Experimental Verification of the Finite Element Analysis of a Dynamically Loaded Semi-Trailer

T/M. D. Tewelde

Thesis presented in partial fulfilment of the requirements for the degree
Master of Science in Engineering Science at the University of Stellenbosch

Thesis Supervisor: Dr E. Terblanche
April 2004

DEPARTMENT OF MECHANICAL ENGINEERING
UNIVERSITY OF STELLENBOSCH

DECLARATION

I, the undersigned, hereby declare that the work contained in this thesis is my own original work and that I have not previously in its entirety or in part submitted it at any university for a degree.

Signature:

Date: 15 Maart 2004

ABSTRACT

The aim of the thesis is to compare results obtained from a finite element analysis method (FEM) to experimental results of a 12.2m long semi-trailer driven off-road. Semi-trailers are of great importance in the transport industry. Furthermore, the need to obtain optimum and reliable semi-trailers in this crucial stream of industry is indispensable. The work focuses on comparing the two results so that the finite element method may be used as design analysis and redesigning tool as a substitute to testing.

The semi-trailer was driven on a relatively rough off-road at different speeds, at 70km/h, 50km/h and 40km/h loaded with about 12 tonnes of brick pallets. The forces at the suspension of the semi-trailer and strains at different parts were measured with the help of strain gauges and other data acquisition equipment.

A finite element model of the semi-trailer was modelled in Nastran for Windows. The trailer parameters in the finite element were tuned to curve fit the test results. A comparison of the two results was made based on the average of absolute values and standard deviation, to verify the validity of the finite element model.

OPSOMMING

Die doel van die tesis is om die resultate wat verkry is deur eindige element metodes (EEM) met eksperimentele resultate van 'n 12.2 m lang leunwa wat bestuur is op 'n grondpad te vergelyk. Leunwaens is baie belangrik vir die vervoer industrie. Verder is die behoefte om optimum en betroubare leunwaens in die industrie te vervaardig baie nodig. Die werk fokus daarop om die 2 resultate te vergelyk sodat die EEM gebruik kan word as ontwerp analiese en herontwerp gereedskapstuk en as 'n vervanging vir toetsing.

Die leunwa was op 'n redelike rowwe pad teen verskillende snelhede nl. 70km/h, 50km/h en 40km/h met 'n 12 ton baksteen vrag gery. Die kragte by die suspensie van die leunwa en die vervorming by verskillende onderdele is gemeet met behulp van rekstrokies en ander data versamelings toerusting

'n Eindige element model van die leunwa is gemodelleer in "Nastran for Windows" . Die sleepwa parameters in die eindige element model is verstel d.m.v krommepassing van die toets resultate. 'n Vergelyking van die 2 resultate is gebasseer op die gemiddelde van die absolute waardes en standaard afwykings, om die geldigheid van die eindige element model te kontroleer.

TABLE OF CONTENTS

LIST OF FIGURES

LIST OF TABLES

LIST OF SYMBOLS

σ	normal stress	MPa
τ	shear stress	MPa
Δ	difference	
F	force	N
A	area	m^2
X	generalized coordinate axis	
0	origin of coordinate axis	
∂	partial differential operator	
d	ordinary differential operator	
x,y,z	cartesian coordinate axes	
F	force per unit volume	Nm^{-3}
x', y', z'	transformed cartesian coordinate axes	
θ,β,α,ϕ	angle degree, ratio	
u	displacement along x-axis	m
v	displacement along y-axis	m
ε	normal strain	$m\ m^{-1}$
γ	shear strain	$m\ n^{-1}$
E	modulus of elasticity	$N\ m^{-2}$
G	shear modulus	$N\ m^{-2}$
υ	Poisson's ratio	ν
U	energy	W
k	stiffness constant	$N\ m^{-1}$
c	damping constant	$m\ s^{-1}$
m	unit mass	kg
ω	angular frequency	$r\ s^{-1}$
ζ	damping ratio	
f	unit force amplitude	
A	displacement amplitude	
H	transfer function	
S	Power Spectral Density	
Σ	summation	

M	mass matrix	
C	damping matrix	
K	stiffness matrix	
Π	Potential energy	W
r	frequency ratio	
$\boldsymbol{l}$	structural length	m
$\boldsymbol{a}$	structural cross sectional area	m^{-2}
$\boldsymbol{q}$	distributed load	N
$\boldsymbol{L}$	element length	m
$\boldsymbol{\{d\}}$	elemental nodal degree of freedom vector	
$\boldsymbol{\{D\}}$	structural nodal degree of freedom vector	
$\lfloor N \rfloor$	shape function	
$\lfloor B \rfloor$	strain displacement matrix	

Chapter 1 INTRODUCTION AND LITERATURE REVIEW

1.1 Document Layout

The work of this document is all focused on comparison of experimentally tested results of strain and stress of a 12.2m long interlink semi-trailer driven off-road with results of its finite element model. To give a brief backup of the formulas and expressions used in the process, the author preferred to outline a short summary of the theoretical base of the whole work in the first part of the document.

A very brief note on the theory of elasticity of materials is given in the first part of chapter 2. The basic expressions of strain and stress and their relation are summarised in this part. In the second part, concepts of mechanical vibration which mainly concentrate on a single degree of freedom is given. A short summary of formulating expressions of multi-degree of freedom is also discussed briefly here. The last part of the chapter contains the fundamental theory behind the concept of finite elements. A summary of the mathematical concept of finite element theory and its basic principles are outlined. Detailing a bit in the formulation of the element characteristic matrix and finding an approximating function, shape function, by interpolating from element nodal values, the chapter concludes with briefing of the finite element package used.

Chapter 3 is mainly devoted to the instruments used and their setting during the test. The first part lists all the equipment used. It also briefs the main characteristics of each piece of equipment. The last part of chapter 3 explains the setting up of the complete test.

Testing and data acquisition are explained in chapter 4. Calibration of each instrument used in getting the required data is discussed in the first part of the chapter. The second part, which itself is divided into two, contains the explanation of the testing methods and samples of measured data. The samples are reported by separating them as input and response samples.

In chapter 5 the finite element analysis technique (FEM) of the semi-trailer is discussed. The finite element modelling of the semi-trailer which includes the elements used, the constraint points and application of loads is explained in the first part. The second part, starting with the briefing on how the finite element method used approximates the second order differential equation of motion,

discusses the trial-curve-fitting method followed to curve fit the two results. The chapter concludes with sample data from the finite element analysis technique.

Chapter 6 discusses the comparison of the results form the two analysis methods, test and finite element. The first part outlines the comparison of the results part by part. The chapter concludes with a static finite element analysis of the semi-trailer for the extreme recorded value.

The report concludes with a summary of conclusion and author's comments.

1.2 Literature Review

In spite of the precautions taken and efforts made in designing and building machines or equipment, it is not uncommon to see structural or design defects in the final product. Sometimes the defect is so serious that it even causes failure of equipment or parts prior to their expected life span and prescribed manufacturer's limits. There are circumstances where the cost of damage is so high that manufacturers are forced to revise their work at high cost. In assessing the cause of the unexpected failure, companies or related organisations prefer to perform practical tests on the failed equipment. J.M. Henshaw, V. Wood and A.C. Hall [19] reported the failure of a particular brand of automobile seat belts with a potential total cost of US$10^9 affecting about 8.8 x 10^6 vehicles in the USA. After completing a detailed test on the seat belt mechanism and manufacturing content, they concluded the failure was due to environmental polymer degradation. They commented in their report that replacement of the seat belt receptacle with more environmentally resistant polymers would have saved the companies billions of dollars.

M.V. Figueiredo, F.M.F. Oliveira, J. P. M. Gonçalves, P. M. S. T. de Castro and A. A. Fernandes [21] made assessments on a failure consisting of fracture of two forks of a fork lift truck with maximum capacity of 25 tonnes at the distance d=1200 mm that was moving a transformer of 22.6 t acting at the distance d=1700 mm. They reported the consequential loss due to damage to the transformer to be of the order of US$35 000, and the cost of replacement of the broken forks was US$70 000. The cost excludes the delay in the supply of the transformer and the cost of the unavailability of the truck during repair. They made mechanical tests for characterization of the material, including tensile and Charpy tests; tests on weld defects and fatigue crack detections; detailed metalographical analysis; stress analysis using the finite element method; and fracture mechanics and plastic collapse analyses. They concluded the failure was due to previous welding defects on one of the forks of the lift truck and recommended an appropriate solution for the repair should consist of using a weld metal similar to the parent metal, provided a suitable weld procedure was specified and treatment is done.

F.S. Silva [23] analysed laboratory tests on two damaged crankshafts of diesel engine vans that were expected to have a life of about 300 000 km each. To fix the damage to some journals, the crankshafts were grinded and re-installed into the van. The investigation was made after the crankshafts lasted 1 000 km each, and the journals were damaged again. Based on his laboratory

results Silva concluded that the cause of the failure was a wrong grinding process that caused small thermal fatigue cracks at the centre of the journals on both crankshafts. These almost invisible cracks, with sharp edges, acted as knives causing a very quick damaging of the journal bearings, and as a consequence damaged the journals themselves.

V.M.J. Sharma, G. Venkatanarayana, V. Diwakar, S. Arumugham and T. S. Lakshmanan [17] conducted an experimental investigation after the chamber used in the upper stage of a satellite launch vehicle had a failure in the welded portion at an internal pressure of 110 bar against a design proof pressure of 165 bar during routine proof pressure testing as a functional qualification testing program before final clearance for use during the flight. Their investigation revealed welding defects as the origin of failure. The welding defect had grown into a semi-elliptical surface crack during the manufacturing process of the pressure chamber, resulting not only in a localized reduction of the wall thickness of the chamber, but also acting as a stress raiser, due to which the chamber had failed at a pressure much below its design level.

Practical testing of products or structures involves knowledge of the nature of a structure. In essence, it is the best means in terms of understanding the actual characteristics of the problem. In spite of its drawbacks of being expensive most of the time and that it can be done only on a sample, manufacturers prefer to perform practical tests not only to investigate failure or malfunction, but also to get a better understanding of and actual performance from their final product.

J.A. Tamboli and S.G. Joshi [18] conducted a field experiment to predict the Mean Square Acceleration Response (MSAR) of vehicles subjected to random excitation due to road unevenness and variable velocity. They calculated the RMSAR of a vehicle for actual field excitation using the Fast Fourier Transformation (FFT) technique to obtain the power spectral density (PSD), by recording observations at the rear wheel. They found the PSD of road excitation to follow an approximately exponentially decreasing curve, contrary to most previous study assumptions of the PSD of road excitation as white noise. By studying the effects of the time lag of the wheelbase and vehicle velocity on the RMSAR also, they recommended new design variables for the front and rear suspension by minimizing the RMSAR from a ride comfort view.

Hideaki Ishii, Yukinori Oishi, Hiroaki Hoshino and Junzo Tamari [15] conducted experimental stress analyses to determine the characteristics of stress distribution of a fuel tank hanger. They

concluded that the experimental analysis results helped them to ignore the non-linearity effect of the non-linear element of the strap for fixing the fuel tank which makes dynamic stress analysis caused by excitation of road inputs and engine vibration of a truck in operation and fuel movement in the tank difficult. The results helped them also to develop a new method of dynamic stress distribution analysis of the hanger to study the effect of a hanger overhang.

The force transmission from road surface to a rolling tyre has been successfully measured by force measurements on suspension parts and correction for inertia forces of suspension parts by Masaaki Minakawa, Jun Nakahara, Jiro Ninomiya and Yukihiro Orimoto [20]. From their analysis based on their measured data, they concluded the force from road to tyre has a sharp directivity, which is inclined rearward in side view, within the frequency range between 5 and 15 Hz. Reporting their finding on the inclination angle of the direction of action to be dependent on the vehicle velocity, they recommended the optimum locus inclination angle which is desirable for reducing harshness to be approximately 6 degrees, in light of considerations such as the fact that harshness tends to become problematic at relatively low vehicle speeds.

W.J. Stevenson [6] conducted static structural load tests on 'de havilland vampire wings' as part of his M. Eng. thesis, and reported that the simple beam model theory is not quite applicable to the complex structural members of the jet wing. Practical testing is the alternative in understanding the design parameters for such complex structures.

H. J. Beerman [10] also recommends strongly in favour of practical testing. "It is of paramount importance that experimental verification be provided for any mathematical structural analysis, this is especially true when new methods are being developed."

The subject matter of this report is to examine how close a finite element analysis method can approximate practical testing so that it can be used as an alternative tool in design and analysis. The forces at the axle suspensions and strains at different parts of a 12.2 metre long interlink semi-trailer driven off-road are measured experimentally. The results are compared to results obtained from a finite element analysis model. There is not much literature, at least to the author's knowledge, on subject matter exactly the same as that of this report. The above-mentioned research work all stress on practical testing for investigating design limits and manufacturing defects. Du Toit [22], on the other hand, used a merely finite element analysis technique, as part of his M. Eng. thesis, in

predicting the need for redesigning a refrigerated semi-trailer and concluded there was some possibility of design modification that could result in weight reduction of the semi-trailer. He also recommended additional reinforcements on the chassis neck of the trailer.

To investigate on how close the numerical technique approximates the practical testing, this report is focused on comparison of practical test with numerical analysis technique results so that the latter can be used as a substitute option.

Chapter 2 BASIC THEORETICAL CONCEPTS

2.1 Elastic Properties of Materials

The test piece of the experiment reported on in this thesis is a steel-made, 12.2m long interlink semi-trailer. In outlining the elastic property of steel and its mechanical strength governing equations, steel is taken as a linearly elastic, isotropic and homogeneous material. Although steel is far beyond satisfying all the above properties in its molecular form, it almost does on a macro-level [2]. Some of the elementary equations of elasticity, governing the stress and strain expressions in a linearly elastic, homogeneous and isotropic material, are given here as introduction to the theoretical part of the paper on strength of materials.

2.1.1 Stress in Materials

For any material under the influence of some forces or moments the stress tensor is defined as the limiting case of force to area ratio.

$$\sigma = \lim_{\Delta A \to 0} \frac{\Delta F}{\Delta A} \quad \text{... 2-1}$$

Where

σ	Stress in the material
ΔF	limiting force
ΔA	limiting area

As a second order tensor quantity, the surface on which it acts is equally important to define the stress at a given point uniquely, in addition to its magnitude and direction. Taking a cubic material, the stress components on each surface, in a three-dimensional space is given in Fig. 2.1, where the direction of the material is taken parallel to the coordinate system.

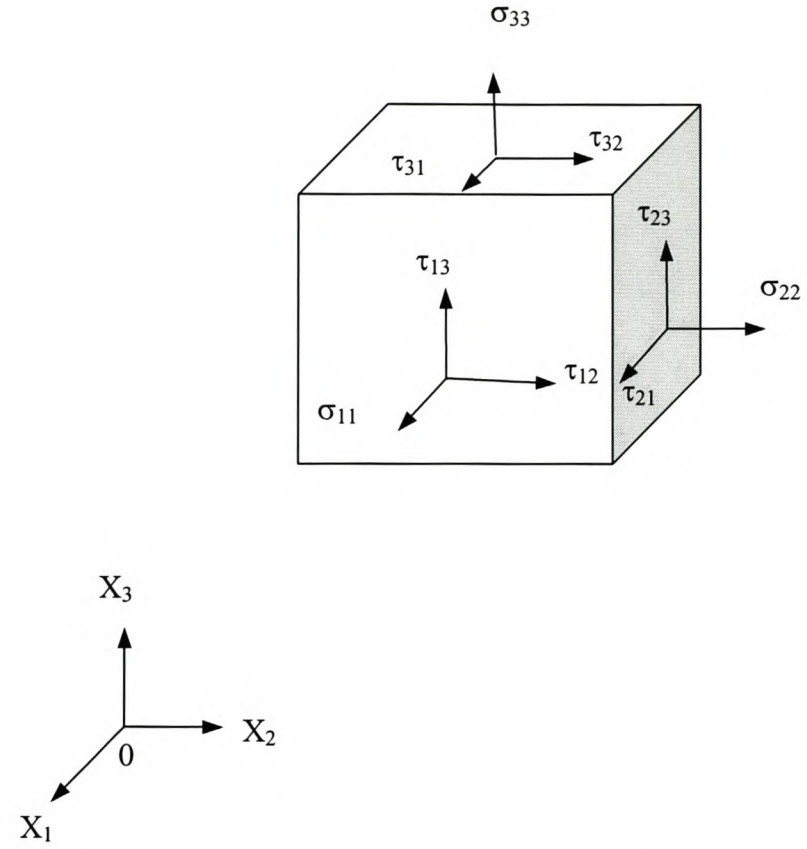

Fig. 2.1 Stress components in a three-dimensional material

The σ component, in the above figure, is the stress perpendicular to a given surface, which is known as normal stress, and the τ component is the stress parallel to the surface, the shear stress. The first subscript on the stress component represents the surface on which the stress acts and the second its direction.

2.1.1.1 Stress Equilibrium Equations

For a non-uniformly stressed body the stress components along its volume can be calculated from the principle of equilibrium of forces. Considering a cubic object in three-dimensional Cartesian coordinate system, the differential stress equilibrium equations are given by:

$$\frac{\partial \sigma_{xx}}{\partial x}+\frac{\partial \tau_{xy}}{\partial y}+\frac{\partial \tau_{xz}}{\partial z}+F_x=0$$
$$\frac{\partial \sigma_{yy}}{\partial y}+\frac{\partial \tau_{xy}}{\partial x}+\frac{\partial \tau_{yz}}{\partial z}+F_y=0 \quad \text{... 2-2}$$
$$\frac{\partial \sigma_{zz}}{\partial z}+\frac{\partial \tau_{xz}}{\partial x}+\frac{\partial \tau_{yz}}{\partial y}+F_z=0$$

Where ***F*** is force per unit volume along the indexed direction.

Materials having their third geometric dimension relatively smaller than the remaining two sides, have less influential stress components along their shorter dimension in comparison to the rest. In dealing with the elastic property of these materials, ignoring the quantities along the shorter dimension does not make significant change on the overall solution of their problems of elasticity [2]. Due to this reason, materials having their third geometrical dimension relatively shorter in comparison to the other two are treated as two-dimensional objects. Generally the elastic property of such materials can be given in two-dimensional form.

Equation 2.2 for two-dimensional material is:

$$\frac{\partial \sigma_x}{\partial x}+\frac{\partial \tau_{xy}}{\partial y}+F_x=0$$
$$\frac{\partial \sigma_y}{\partial y}+\frac{\partial \tau_{xy}}{\partial x}+F_y=0 \quad \text{... 2-3}$$

All components of the test piece in this experiment have one dimension relatively smaller than the other two, which enables us to treat each part of the structure as two-dimensional problem. In relevance to the assumption of a two-dimensional object of the test piece, all the ongoing equations of elastic property of materials in this report are for two-dimensional problems only.

2.1.1.2 Stress at a Point

Taking a point in a stressed body the stress components of all surfaces passing through that point are not the same. That is, for two different surfaces passing through the same point the stress components for each surface are different at the point, provided that the body is not uniformly

stressed. If the stress components at a point are known (in this case a plane stress) on a surface, the stress on any surface inclined at an angle θ to the specified surface is:

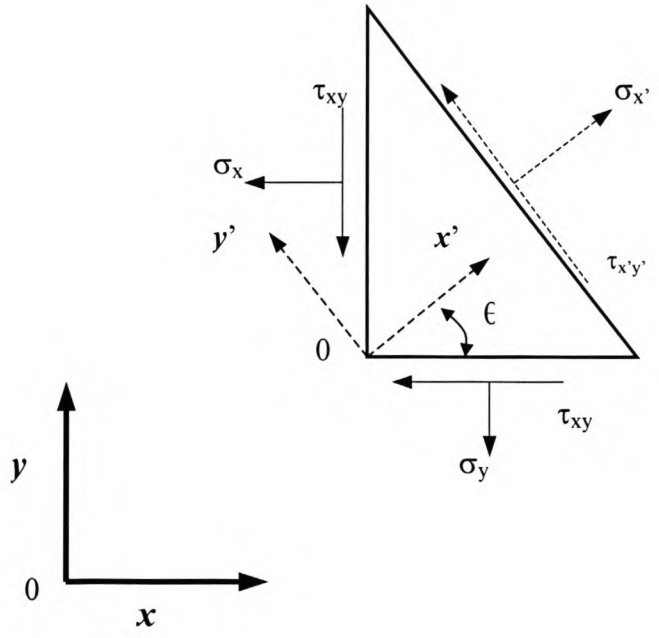

Fig. 2-2 Stress components of a surface inclined at angle θ to the material direction

$$\sigma_{x'} = \tfrac{1}{2}(\sigma_x + \sigma_y) + \tfrac{1}{2}(\sigma_x - \sigma_y)\cos 2\theta + \tau_{xy}\sin 2\theta$$
$$\sigma_{y'} = \tfrac{1}{2}(\sigma_x + \sigma_y) - \tfrac{1}{2}(\sigma_x - \sigma_y)\cos 2\theta - \tau_{xy}\sin 2\theta \quad \textbf{... 2-4}$$
$$\tau_{x'y'} = -\tfrac{1}{2}(\sigma_x - \sigma_y)\sin 2\theta + \tau_{xy}\cos 2\theta$$

2.1.1.3 Principal Stresses

The angle at which the stress at a point is maximum or minimum is the principal angle. Differentiating the first equation of equation (2.4) with respect to θ the expression of the principal angle can be shown to be:

$$\tan 2\theta_p = \frac{2\tau_{xy}}{\sigma_x - \sigma_y} \quad \textbf{... 2-5}$$

Equation (2.5) is satisfied by two mutually perpendicular directions, at which the normal stress is either maximum or minimum. Comparing the equilibrium point of the first derivative of the normal stress expression with respect to θ and the expression of the shearing stress in equation (2.4), the

shearing stress at the principal plane is zero, the plane formed by the direction of the principal stresses. Substituting the value of the principal direction on the first part of equation (2.4), the principal normal stresses are calculated to be

$$\sigma_{1,2} = \frac{\sigma_x + \sigma_y}{2} \pm \sqrt{\left(\frac{\sigma_x - \sigma_y}{2}\right)^2 + \tau_{xy}^2} \quad \text{... 2-6}$$

2.1.2 Material Deformation

Deformation is the relative change of position of points in a body [4]. If a body under the influence of some force is sufficiently constrained there is always some sort of deformation in the body.

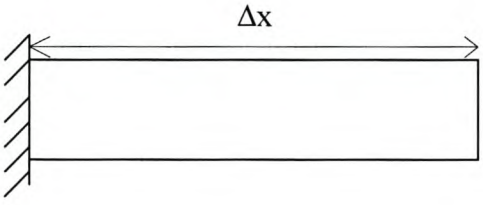

a. Before deformation

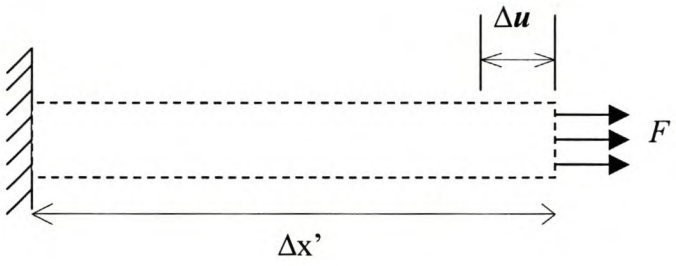

b. After deformation

Fig. 2-3 Normal deformation of a material of length Δx

Fig. 2.3 shows the axial deformation of a bar of original length **Δx** fixed at one end to a length **Δx'** after force ***F*** is applied.

The limiting ratio of the change of length to the original length is defined as normal strain.

$$\varepsilon_x = \lim_{\Delta x \to 0} \frac{\Delta u}{\Delta x} \quad \text{... 2-7}$$

Straining can be either change in length and/or orientation of a stressed body. The strain caused by change of angular orientation is called shear strain and is donated by γ most of the time. For a rectangular surface, the deformation equation for the two straining phenomena can be calculated from geometrical consideration only. Treating the two deformations separately the expressions for strain components can be calculated as below.

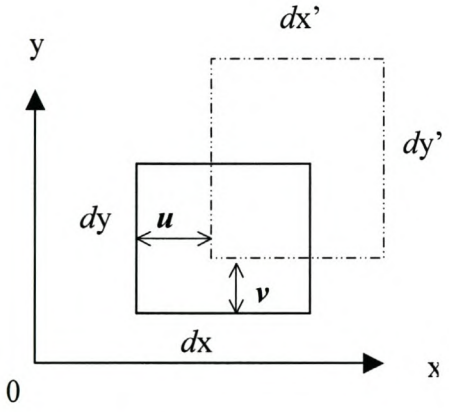

a. Normal deformation

$$dx' = dx + \frac{\partial u}{\partial x} dx \quad \text{.... a}$$

$$dy' = dy + \frac{\partial v}{\partial y} dy \quad \text{... b}$$

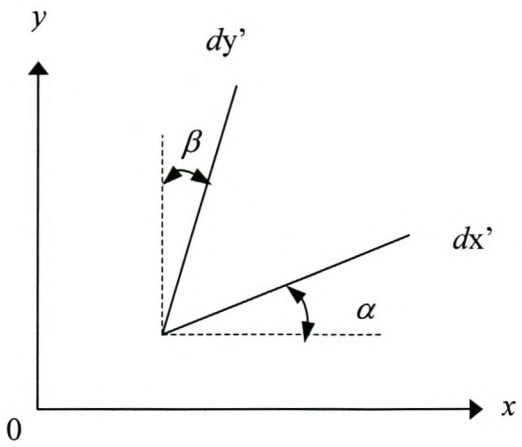

b. Shear deformation

Fig. 2-4 Two-dimensional material deformation

For small deformations, tan α and tan β can be approximated by α and β respectively. Similarly ***dx'*** and ***dy'*** are approximated as ***dx*** and ***dy***. Applying these approximations to the angular deformation of the rectangular surface:

$$\alpha = \frac{\partial v}{\partial x}$$
$$\beta = -\frac{\partial u}{\partial y} \quad \text{... c}$$

... 2-8

From the definitions of normal and shear strains mentioned above, the strain equations can be expressed as functions of displacements, and the expressions for two-dimensional materials are:

$$\varepsilon_x = \frac{\partial u}{\partial x}$$
$$\varepsilon_y = \frac{\partial v}{\partial y} \qquad \text{... 2-9}$$
$$\gamma_{xy} = \frac{\partial u}{\partial y} + \frac{\partial v}{\partial x}$$

Where ε represents the normal strain, related to change of length, and γ is the shearing strain, strain is due to change of angle.

2.1.3 Compatibility Equations

The above strain-displacement equations are merely driven from a geometrical point of view. Since three strain variables are given as a function of only two displacement variables, it is not possible to get a unique displacement function for given strain values. That is, although it is possible to get a unique strain function for a given deformation, the reverse is not true [1]. The strain-displacement equation must satisfy the following compatibility equation in order to avoid any discontinuity or a multi-solution nature of a given deformation problem.

$$\frac{\partial^2 \varepsilon_x}{\partial y^2} + \frac{\partial^2 \varepsilon_y}{\partial x^2} = \frac{\partial^2 \gamma_{xy}}{\partial x \partial y} \quad \textbf{... 2-10}$$

2.1.4 Stress-Strain Relations

From Hooke's Law, for small deformation of uni-axial elastic materials, the stress of an object is linearly related to its strain with a constant of proportionality known as modulus of elasticity.

$$\sigma = E\varepsilon \quad \textbf{... 2-11}$$

Where σ Is the normal stress

ε Normal strain

E Modulus of elasticity

In multi-dimensional objects, the change of length in one direction causes an opposite influence on other directions due to Poisson's influence. For an arbitrarily deformed two-dimensional object, the stress-strain relation is:

$$\varepsilon_x = \frac{1}{E}(\sigma_x - \upsilon\sigma_y)$$

$$\varepsilon_y = \frac{1}{E}(\sigma_y - \upsilon\sigma_x) \quad \text{... a}$$

$$\gamma_{xy} = \frac{\tau_{xy}}{G}$$

Where, $G = \dfrac{E}{2(1+\upsilon)}$, is the shear modulus.

Or

$$\sigma_x = \frac{E}{1-\upsilon^2}(\varepsilon_x + \upsilon\varepsilon_y)$$

$$\sigma_y = \frac{E}{1-\upsilon^2}(\varepsilon_y + \upsilon\varepsilon_x) \quad \ldots \text{b}$$

$$\tau_{xy} = G\gamma_{xy}$$

... 2-12

2.1.5 Yielding Theories of Failure

As the tensile stress increases, all ductile materials reach a point where the stress-strain relation is no more linear. The point at which the material loses its linear elastic property is known as the proportional limit. If the stress is increased further, the material reaches a point known as yield point at which the material deforms significantly without any noticeable increase in stress. The material starts to fail after passing a maximum point in the stress-strain curve, the ultimate stress. The point at which the material fails is called the rupture point.

There are different failure theories predicting the failure of a structure. Each theory has its own advantage and disadvantage. In this report only one theory, the maximum distortion energy theory, the theory thought most appropriate for predicting failure in two-dimensional structures and isotropic materials, is given.

The maximum distortion energy theory, proposed by M.T. Huber [4] and today commonly known as Von Mises criteria, states failure by yielding occurs when at any point in the body the distortion energy per unit volume in a state of combined stress becomes equal to that associated with yielding in a simple tension test.

The distortion energy per unit volume for two-dimensional object is:

$$U_{od} = \frac{1}{12G}[(\sigma_x - \sigma_y)^2 + \sigma_y^2 + \sigma_x^2 + 6\tau_{xy}^2] \quad \ldots \text{a}$$

Or

$$\sigma_1^2 - \sigma_1\sigma_2 + \sigma_2 = \sigma_{yp}^2 \quad \ldots \text{b}$$

... 2-13

And the maximum energy of distortion in a simple test:

$$U_{od} = \frac{1+\upsilon}{3E}\sigma_{yp}^2 \quad \textbf{... 2-14}$$

Equating the two equations for the principal stresses, we get

$$\left(\frac{\sigma_1}{\sigma_{yp}}\right)^2 - \left(\frac{\sigma_1}{\sigma_{YP}}\right)\left(\frac{\sigma_2}{\sigma_{YP}}\right) + \left(\frac{\sigma_2}{\sigma_{YP}}\right)^2 = 1 \quad \textbf{... 2-15}$$

as failure theory for maximum energy of distortion, where σ_1 and σ_2 are the principal stresses in a two-dimensional problem and σ_{yp} is the stress at yield point.

2.1.6 Conclusion

The above summary is a very brief concept of the elastic behaviour of materials irrespective of the external influences that cause them. The response of structures to external influence depends both on their elastic nature, and the magnitude and rate of external or internal influences acting upon them [4]. To complement the above theory of elasticity on the factors causing material stress and deformation, a brief description of the response of materials to external influences will be given in the next section. Some basic vibratory responses of materials to sinusoidal forcing functions, as well as to arbitrary or random forcing functions are outlined.

2.2 Concepts of Vibration

Vibration is a repetitive motion of objects [14]. Since structural vibration problems present a major hazard and design limitation for a wide range of engineering products [7], it is worth outlining some of its basic theoretical concepts as a backup to the experimental analysis of the response of the semi-trailer to forces caused by road profile and trailer speed.

This report is mainly devoted to the nature of response of a truck trailer driven on a rough road. The forcing function is typically of random nature. To help visualising the response to random forces, the theoretical concepts of response to definitive force is given first. Starting with the response of a single degree of freedom of a spring mass system, the concept of response to a random forcing function is discussed. In the second part, a short note on multi-degree of freedom equations of vibration is given.

2.2.1 Single Degree of Freedom

2.2.1.1 Sinusoidal Input

The equation of motion of a sinusoidally driven object of mass ***m*** connected to a spring end of spring constant ***k***, with the second end fixed, and viscous damping ***c*** is:

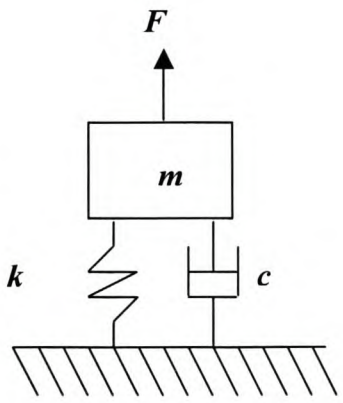

Fig. 2-5 Spring-model of a vibrating point mass

$$m\ddot{x} + c\dot{x} + kx = F_o \cos \omega_{dr} t \quad \ldots \text{a}$$

Or

$$\ddot{x} + 2\zeta\omega\dot{x} + \omega^2 x = f_o \cos \omega_{dr} t \quad \ldots \text{b}$$

... 2-16

Where

$$\omega = \sqrt{\frac{k}{m}} \quad \ldots \text{a}$$

is the system's natural frequency

$$c_{cr} = 2m\omega \quad \ldots \text{b}$$

critical damping coefficient

$$\zeta = \frac{c}{c_{cr}} \quad \ldots \text{c}$$

the damping ratio

$$f_o = \frac{F_o}{m} \quad \ldots \text{d}$$

unit amplitude of forcing function

... 2-17

ω_{dr} - frequency of forcing function

As a second order non-homogeneous differential equation, equation (2.16) has different solutions depending on the value of damping ratio, ζ. For the option of the solutions of a vibratory nature, the solution of equation (2.16) is given by

$$x(t) = Ae^{-\zeta\omega t} \sin(\omega_d t + \theta) + A_o \cos(\omega_{dr} t - \phi) \quad \ldots \text{a}$$

Where

$$A_o = \frac{f_o}{\sqrt{\left(\omega^2 - \omega_{dr}^2\right)^2 + \left(2\zeta\omega\omega_{dr}\right)^2}} \quad \ldots \text{b}$$

amplitude of the steady part of the solution,

$$\phi = \tan^{-1}\left(\frac{2\zeta\omega\omega_{dr}}{\omega^2 - \omega_{dr}^2}\right) \quad \ldots \text{c}$$

the phase shift, and

$$\omega_d = \omega\sqrt{1-\zeta^2} \quad \ldots \text{d}$$

the damped frequency.

... 2-18

The values of A and θ depends on the initial conditions of the system.

The first part of equation (2.18a) is the homogeneous solution of the problem and it decays exponentially any time. More emphasis is put on the steady state solution of the expression, the second part of equation (2.18a), although care must be taken in discarding the transient solution always [14]. Having a close look at equation (2.18b) important characteristic curves can be drawn by taking the ratio of the amplitudes of the steady state response and the forcing function as a function of the frequency ratio defined by

$$r = \frac{\omega_{rd}}{\omega} \quad \ldots \text{a}$$

$$\frac{A_o k}{F_o} = \frac{A_o \omega^2}{f_o} = \frac{1}{\sqrt{\left(1-r^2\right)^2 + \left(2\zeta r\right)^2}} \quad \ldots \text{b}$$

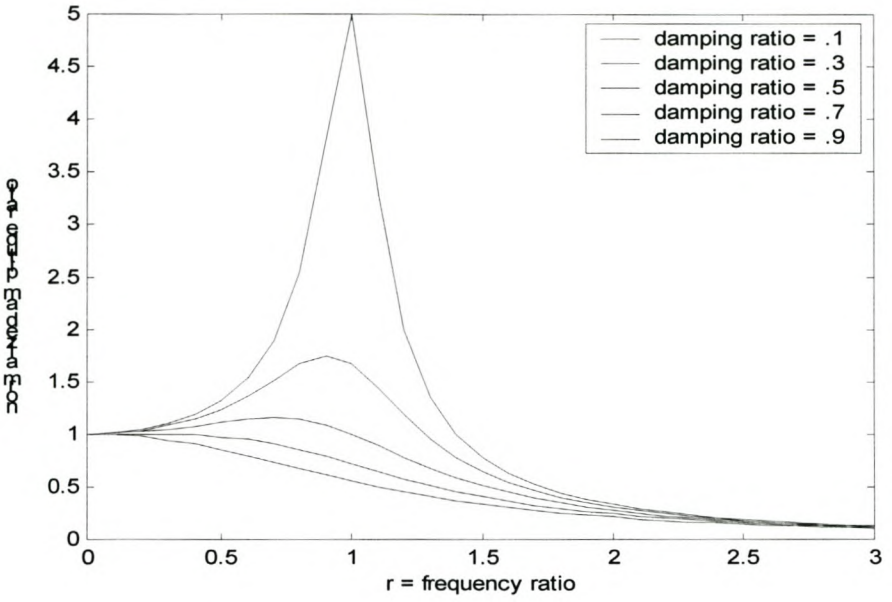

Fig. 2-6 Plot of response to forcing amplitudes as a function of frequency ratio

$$\phi = \tan^{-1}\left(\frac{2r\zeta}{1-r^2}\right) \quad \ldots \text{ c}$$

... 2-19

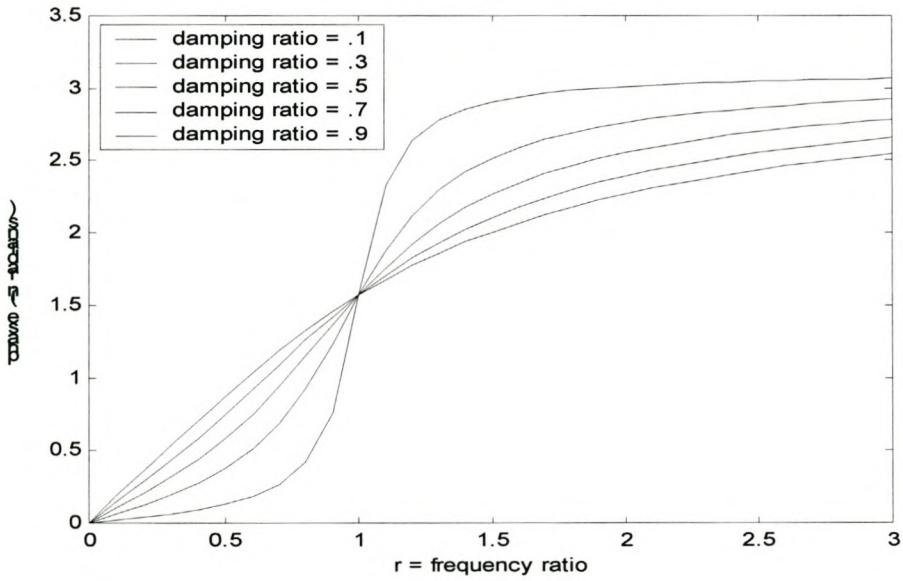

Fig. 2-7 Plot of phase shift as a function of frequency ratio

Figures 2.6 and 2.7 show important characteristics curves of the amplitude ratio and phase shift of the problem as the driving frequency closes the undamped natural frequency of the system. This

characteristic is very helpful in identifying the natural frequency of the system for known forcing frequencies or vice versa.

An alternative method of solving the particular solution of equation (2.16) is by Laplace transform. Referring to equation (B-3) in Appendix B, the Laplace transform of both sides of equation (2.16), assuming the initial conditions to be zero, is

$$(ms^2 + cs + k)X(s) = F(s) \quad \textbf{... 2-20}$$

Where F(s) and X(s) are the Laplace transform of the forcing function and response function respectively and s is a complex transform variable.

The ratio of the Laplace transform of the response function to the Laplace transform of the forcing function is called the transfer function of the system.

$$\frac{X(s)}{F(s)} = \frac{1}{ms^2 + cs + k} = H(s) \quad \textbf{... 2-21}$$

Equation (2.21) is an important expression in vibration, which relates the Laplace transform of the system to the dynamic parameters of the system only.

It is convenient to express equation (2.21) as a function of frequency since most engineering problems are expressed similarly. The frequency transform form of equation (2.21) can be found by substituting s by $j\omega_{dr}$ or from equation (B-8) in Appendix – B,

$$H(j\omega_{dr}) = \frac{1}{k - m\omega_{dr}^2 + jc\omega_{dr}} \quad \textbf{... 2-22}$$

Equation (2.22) is a key expression in predicting the dynamic parameters of a vibrating single degree of freedom system as plotted in figure 2.8.

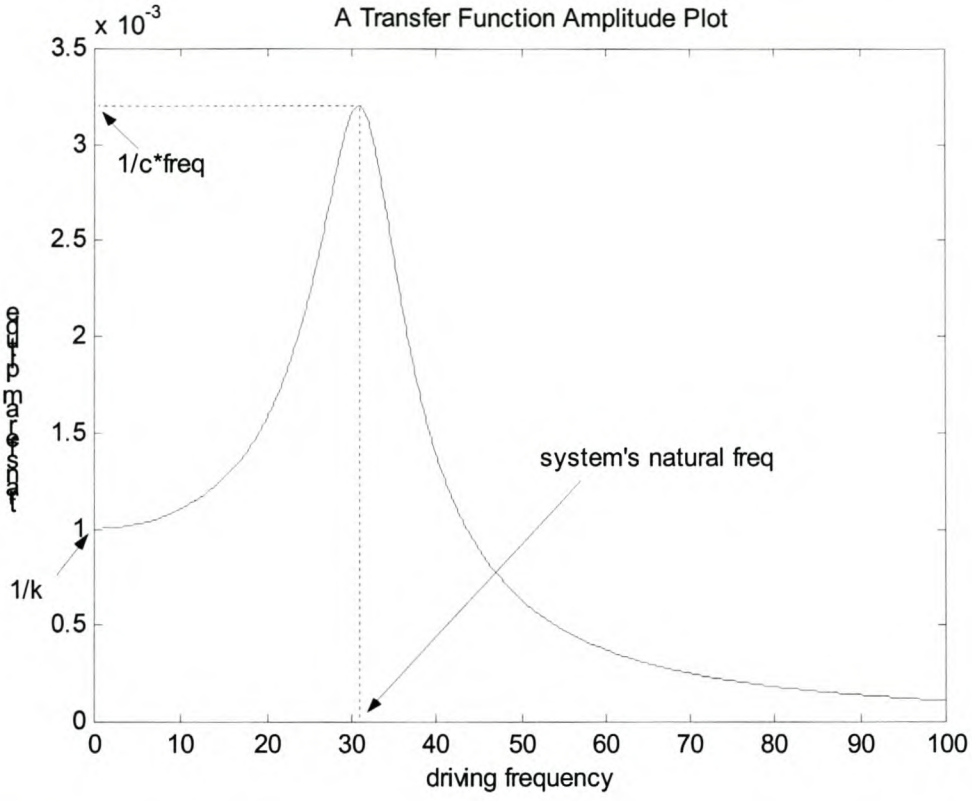

Fig. 2-8 Amplitude of transfer function vs. frequency

The curve is dominated by the region where the driving frequency is close to the natural frequency of the system. The maximum of the curve is at the point where the two values coincide. Equating the natural frequency of the system to the driving frequency at the point where the amplitude of the transfer function is maximum, the damping is calculated as the inverse of the transfer function amplitude and the driving frequency. The stiffness constant can be extracted also from the point where the curve crosses the amplitude axis. All the parameters are labelled in figure 2.8.

2.2.1.2 Random Forcing Functions

Unlike deterministic forcing functions which can be treated as the sum of impulse, or sinusoidal forcing functions using Fourier transforms, response to random forcing functions are treated from a statistical point of view. For an arbitrary forcing function F(t), the response function can be calculated as a sum of the products of the amplitudes of the forcing function and the response to a unit impulse force. Taking the limiting sum, the expression for the problem is given below, from [14]

$$x(t) = \int_0^t F(p)h(t-p)dp \quad \text{... 2-23}$$

Where

$$h(t-p) = \frac{1}{m\omega_d} e^{-\zeta\omega(t-p)} \sin\omega_d(t-p), \; t > p \quad \text{... 2-24}$$

is the response to a unit impulse forcing function. And zero for the interval $0 < t < p$.

Considering the value of h(t - p) for $t < p$ and changing the dummy variable to **q**, equation (2.24) can be written as

$$x(t) = \int_{-\infty}^{\infty} F(t-q)h(q)dq \quad \text{... 2-25}$$

Referring to equation (C-19), in Appendix C, the power spectral density, PSD, of a response function x(t) is given by

$$S_{xx}(\omega) = \frac{1}{2\pi} \int_{-\infty}^{\infty} \left[\lim_{T\to\infty} \frac{1}{T} \int_0^T x(z)x(z+p)dz \right] e^{-j\omega p} dp \quad \text{... 2-26}$$

Substituting the value x(z) from equation (2.25) in equation (2.26) and a small manipulation, the power spectral density, PSD, of the response displacement function is given as a function of the PSD of the forcing function,

$$S_{xx} = |H(\omega)|^2 S_{ff}(\omega) \quad \text{... 2-27}$$

If there are ***n*** number of forcing functions, the PSD of the response is, from [3].

$$S_{xx}(\omega) = \sum_{i=1}^{n}\sum_{j=1}^{n} H_i^*(\omega)H_j(\omega)S_{f_i f_j}(\omega) \quad \text{... 2-28}$$

Where H_i^* is the complex conjugate of H_j, the transfer functions due to **ith** input function.

Equation (2.28) is an important expression in analysing random vibration problems using modal analysis. For uncorrelated inputs, equation (2.28) simplifies to

$$S_{xx}(\omega) = \sum_{i=1}^{n} |H_i(\omega)|^2 S_{f_i}(\omega) \quad \textbf{... 2-29}$$

2.2.2 Multi-Degree of Freedom

The single degree of freedom problem formulation is too simple for most physical applications in nature. Many problems of application are relatively more complex to be approximated by a single degree of freedom problem. Since it is easier to handle multi-degree of freedom problems from the basics of a single-degree of freedom, it is reasonable to discuss the single-degree of freedom problem at the first stage.

One example of a multi-degree of freedom is, assuming ***n*** number of masses connected to each other with a set of springs and dampers in series. In solving the displacement function of the whole set of spring-mass system displacing in an axial direction, each mass can be assumed having a single degree of freedom, summing up to ***n*** degrees of freedom for the complete system.

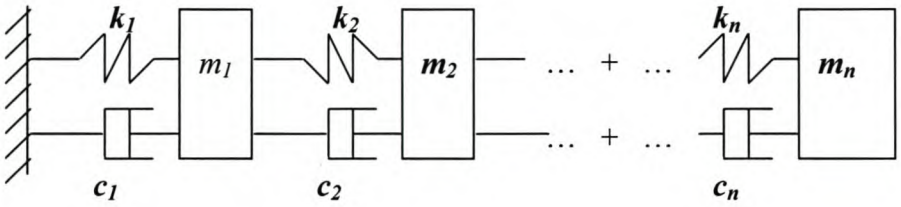

Fig. 2-9 A spring mass model for a system of n degrees of freedom

Writing the equation of motion for each mass results in an array form of a set of equations that can be represented by the following expression.

$$M\ddot{x} + C\dot{x} + Kx = F(t) \quad \textbf{... 2-30}$$

Where

M, ***C*** and ***K*** are $n \times n$ mass, damping and stiffness matrices respectively. And **x** and ***F*** are $n \times 1$ displacement and force vectors.

For a damping coefficient proportional to the sum of the stiffness and mass matrices, say

$$C = aM + bK \quad \textbf{... 2-31}$$

equation (2.30) can be decoupled into **n** number of single-degree-of-freedom problems using modal analysis. And the solution can be found in a closed form. The whole procedure follows the same as the solution formulation of a single-degree-of-freedom-problem to each equation, once the equations are decoupled.

The modal form of equation of motion for the k^{th} term of the ***n*** number of single-degree of freedom equations is

$$\ddot{r}_k(t) + 2\zeta_k \omega_k \dot{r}_k(t) + \omega_k^2 r_k(t) = f_k(t) \quad \textbf{... 2-32}$$

Where

$\zeta_k = \dfrac{a}{2\omega_k} + \dfrac{b\omega_k}{2}$, the k^{th} mass damping ratio

ω_k - the k^{th} mass natural frequency

And its solution is

$$r_k(t) = d_k e^{-\zeta_k \omega_k t} \sin(\omega_{dk} t + \phi_k) + \frac{1}{\omega_{dk}} e^{-\zeta_k \omega_k t} \int_0^t f_k(p) e^{\xi_k \omega_k \tau} \sin(\omega_{dk}(t-p)dp \quad \textbf{... 2-33}$$

In actual problems equation (2.31) is not always true. In addition to the damping coefficient to be non-linear, the nature of the multi-degree problem may be more complex to be approximated by a set of mass-spring systems displacing in a straight line. The effect of moments and other multi-directional forces may result in more complex responses of rotation and translation, which cannot be solved in a closed form. In problems resulting in a more complex form to be solved in a closed form, the solution of the problem is estimated numerically using different computer simulations.

2.2.3 Conclusion

The brief summary in vibration of objects is to give a basic idea of solving some elementary vibratory problems in a closed form or analytically. Most problems in nature are too complicated to be solved in this manner. In addition to the complexities of the nature of the problem, most data acquisition machines are digital, they cannot handle continuous data. Therefore it is compulsory to use some numerical techniques that approximate the nature of the problem to an acceptable degree

of accuracy. Briefing the formulation of finding a closed form solution of some elementary problems of mechanical vibration in this section, the next section will discuss a way of formulating one type of numerical approximation method.

The Finite Element Method is the numerical approximation method used in this report. The following section will briefly outline the basic concepts in formulating the finite element method.

2.3 Finite Element Concepts

The finite element method is a numerical procedure for analysing structures and continua. Although it started as a method of stress analysis in its early phase starting in the middle 1960s, the finite element method gained wide acceptance when it was recognised as a solution of a variational problem by minimisation of a functional (functions whose arguments themselves are functions). Thus the method is used to deal with problems of all fields that can be cast in a variational form [11].

A variational form of a differential equation is the weak (integral) form of the posted problem. To have a clear insight of the finite element method, it is necessary to understand how to formulate the variational form of a differential problem and know to derive an algebraic system of equations related with the variational form [8]. A brief outline of how to formulate a variational form of a given differential equation and some basics of formulating the finite element algebraic equations is given here.

2.3.1 Derivation of the Variational Form of a Differential Equation

To simplify the process of deriving the variational form of a given differential equation the steps are accompanied by an example. Suppose we want to find the variational form to the following differential equation,

$$-\frac{d}{dx}(a\frac{du}{dx}) - f = 0\,,\ 0 < \mathrm{x} < \mathrm{L}. \quad \ldots \mathrm{a}$$

having the following boundary conditions

$$u(0) = 0,\ (a\frac{du}{dx})\Big|_{x=L} = P \quad \ldots \mathrm{b}$$

Where **a** and **f** are both functions of **x** and **P** is a constant.

The first step in finding the variational form is to multiply the differential equation by a test function **v(x)** which is a variation of **u(x)**, and integrate the whole expression over the specified domain. The test function is an arbitrary continuous function in the domain and satisfies the essential boundary conditions.

$$0 = \int_L \left(a\frac{dv}{dx}\frac{du}{dx} - vf \right) dx + \left[v\left(-a\frac{du}{dx} \right) \right]_0^L \quad \text{... 2-35}$$

The second step is to specify the test function by identifying the boundary conditions. From equation (2.35), the coefficient of **u** or its derivative equivalent to the test function, in the integral of boundary conditions, is the natural boundary condition. In this case $-a\frac{du}{dx}$ is a natural or nonessential boundary condition. The values of **u** or its derivative, equivalent to the test function in the same integral are the essential boundary conditions. In this case **u** is the essential boundary condition. The test function is then specified at this point in a way to satisfy the essential boundary condition and is arbitrarily continuous in the domain.

The last step is to simplify the expression and write its functional form.

$$I(u) = \int_0^L \left[\frac{a}{2}\left(\frac{du}{dx} \right)^2 - uf \right] dx - Pu(x_L) \quad \text{... 2-36}$$

The $\frac{1}{2}$ coefficient in equation (2.36) is to help write the functional in a quadratic form. Equation (2.36) can be solved like any quadratic functional using the method of variational calculus.

As can be seen from equation (2.36), compared to differential equation (2.34), the order of differentiation is weakened to one and the natural boundary condition is included in the integral of the functional itself. That is, the differential equation is weakened into an integral form, which is needed to satisfy less constraining values. Although equation (2.36) is not equal to equation (2.34), whenever the solution of the differential equation exists, it coincides with the solution of the variational form [8].

Equation (2.36) is the expression for a total potential energy ($I(u) = \Pi$) of an axially loaded bar, where each part of the expression is the potential due to straining, body force and nodal force respectively.

2.3.2 Finite Element Formulation

The finite element method is a piecewise variational method [11]. In classical variational approximation methods the functional of a given problem is approximated by a sum of some arbitrary functions ($u = c_i\varphi_i$) over the whole domain of the problem. c_i is an arbitrary parameter to be determined so that it satisfies the requirements of the problem at hand. This kind of approximation method gets to be more and more complicated as the geometry gets bigger and irregular; and as the nature of the problem gets more complicated.

The finite element method on the other hand, overcomes the limitation of the classical variational method by first dividing the problem domain into more, simpler geometrical units called *elements*. Then an approximation function is sought by interpolating the values on the edge or boundary points of the element known as *nodes*. What can be observed here, on the advantage of the finite element method over the classical variational method is: The approximating function does not get complicated whatever the geometry of the domain, as far as it is divided into appropriate simpler units. And the approximation is not simply an arbitrary function. It is interpolated from the values of the edge element or nodes based on sound mathematical foundation.

The following are the major steps needed in the formulation of a finite element problem:

- Discretizing the domain into simpler geometrical entities or elements
- Deriving the governing equations for each element
- Assembling an equation of the each element to get the equation of the whole structure
- Applying the prescribed loads and boundary conditions
- Solving the set of simultaneous algebraic equations to get the solution of the assembled structure
- Calculating other post-process quantities required for the structure.

2.3.2.1 Discretization of a Structure

In solving a structural problem using the finite element method, the first step is to divide the structure into simpler units or elements. The type and the number of elements to use, depend on the property of the domain or structure and the nature of the problem to handle.

For a steel bar under the influence of an axial load, for example, line elements are appropriate in handling the problem with the finite element method. Say we have a bar of length ***l*** and a uniform cross sectional area ***a***. The bar is loaded with a uniformly distributed weight ***q*** along its length and a point force ***F*** at its tip. The elongation of the bar at the free end is needed to be solved.

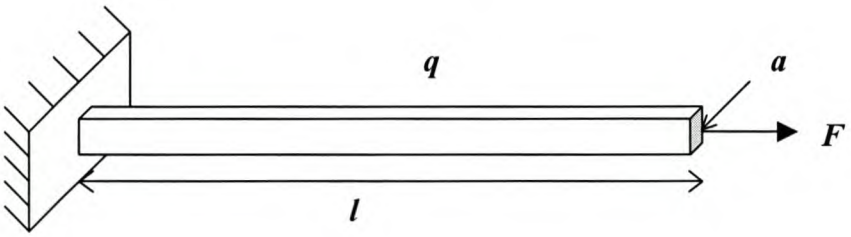

Fig. 2-10 Axially loaded rectangular steel bar of uniform cross-section

To solve the problem using the finite element method, the first step is to divide the bar into ***n*** parts, say five parts in this particular example. Then we have five line elements each having a length of ***l/5*** and six nodes having a single degree of freedom each. For convenience of computer coding and problem handling, the elements and nodes are labelled with numbers starting from some point. If we start labelling at the fixed end of the bar, the element at the free end will be element ***5***, and the node at the same point is 6 as in figure 2.11. The elements are labelled with italicised numbers for easy differentiation from the node labelling in the figure. All parameters related to any of the elements are labelled with the respective label of the element or node.

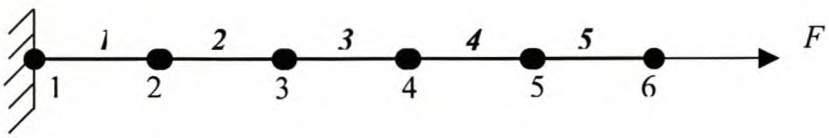

Fig. 2-11 Line element model of a bar

2.3.2.2 Element Governing Equations

Suppose we consider element *i*, having a length ***L***, one-fifth of the bar length ***l***, ***l/5*** = ***L***, and we want to determine the one-dimensional, linear displacement of the element. Let the axial displacement be along axial axis ***s***.

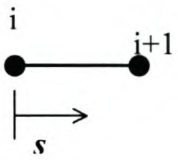

Fig. 2-12 Generic element

The displacement of the element is approximated by a sum of polynomials satisfying the essential boundary conditions and continuous along the element axis. By observing the nature of the problem, a complete linear function can be appropriate as an approximating polynomial since it is continuous along the length of the bar and can satisfy the boundary conditions. Then the displacement function, the problem in question, should be expressed as a linear function of the axial displacement and the nodal values of the element.

Let

$u = a_1 + a_2 s$ … a

or

$$u = \lfloor 1 \quad s \rfloor \begin{Bmatrix} a \\ a_2 \end{Bmatrix} \quad \ldots \text{b}$$

... 2-37

be the approximating polynomial with values $u = u_i$ at $s = 0$ and $u = u_{i+1}$ at $s = L$. It is easy to see that ***u*** is continuous in the element domain and satisfies the essential boundary values.

$$\begin{Bmatrix} u_i \\ u_{i+1} \end{Bmatrix} = \begin{bmatrix} 1 & 0 \\ 1 & L \end{bmatrix} \begin{Bmatrix} a_1 \\ a_2 \end{Bmatrix} \quad \ldots \text{a}$$

or

$\{d\} = [A]\{a\}$ … b

... 2-38

Solving for $\{a\}$

$$u = \begin{bmatrix} \frac{L-s}{L} & \frac{s}{L} \end{bmatrix} \begin{Bmatrix} u_i \\ u_{i+1} \end{Bmatrix} \quad \ldots \text{a}$$

$$u = [N]\{d\} \quad \ldots \text{b}$$

... 2-39

$[N]$ is called the shape function matrix. It describes how ***u*** is to be interpolated from the nodal values of the element. One way to find the shape function or interpolation function of elements is using *Lagrange's Interpolation Formula.*

The axial or normal strain of a bar element of length ***L*** lying along the ***s*** axis is given by equation (2.9)

$$\varepsilon_s = \frac{du}{ds} \quad \textbf{... 2-40}$$

Substituting ***u*** from equation (2.39)

$$\varepsilon_s = [B]\{d\} \quad \ldots \text{a}$$

Where

$$[B] = \frac{d}{ds}[N] = \begin{bmatrix} -\frac{1}{L} & \frac{1}{L} \end{bmatrix} \quad \ldots \text{b}$$

... 2-41

$[B]$ is the strain-displacement matrix.

From equation (2.36) the potential energy due to straining of a bar having area ***A*** and modulus of elasticity ***E*** is

$$\Pi_s = \tfrac{1}{2}\int_0^L \varepsilon_x^T AE\varepsilon_x ds = \tfrac{1}{2}\{d\}^T[k]\{d\} \quad \textbf{... 2-42}$$

Comparing equations (2.40) and (2.41), the element stiffness matrix is given by

$$[k] = \int_0^L [B]^T AE[B] ds \quad \textbf{... 2-43}$$

The element potential energy due to element body force is, from equation (2.36),

$$\Pi_b = -\int_0^L ufAds = -\int_0^L u^T qds \quad \textbf{... 2-44}$$

Where $f = \frac{q}{A}$ is the force per unit volume.

$$\Pi_b = -\{d\}^T \{r_e\} \quad \textbf{... a}$$

Where

$$\{r_e\} = \int_0^L \lfloor N \rfloor^T qds \quad \text{... b}$$

... 2-45

is the element consistent load vector, which explains how the distributed load is to be allocated to the element nodes in a way consistent with the displacement field assumed.

And the potential energy due to nodal forces is given by, from equation (2.36),

$$\Pi_n = \{d\}^T \{p\} \quad \textbf{... 2-46}$$

Where $\{p\}$ is the element nodal force vector.

Thus, the element stiffness matrix and all the accompanied loads are solved.

2.3.2.3 Structural Assembly

After solving the necessary variables, the stiffness matrix, the displacement vector, the nodal loads, etc, for a single element, the next step is to assemble all the elements to form the complete structure. First, the structural degree of freedom is calculated from the number of elements and the degree of freedom of each element. Then the element degree of freedom is expanded to the total structural degree of freedom with appropriate assignment of each entry. The matrices of each element are added to form the global matrix of the structure, with overlapping entries added.

For the above example of bar modelling, the structural degree of freedom is 6 and the total potential energy of the bar is the sum of the potential energy of each element.

$$\Pi_T = \Pi_1 + \Pi_2 + \Pi_3 + \Pi_4 + \Pi_5 \quad \textbf{... 2-47}$$

Taking the length of each element to be L, and AE constant over the entire length, the potential energy for the bar is given below as the sum of the potential energy of each element.

$$\Pi_T = \frac{1}{2}\{D\}^T \left(\frac{AE}{L} \begin{bmatrix} 1 & -1 & .. & .. & .. \\ -1 & 1 & .. & .. & .. \\ .. & .. & .. & .. & .. \\ .. & .. & .. & .. & .. \\ .. & .. & .. & .. & .. \end{bmatrix}_{6\times6} + \frac{AE}{L} \begin{bmatrix} .. & .. & .. & .. & .. \\ .. & 1 & -1 & .. & .. \\ .. & -1 & 1 & .. & .. \\ .. & .. & .. & .. & .. \\ .. & .. & .. & .. & .. \end{bmatrix}_{6\times6} + \ldots \right.$$

$$\left. + \frac{AE}{L} \begin{bmatrix} .. & .. & .. & .. & .. \\ .. & .. & .. & .. & .. \\ .. & .. & .. & .. & .. \\ .. & .. & .. & 1 & -1 \\ .. & .. & .. & -1 & 1 \end{bmatrix}_{6\times6} \right) \{D\}$$

$$- \{D\}^T \frac{qL}{2} \left(\begin{Bmatrix} 1 \\ 1 \\ .. \\ .. \\ .. \end{Bmatrix}_{6\times1} + \begin{Bmatrix} .. \\ 1 \\ 1 \\ .. \\ .. \end{Bmatrix}_{6\times1} + \ldots + \begin{Bmatrix} .. \\ .. \\ .. \\ 1 \\ 1 \end{Bmatrix}_{6\times1} \right)$$

$$- \{D\}^T \left(\begin{Bmatrix} .. \\ .. \\ .. \\ .. \\ .. \end{Bmatrix}_{6\times1} + \ldots + \begin{Bmatrix} .. \\ .. \\ .. \\ .. \\ F \end{Bmatrix}_{6\times1} \right) \qquad \ldots \text{a}$$

Taking the force per length, ***q***, constant along the length of the bar and a single axial point load at the free end of the bar the assembled matrix will be a single 6x6 stiffness matrix and a single 6x1 nodal force vector as given below.

$$\Pi_T = \frac{1}{2}\{D\}^T\left(\frac{AE}{L}\begin{bmatrix}1 & -1 & 0 & 0 & 0 & 0\\ -1 & 2 & -1 & 0 & 0 & 0\\ 0 & -1 & 2 & -1 & 0 & 0\\ 0 & 0 & -1 & 2 & -1 & 0\\ 0 & 0 & 0 & -1 & 2 & -1\\ 0 & 0 & 0 & 0 & -1 & 1\end{bmatrix}\right)\{D\} - \{D\}^T\left(\frac{qL}{2}\begin{Bmatrix}1\\2\\2\\2\\2\\1\end{Bmatrix}\right) - \{D\}^T\begin{Bmatrix}0\\0\\0\\0\\0\\F\end{Bmatrix}$$

... b

Where

$$\{D\}^T = \lfloor u_1 \quad u_2 \quad u_3 \quad u_4 \quad u_5 \quad u_6 \rfloor \quad \ldots \text{c}$$

2.3.2.4 Application of Boundary Conditions

Boundary conditions on the assembled structure are imposed by forcing the entries of the required degree of freedom in the characteristic matrix of the structure to be zero. In the above example, one end of the bar is fixed, the node with the first entry. That is, the degree of freedom at that point must be zero, $u_1 = 0$. This is done by striking out the first row and the first column of the structure stiffness matrix. The first entry of the structural degree of freedom in the vectors is also discarded. The expression of the total potential energy of the bar model is then given by

$$\Pi_T = \frac{1}{2}\{D\}^T\left(\frac{AE}{L}\begin{bmatrix}2 & -1 & 0 & 0 & 0\\ -1 & 2 & -1 & 0 & 0\\ 0 & -1 & 2 & -1 & 0\\ 0 & 0 & -1 & 2 & -1\\ 0 & 0 & 0 & -1 & 1\end{bmatrix}\right)\{D\} - \{D\}^T\left(\frac{qL}{2}\begin{Bmatrix}2\\2\\2\\2\\1\end{Bmatrix}\right) - \{D\}^T\begin{Bmatrix}0\\0\\0\\0\\F\end{Bmatrix}$$

... d

... 2-48

2.3.3 General Comments on the Finite Element Method

Generally speaking selecting appropriate finite element entities depends on the nature of the problem at hand. That is, the choice of an appropriate functional, the interpolating function to use,

the nature of elements to select, all depends on the nature of the problem to solve. But, the principles of problem handling using the finite element method are the same, which can be summarised by the following points.

- Selecting an appropriate functional
- Finding an admissible interpolating function within an element, interpolated from the nodal degrees of freedom of the element.
- Evaluating the functional in terms of nodal degrees of freedom using the principle of stationary point, which results in expressions for the element stiffness matrix and force vectors in terms of nodal degrees of freedom. The element matrix may have different names for different problem types.

In the study of elastic property of materials, for example, the appropriate functional for a Rayleigh-Ritz solution, a numerical solution technique by a stationary principle using approximating functions, is the expression of potential energy, Π_p. The expression of total potential energy in an elastic body is

$$\Pi_p = \int_v \left(\tfrac{1}{2}\{\varepsilon\}^T[E]\{\varepsilon\} - \{\varepsilon\}^T[E]\{\varepsilon_o\} + \{\varepsilon\}^T\{\sigma_o\} - \{u\}^T\{F\}\right)dV - \int_s \{u\}^T\{\Phi\}dS - \{D\}^T\{P\} \quad \ldots \text{a}$$

Where $\{u\}$ - Displacement field

$\{\varepsilon\}$ - Strain field

$[E]$ - Material property matrix

$\{\varepsilon_o\}, \{\sigma_o\}$ - Initial strains and stresses

$\{F\}$ - Body forces

$\{\Phi\}$ - Surface tractions

Or

$$\Pi_p = \tfrac{1}{2}\{D\}^T[K]\{D\} - \{D\}^T\{R\} \quad \ldots \text{b}$$

Where $\{K\}$ - Global stiffness matrix

$\{R\}$ - Global nodal consistent force vector

$\{D\}$ - Global nodal degrees of freedom

Taking the stationary point of equation (2.48) with respect to the nodal degrees of freedom yields a set of algebraic equations in terms of the stiffness matrix and the nodal degrees of freedom.

$$[K]\{D\} = \{R\} \quad \text{... 2-50}$$

Equation (2.50) is an expression that relates the elastic property of the structure with its nodal values. Since the property of elements is calculated by numerical approximation, the following remarks can be drawn:

- The equilibrium and compatibility conditions are satisfied at nodes.
- Across the inter-element boundaries the compatibility and equilibrium conditions may or may not be satisfied.
- Inside an element compatibility condition is satisfied, but equilibrium not usually.

In any finite element approximation method the solution should be closer to the theoretical the finer the mesh gets. To assure this criterion is fulfilled, the following requirements should be met:

- the interpolating field, φ, must be complete.
- across inter-element boundaries, φ through its ***m-1*** derivatives should be continuous, where φ is of order ***m***.
- for elements in a mesh, if boundary conditions on the mesh is appropriate to a constant value of the $\boldsymbol{m^{th}}$ derivative of φ, then each element must display that constant value as the mesh is refined.

For computer coding and robust usage of the finite element method, a parametric system is usually used instead of the actual size of finite elements of structures.

2.3.4 Finite Element Package Used

The finite element package used for numerical analysis in this research is MSC NASTRAN for Windows v4.

MSC NASTRAN for Windows (MSC/N4W) is a finite element modelling and post-processing system that allows the user to perform engineering analyses both quickly and confidently. FEMAP is used as the modeller and NASTRAN as the finite element solver. It provides the capability to

develop sophisticated analyses of stress, temperature and dynamic performance directly on the desktop.

MSC/N4W provides the integration that is necessary to link all aspects of finite element analysis. It can be used to create geometry, or you can import CAD geometry. MSC/N4W then provides powerful tools for meshing geometry, as well as applying loads and boundary conditions. It has the capability to export an input file to many finite element codes for analysis. MSC/N4W can then read the results from the solver program.

Once results are obtained in MSC/N4W, a wide variety of tools are available for visualising and reporting the results.

2.3.5 Conclusion

The total concept of this part is to give a short explanation of the theoretical base behind the finite element package used. The complete procedure of the finite element problem formulation is incorporated in a user-friendly way in the MSC NASTRAN for Windows software package. The user is required to apply the relevant conditions that simulate the physical nature of the problem at hand and appropriate finite element concepts in handling the problem in question.

There are different options of modellers, interpolating methods, solvers and other features incorporated in the MSC NASTRAN for Windows package that enables the user choice to his/her satisfaction. But, it is good to stick to the default unless the user is sure of his/her selections.

This part concludes the theoretical basics that are needed to handle the practical and finite element analysis method needed in this thesis. Equipped with the necessary theoretical principles needed to handle the thesis, the next chapters will be devoted in total to the practical work and the finite element method analysis. In chapter 3, the equipment used in the test and the complete experimental set-up are summarised.

Chapter 3 INSTRUMENTATION AND SET-UP

The set-up and preparation of the experiment was quite tiresome and time-consuming. Most of the preparation is work devoted to strain gauge bonding and curing. The inconvenience of the locations where the gauges were bonded and the working conditions contributed significant effort to the experimental set-up and experimentation. Leaving all the accounting of time and energy spent to the experience of the author, this part of the report outlines the materials and instruments used in the testing.

Different sensors, measuring instruments and data recorders were used as means of data acquisition and analysis equipment in addition to the main test piece. The nature of the materials and their function is briefly discussed here for the sake of getting some insight of the equipment. The set-up and experimental procedure is also discussed to give a general idea of the testing conditions.

3.1 Instruments Used

The test piece was a 12.2m long inter-link semi-trailer. It was a double-axle heavy duty semi-trailer with a payload of 9 tonnes per axle. The dimensional drawing of the trailer is given in appendix D.

Fig. 3-1 Semi-trailer used as a test piece in the experiment

3.1.1 Strain Gauges

Electrical strain gauges are electrical conductors that change their resistance with the change of the length of the conductor. For sensing the small deformation of the parts of the test-piece, electrical strain gauges were bonded at selected parts of the semi-trailer. All the strain gauges used were approximately of 120Ω resistance, and of gauge factor 2 on average. The full description of the strain gauges used is given in table 3.1.

	Gauges used in the experiment					
No	Material	Type	Length (mm)	Resistance (Ω)	Factor	Qnt.
1	Steel	Uni-axial	1	120.2	2.1	9
2	Steel	Uni-axial	1	120.2	2.09	2
3	Steel	Uni-axial	2	120.2	2.14	4
4	Steel	Uni-axial	1	119.8	2.14	1
5	Steel	Uni-axial	10	119.8	2.14	7
6	Steel	Rosette	6	119.8	1.95;1.95;1.97	1
7	Steel	Rosette	6	120.2	1.95;1.95;1.97	3
8	Aluminium	Uni-axial	5	120.0	2.18	3

Table 3-1 Specification of strain gauges used in the test

3.1.2 Strain Gauge Conditioning Amplifiers

A group of Vishay 2300 series strain gauge conditioning amplifiers were used to amplify the low-level signals from the strain gauges. Vishay 2300 series amplifiers are multi-channelled signal amplifiers for conditioning and amplifying low-level signals from strain gauges for display or recording on external equipment. Each 2300 Signal Conditioning Amplifier was separately powered through a multi-channelled rack adapter and electrically isolated from the others. The group of amplifiers used in the experiment, are shown in figure 3.2 assembled in a multi-channelled rack adapter.

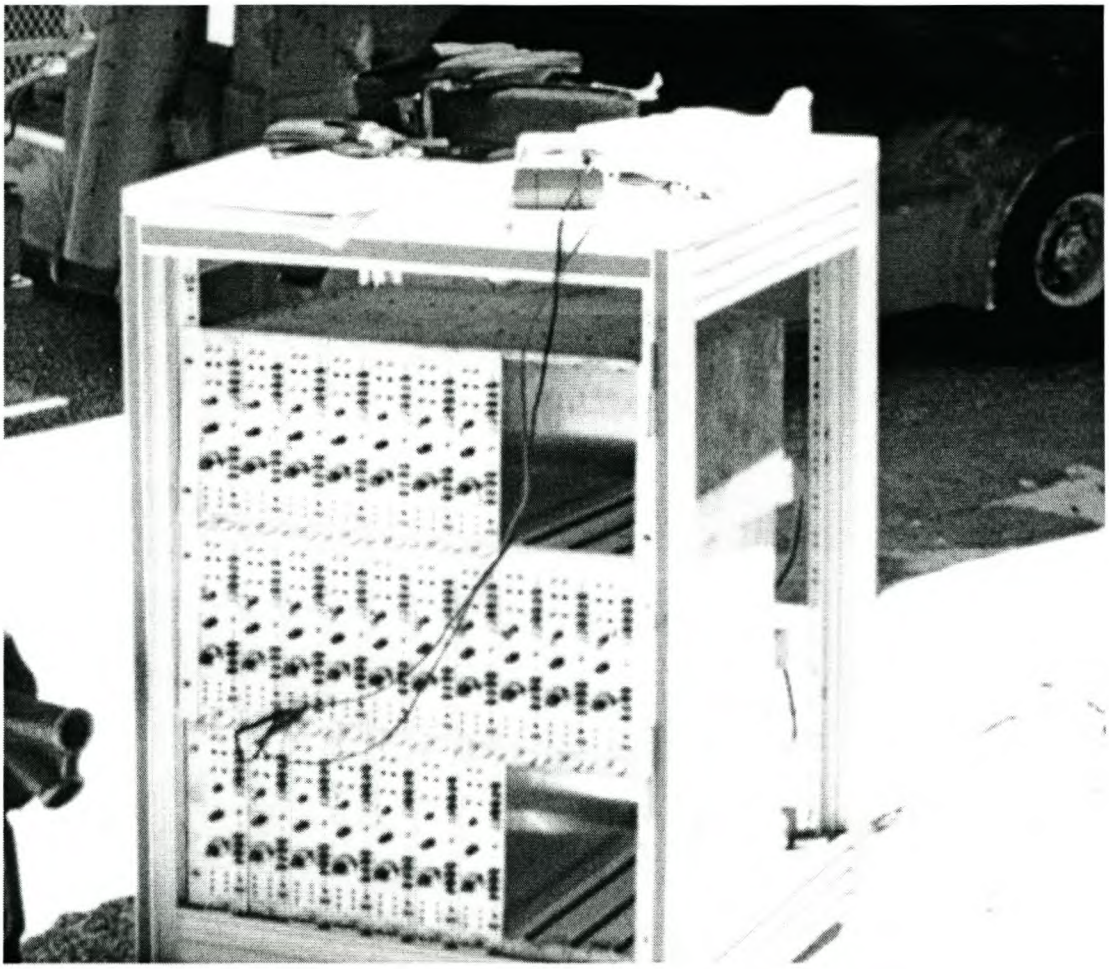

Fig. 3-2 Group of Vishay 2300 amplifiers in a rack adapter

This model incorporates precision high stability bridge completion resistors and dummy gauges, and four shunt-calibration resistors. It was designed for accurate stress analysis in a broad range of measurement applications.

- Fully adjustable calibrated gain
- Wide range of bridge excitation input
- Wide band of operating frequency
- Acceptance of all strain gauge inputs
- High input impedance
- Four-frequency active filter
- Dual-range automatic bridge balance

are some of the features that make the model convenient to use.

3.1.3 Calibration Box

An HBM K 3602 model pre-calibrated resistor bridge was used to calibrate the strain gauge reading. The bridge has a range of scaled readings. Each scale is pre-calibrated to give a specific micro-strain value when set at a particular mV/V reading. It is used to calibrate the strain gauges to give a specific micro-strain value for a given mV/V reading.

3.1.4 Digital Strain Meter

A P-3500 Model Strain Indicator was used to check the reading and circuit balance of the strain gauge bridges.

The P-3500 Model Strain Indicator is a portable, battery-powered precision instrument for use with 120Ω or 350Ω resistive strain gauges in full, ½ and ¼ -bridge inputs. It accepts gauge factors of 0.500 to 9.900, and the gauge factor is adjustable to an accuracy of 0.001. The model has all sorts of adjusting and calibrating buttons for easy operation. Indication signs or lights are also incorporated in the model for indicating the user's inputs and the working condition of the equipment. All readings are displayed on a liquid crystal display (LCD).

3.1.5 Digital Weight

Two digital weights and two load-cells were used to measure the weight-deflection curves of the gauges on the leaf springs.

3.1.6 Acceleration Transducers

HBM Model B 12 range of acceleration transducers or accelerometers were used to measure the vertical acceleration at some parts of the trailer. The Type B 12 acceleration transducers are instruments used to measure vibration and shock accelerations as well as constant acceleration. The model has an acceleration measuring range between $0.02 m/s^2$ and $200 m/s^2$. It is also intended to measure dynamic measurements up to 1 000Hz. Its excellent absolute zero stability is particularly suitable for constant and slowly changing accelerations. The accelerometers are easily mounted and compact instruments that measure quite a large range of accelerations.

3.1.7 Multi-Meter

A digital multi-meter with precision of 0.001V was used for checking the circuit and the values of the labelled resistance of the gauges.

3.1.8 Computer

Computers with PC30F and PC30G Series Eagle Cards were used as recording and data acquisition equipment during the experiments.

The PC30F and PC30G Series Boards are half-size, low cost, high accuracy analogue to digital I/O boards for the IBM PC/AT and compatible series of computers. The board has a monolithic A/D sub-system, which converts analogue voltage inputs from sensors to 12 bit digital codes. The A/D sub-system can accept 16 single-ended inputs simultaneously. The gain for each channel can be set independently to the different gains of the system.

The board has a sample-and-hold feature that results in a small time delay between each sampled piece of data. The time for sampling can be calculated from the maximum input frequency one intended to sample. In this particular experiment the time delay between each sample data was not of concern due to the low sampling frequency nature of the problem at hand, and it was not taken into consideration during sampling frequency selection.

The software used with the PC30F and PC30G Series Boards is WaveView. It is a powerful data acquisition and analysis package for the PC30 range of boards. It has a capacity of high streaming to disk and unique parallel board streaming. It can support the use of up to 3 boards simultaneously, with each board having its own configuration information, data sets, graphs and Fast Fourier Transforms. The number of samples acquired using streaming is limited only by the available disk space.

3.2 Hardware Set-up

3.2.1 Strain Gauges Set-up

A total number of 30 strain gauges were bonded to different parts of the semi-trailer body. The location of the strain gauges was arranged in approximately geometrically symmetric fashion. The gauges were fixed in parts of the trailer body where they were supposed to give fairly significant figures for relatively small disturbances. The locations were also selected at points where they were assumed to be key places for analysing the dynamics of the trailer for any arbitrary forcing functions.

One uni-axial gauge was installed at each spring-end at about 90mm from the end, on top and at the bottom side of each leaf spring. The gauges on each leaf spring were connected in a full bridge arrangement. The circuit connection in each set of gauges is such that the total deformation effect of the gauges add up. The full bridge circuit connection is given in figure 3.3 below.

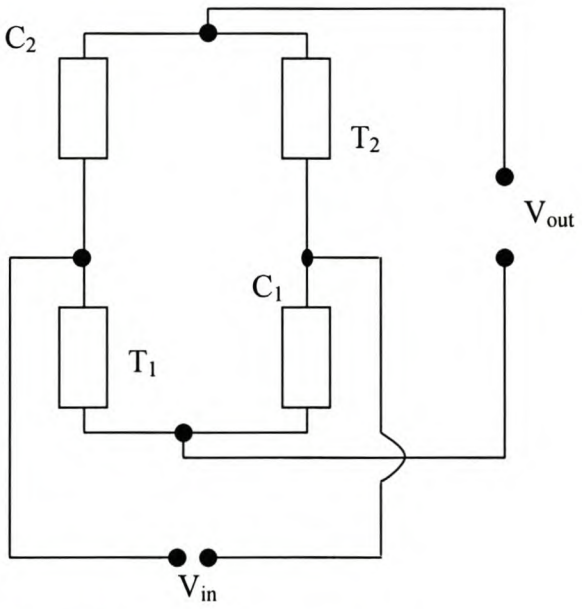

Fig. 3-3 Full bridge setting of the strain gauges

Where C_1 and C_2 are the strain gauges on the compressed sides of the leaf springs; and T_1 and T_2 are on the tension side.

From equation (A-4), in Appendix A,

$$\frac{V_{0ut}}{V_{in}} = \frac{K_{ave}}{4}(\varepsilon_{T_1} - \varepsilon_{C_1} + \varepsilon_{T_2} - \varepsilon_{C_2}) \quad \textbf{... 3-1}$$

K_{ave} is the average gauge factor of the four strain gauges in the bridge.

Three pairs of uni-axial gauges were bonded on the chassis of the trailer. The gauges in each pair were installed, one on each chassis, in geometrically symmetric position. The first pair was at 7 220mm on the web of the full (rear) part of the chassis. The second pair and the third pair were at 4940mm and 1990mm on the web of the tapered chassis, and on the bottom side of the lower flange of the neck of the chassis respectively. The distances of the gauge positions were measured from the front end of the trailer. All the gauges were attached to the outer surface of the parts of the chassis, except the gauge on the right side (from a rear view) of the full chassis web. The location of each gauge was at the geometrical middle of the chassis part where the gauges were bonded.

The gauges on the rear supporting plate were at 240mm from each edge and 45mm below the deck surface. The front supporting plate gauges were 370mm from each edge and 30mm above the surface of the deck, all on the outer surface of the trailer.

On the top beams, two rosette gauges where installed at the top and bottom sides of each beam. The perpendicular arms of the rosette gauges were connected in a full bridge. Similar to the leaf spring bridges, the full bridge circuit was in a way to read the combined deformation effect of the beams.

Quickset type strain gauge glue, adhesives especially manufactured for strain gauge bonding, was used to bond the strain gauges. All necessary care and treatment, as outlined in Appendix-A, was also given to the gauge bonding to avoid any stress relaxation at the time of testing. Every strain gauge was coated with M-coat A, a poly-urethane, to prevent any humidity or moisture effect, after bonding.

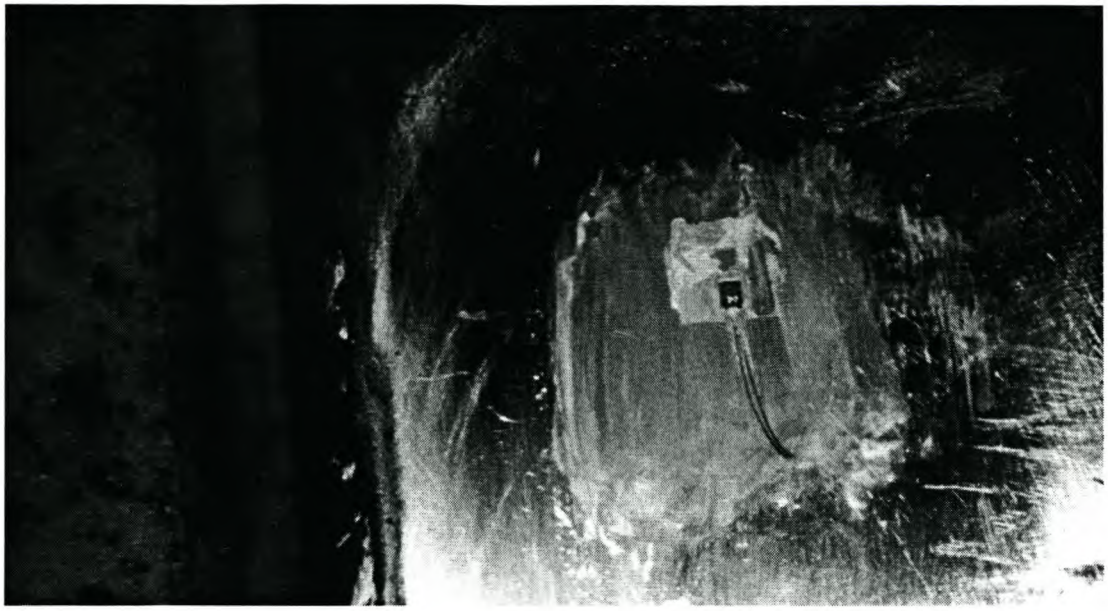

Fig. 3-4 Sample strain gauge bonded on the chassis web

When circuit connection was complete, the balance of each bridge and appropriate reading was checked. The gauges were covered with silicon to protect them from any external hazards, like sand and mud at the time of experimentation that may have resulted in their failure.

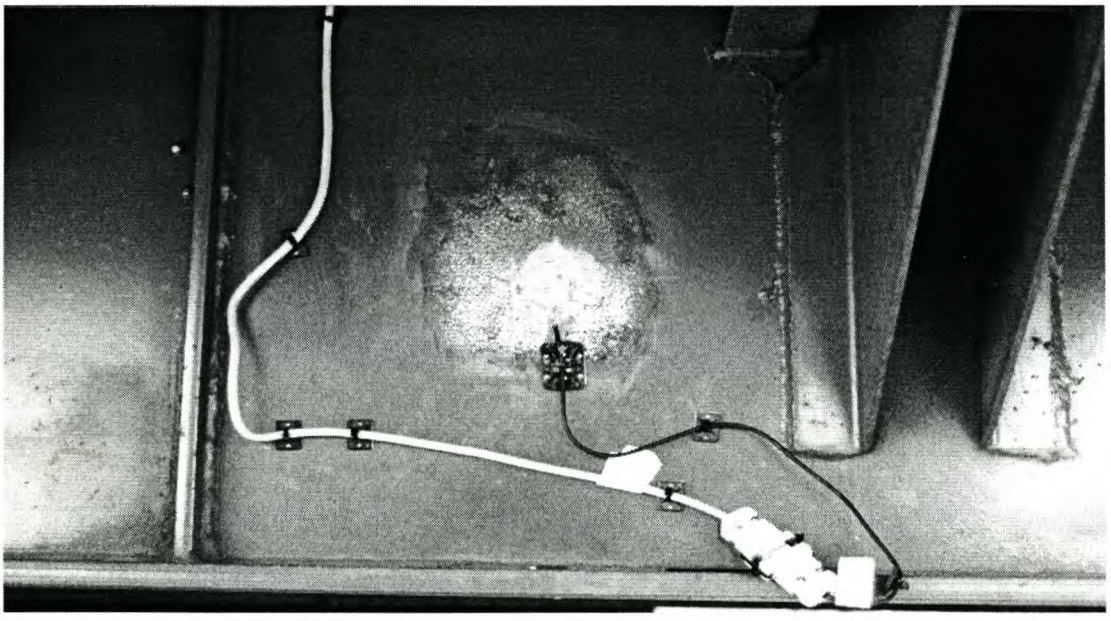

Fig. 3-5 Sample strain gauge on the tapered chassis web, fully connected and coated

3.2.2 Accelerometer Setting

Four acceleration transducers are installed to measure the response function, vertical acceleration of the trailer at some parts. One pair of accelerometers was installed on the lower flanges, right on top of the front axle, at 9 680mm from the front end. The second pair was installed at 3 500mm on the lower flanges of the chassis neck. All the accelerometers were fixed on the top surface of the lower flanges. Silicon glue was used to bond the accelerometers against the chassis steel bar.

3.3 Circuit Arrangement

A total of 16 strain gauge bridges were installed in the whole body of the trailer. Each strain gauge bridge was connected to a single 2300 model signal conditioning amplifier. An intermediate multi-interface adapter was used to connect the signal conditioning amplifiers to the PC30F and PC30G Series Eagle Board of the computer via a ribbon cable. Similarly the acceleration transducers were connected to a different set of amplifiers and a separate computer.

The total set, the two sets of computers and signal conditioning amplifiers, were tied up in a movable stand. The stand was temporarily welded on the front end of the trailer attached to the front supporting plate of the trailer. The whole arrangement was made so that it was possible to manipulate the recording and other adjustments while the trailer was moving. The location of the set was chosen to give enough space for the people manipulating the measurement setting and safe enough to keep the equipment and personnel stable during the experiment.

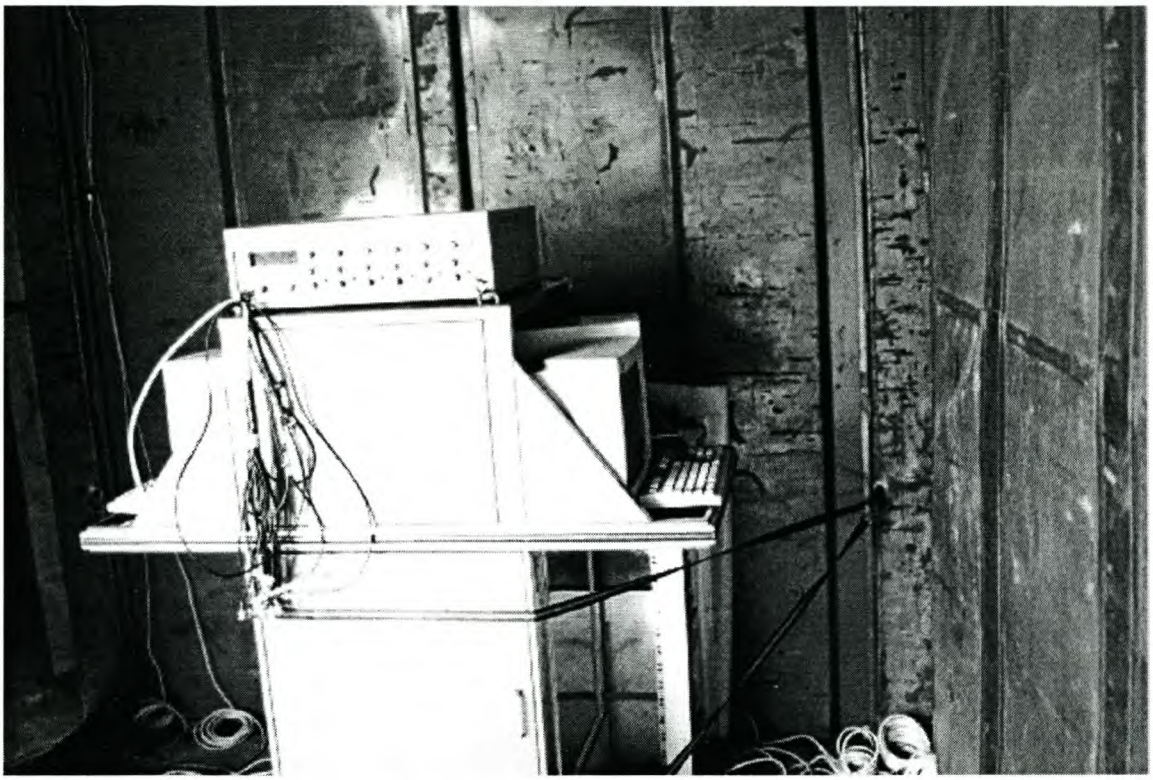

Fig. 3-6 The data recording and acquisition equipment on the semi-trailer packed in a stand

3.4 Software Setting

As mentioned above, the time-lag between each sample was not considered in this low frequency sampling test. WaveView has characteristics of summing up the frequency of the channels used. If two channels are needed to sample at a frequency of 10Hz, the frequency option in the software should be set at 20Hz. Taking this sampling nature of WaveView into consideration, and trying to get fairly optimum number of samples, a workable frequency for the trailer was approximated. 20 Hz was approximated as the maximum prevailing forcing frequency for moving trucks or trailers [20]. In accordance to Shannon-Nyquist's Sampling Theorem, the sampling frequency was set to 40Hz. Another assumption was taken that the mode shape of a signal having a frequency of 40Hz can be approximated well enough with eight sampling points.

Summing up all the above assumptions, the sampling frequency in the WaveView was set to 8*16*40 = 5120Hz, where the sampling time-interval was automatically calculated from the frequency.

3.5 Conclusion

The above information gives some idea of the general nature of the instruments used and their use in the test. The next chapter will deal with the experimentation and experimental results.

Chapter 4 EXPERIMENTATION AND TEST RESULTS

The test is to measure the influence of forces due to road profile on a truck trailer driven over a relatively rough road at different speeds and the resulting strain. The forces were measured at the suspension, at each spring, and the response strains at different parts of the semi-trailer. To enhance data interpretation and knowing the actual parameters of the readings of the strain gauges, the measuring instruments were first calibrated. The detail of the complete calibration data and experimental results of the test are outlined in this chapter.

4.1 Calibration of Instruments

4.1.1 Calibration of Gauges

Bridges used for measuring the input forces and response functions were calibrated in two different ways. The leaf spring bridges, the bridges that measure the forces from the tyres, were calibrated to give weight-deflection ratio curves. Two digital weights and two load cells were used to weigh the sand barrels that were loaded onto the trailer sequentially. The trailer was supported with two load cells at the axle ends, one axle at a time. A number of sand barrels were loaded, one by one, approximately on top of each tyre. The weight reading of each loaded barrel, from the digital weight and the mV/V deflection values of the respective bridge, from the Vishay 2300 model signal conditioning amplifiers was recorded. The same data was recorded when the sand barrels were unloaded in reverse order. The last loaded barrel was unloaded first.

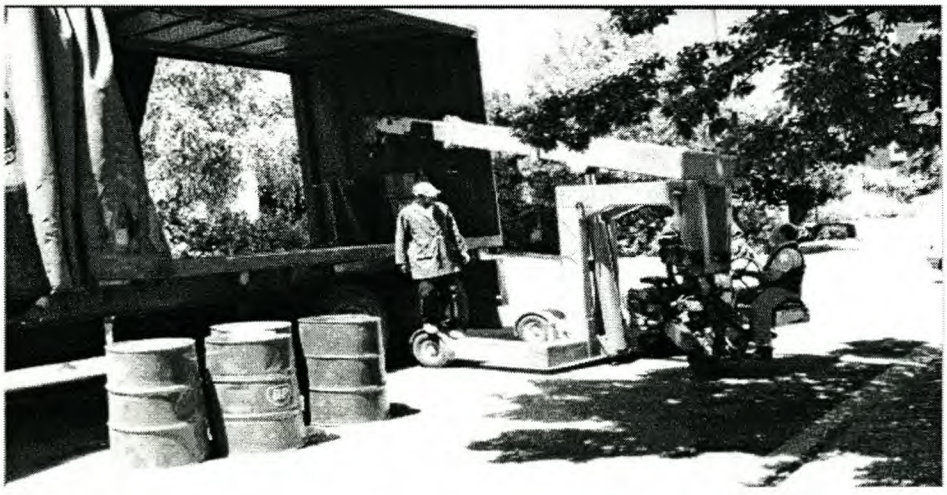

Fig. 4-1 Calibration of suspension of trailer using sand barrels

From the weight-deflection curve of the average values of the loading and unloading measurements, a calibration constant was calculated for each bridge. This constant was to be used to approximate the magnitude of the forcing function at the spring ends for a given mV/V reading. The suspension bridges calibration curves are given in figure 4.2.

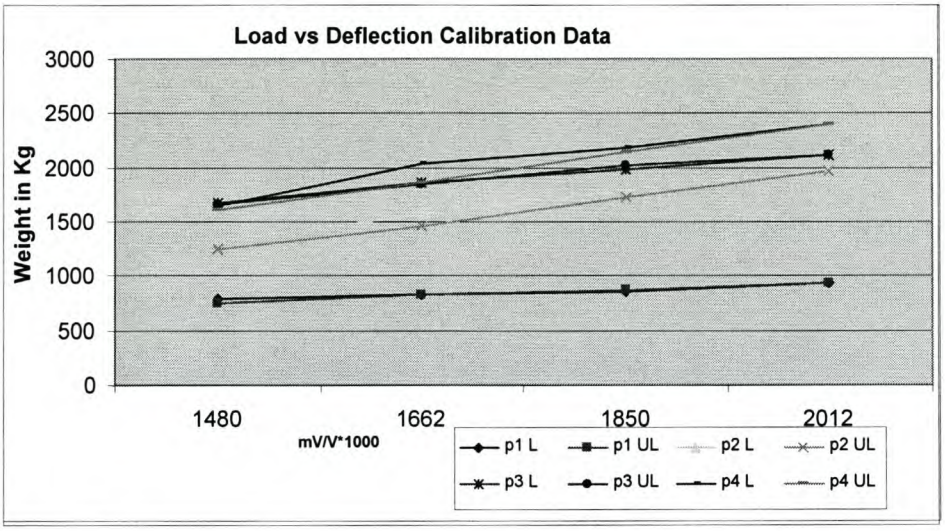

Fig. 4-2 Suspension calibration curves

Where P1 = Rear axle right tyre
P2 = Rear axle left tyre
P3 = Front axle right tyre
P4 = Front axle left tyre
And L – Loading
UL – Unloading

The bridges reading the response functions of the trailer, on the other hand, were calibrated using a pre-calibrated calibration box that has a gauge factor of 2. The box is tuned to read 1000με (1000 micro-strain) at 0.5mV/V scale, where the strain reading can be found using equation (A-1), in Appendix A , which is given below.

$$\frac{\Delta R}{R} = \frac{\Delta V}{V} = K\varepsilon \quad \textbf{... 4-1}$$

The calibration values for the response measuring bridges are given in table 4-1, to help further strain value manipulations.

Bridge Weight vs. Deflection Calibration Data				
Bridge label	Calibration reading per 0.5mV/V	Bridge Distance form the front end	Bridge Location	Comment
P1	1.034	Leaf-spring	Leaf-spring ends	Full bridge
P2	0.998	"	"	"
P3	1.008	"	"	"
P4	1.009	"	"	"
P5(2.14)	1.016	7220mm	Right side	Quarter bridge
P6(2.09)	1.002	7220mm	Left side	"
P7(2.14)	2.573	4940mm	Right side	"
P8(2.14)	1.093	4940mm	Left side	"
P9(2.14)	1.014	1990mm	Right side	"
P10(2.14)	1.001	1990mm	Left side	"
P11(2.09)	1.016	Rear end	Right side	"
P12(2.14)	1.055	Rear end	Left side	"
P13(2.14)	1.033	Front end	Right side	"
P14(2.14)	1.007	Front end	Left side	"
P15	1.074	6500mm	Right side	Full bridge
P16	1.031	6500mm	Left side	"

Table 4-1 Bridge locations and their calibration value

4.1.2 Acceleration Transducers Calibration

All accelerometers in the experiment were calibrated to give a reading of 1mV/V per 1g (gravitational acceleration), and were installed in a way to read the vertical acceleration of the trailer.

4.2 Input Force Sampling

4.2.1 Pallet Loading

Eight brick-pallets were loaded as a test weight on the semi-trailer. Each pallet had a dimension of approximately 1*1*1 m^3 and weighed 1.5 tons. Four of the pallets were loaded almost on top of each tyre. The remaining pallets were loaded approximately 300mm to the back and front from the middle of the semi-trailer deck.

Fig. 4-3 Pallet loading

Fig. 4-4 shows the data taken at the suspension of the semi-trailer during pallet loading.

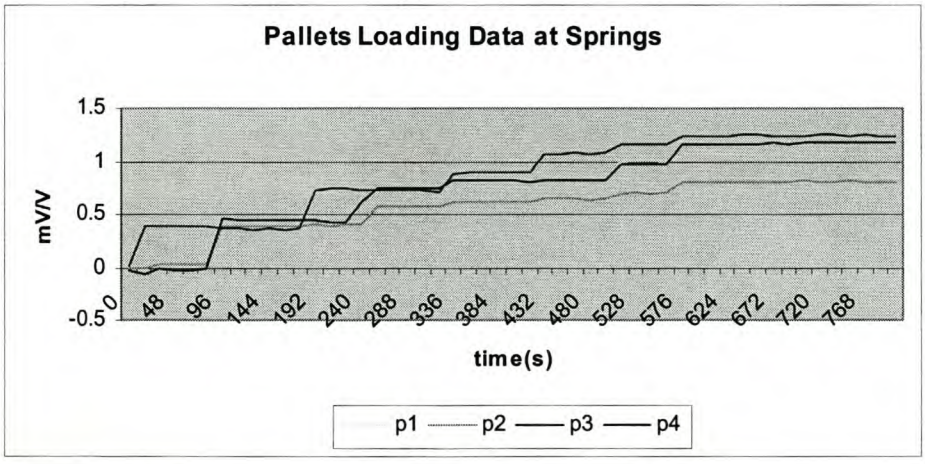

Fig. 4-4 Pallet loading data at the suspension part

Where p1 = rear axle right wheel spring

p2 = rear axle left wheel spring

p3 = front axle right wheel spring

p4 = front axle left wheel spring

4.2.2 Testing on Road Profile

Loaded with eight brick-pallets, the truck was driven on relatively rough off-road at different speeds. Three sets of samples were recorded, at 40km/h, 50km/h and 70km/h vehicle speeds. Two people controlled the computers on the deck of the semi-trailer. A person who watched the speed of the truck and estimated the profile of the road was in the truck cabin. When the vehicle accelerated to the required speed, the person in the cabin instructed the operators using two-way radio contact to start sampling. Similarly the same person instructed them to stop sampling when he assumed enough data had been recorded. The following forcing data inputs were sampled at the suspension of the semi-trailer for the three vehicle speed tests. The samples are part of the full sample of each sampled set. The plots are just to show the nature of the forcing functions for each test. A detailed record of the input functions is given in Appendix E.

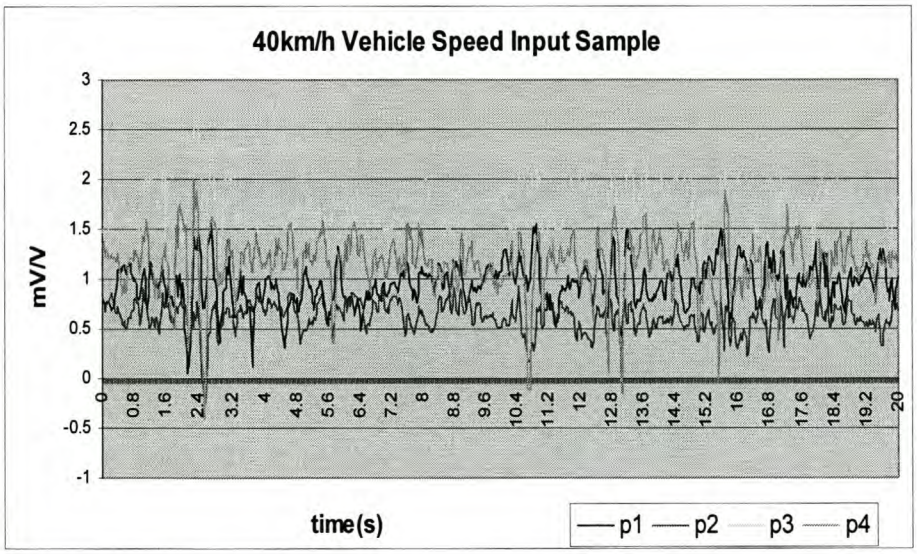

Fig. 4-5 Input force sample at 40km/h vehicle speed

Since it is more convenient to handle the dynamic and static forcing functions separately, the static part of the forcing function is filtered out; and normalised for mathematical discipline during both the experimental and finite element analysis. For easy visualisation of the magnitude of the

dynamic forcing function, sample plots of the static-filtered forcing input are given for the 50km/h and 70km/h speed tests below.

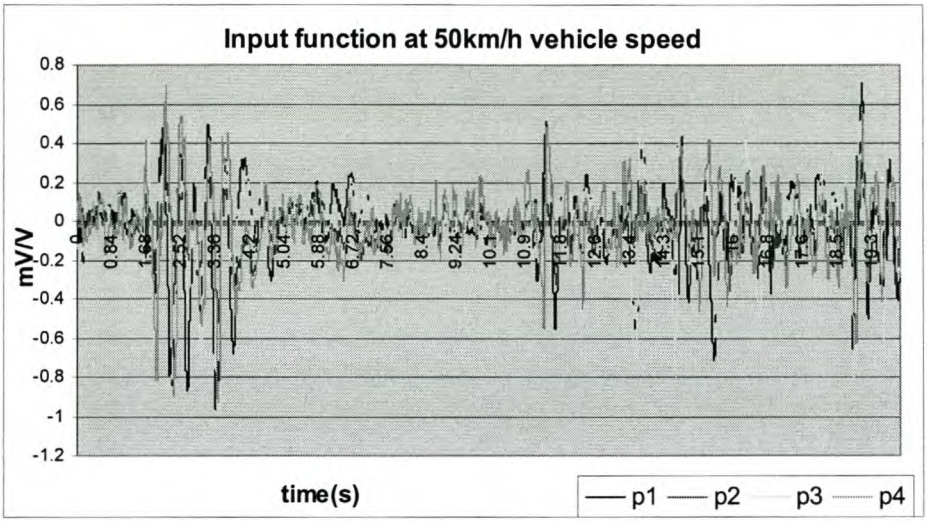

Fig. 4-6 Average filtered trailer dynamic input at 50km/h

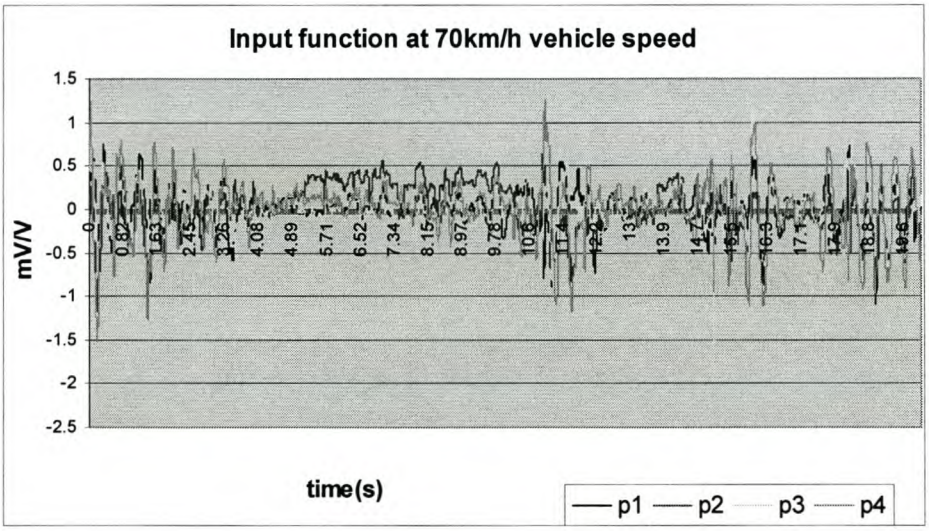

Fig. 4-7 Dynamic trailer input force at 70km/h

Where p1 – Rear axle right wheel spring

p2 – Rear axle left wheel spring

p3 – Front axle right wheel spring

p4 – Front axle left wheel spring

A fourth set of data was sampled as well for a curved road at a relatively low speed.

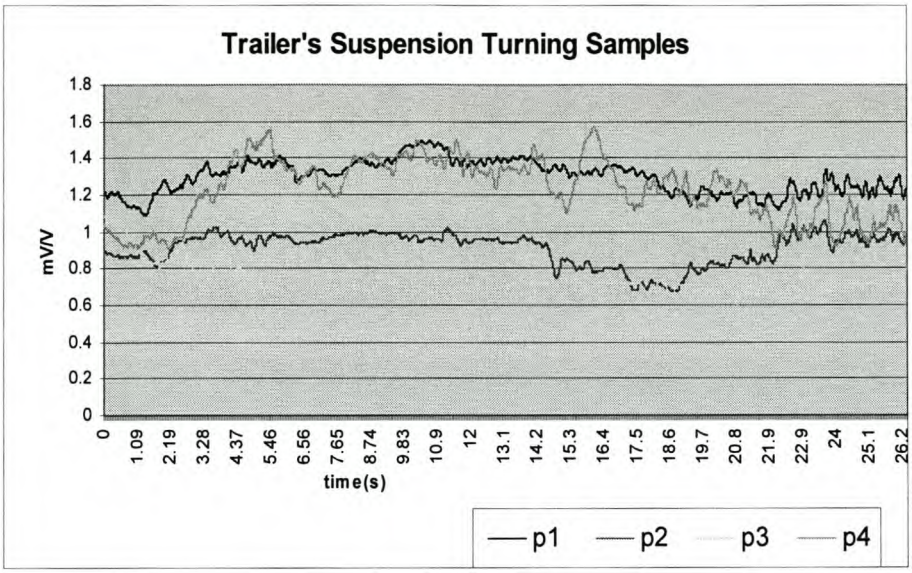

Fig. 4-8 Forcing inputs on a curved road

4.3 Measured Output Functions

4.3.1 Sample Output Data

The sampled output functions are all in mV/V (milli-Volt per Volt). Sample graphs of output functions are given in the following figures. Each figure contains sample data recorded for a time interval of 20s. The samples were arbitrarily selected, as examples of the output data only.

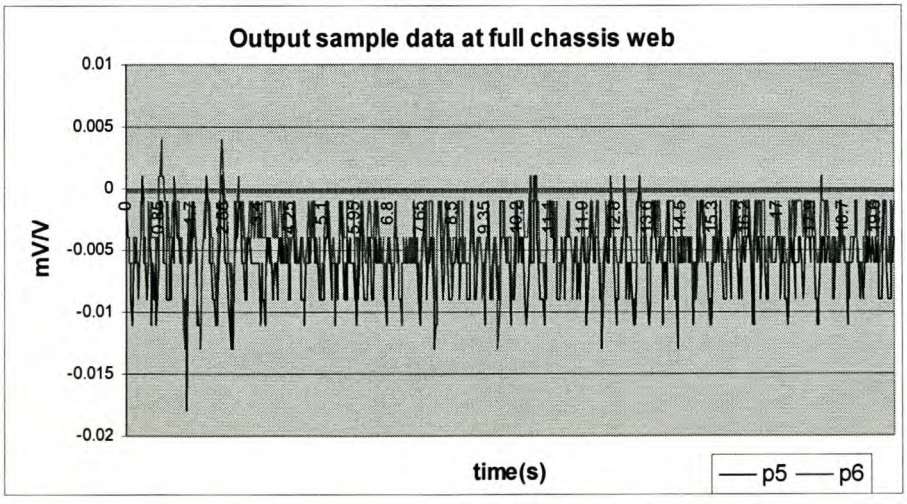

Fig. 4-9 Full chassis web response data at 40km/h vehicle speed

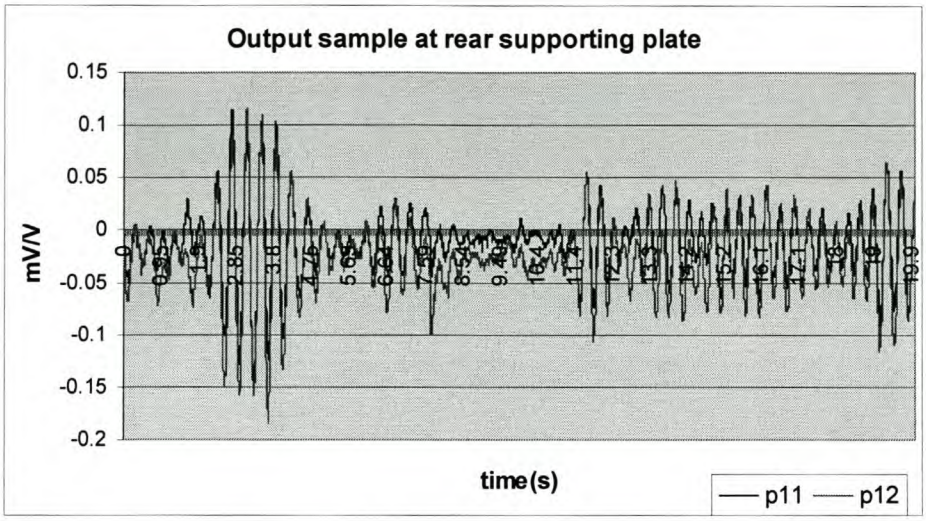

Fig. 4-10 Rear supporting plate sample response data at 50km/h vehicle speed

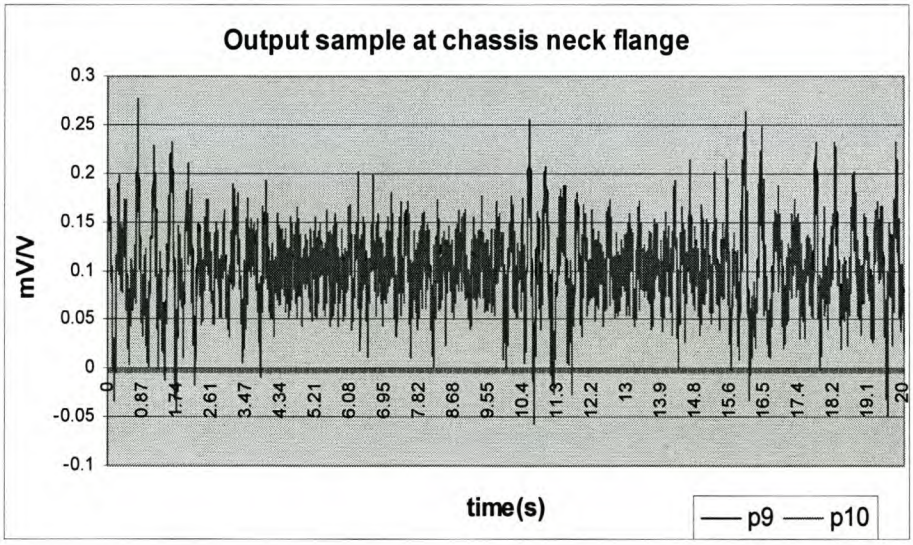

Fig. 4-11 Sample response data of chassis neck flange of semi-trailer at 70km/h vehicle speed

Note: The letter p with its accompanying number in the legend of the graph represents the name of the sampling point. The odd numbers represent the right side of the semi-trailer at the specified part and the even numbers represent the left side.

4.3.2 Experimentally Measured Strain and Accompanied Stress

The measured values of strain and the resulting stresses are given in this section for selected time intervals. Since the static values, the strain due to the dead weight of the trailer can be treated separately, only the values due to the dynamic forcing function are given here. That is, the mean values of all the tests are manually filtered out. Time intervals having relatively prominent output functions were selected from each test. Since these results are to be compared to the finite element analysis results in the next chapter, it is quite reasonable to select time intervals that have significant values. The strains are calculated from equation (4.2) with a little modification to include the calibration constants and gauge factor of each strain gauge bridge.

$$\frac{\Delta V}{V} = K\varepsilon \quad \text{... 4-2}$$

To put into account the gauge factor of each strain gauge, equation (4.2) is modified as below for the same bridge calibration constant (1 000με per 0.5mV/V).

$$\varepsilon = \frac{2R_g}{K_g C_g} \quad \text{... 4-3}$$

Where ε – Strain value

R_g Amplifier reading in mV/V

K_g Gauge factor of the specific bridge

C_g Bridge calibration constant

This was done to put into consideration a change in calibration constant and gauge factor of each bridge in calculating the strain value. As can be seen from table 4.1 some of the bridges have quite a significant difference in their calibration constants. Table 3.1 shows there is some difference in the gauge factor of the strain gauge used as well.

The stresses are calculated for equation (2.11), taking the strain as uni-axial strain in the direction of the strain gauge length.

$$\sigma = E\varepsilon \quad \text{... 4-4}$$

This approximation may overestimate the strain as well as the stress values in parts which are relatively flexible, although the strain gauge positions are believed to have been at points where there is no excessive bending, to be on the save side for the above assumption. Anyway, the stress values will be compared to the finite element analysis stresses calculated for a two dimensional domain.

The strains and stresses tabulated below are values to be compared with the finite element analysis results. The values were tabulated at intervals of two and half seconds. Short time interval values are preferred, because it is more expensive to run the finite element analysis if longer time intervals are taken.

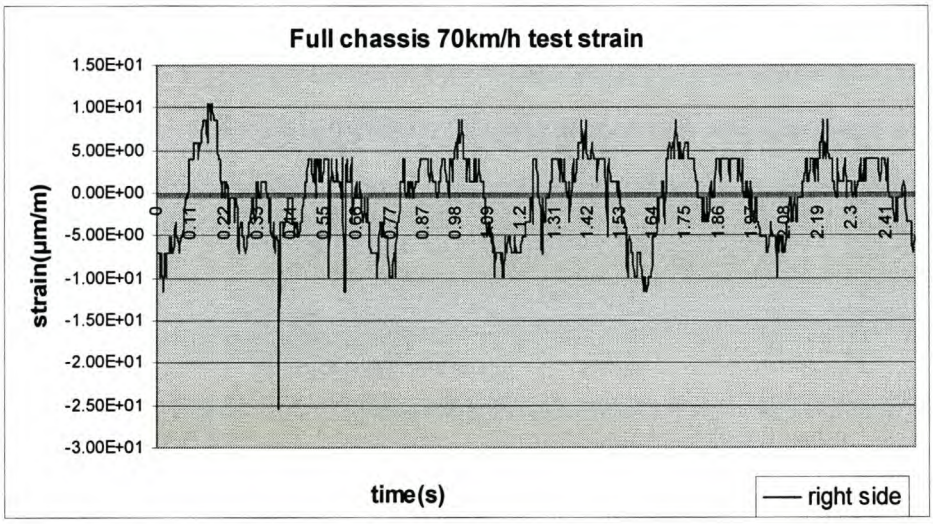

Fig. 4-12 Experimental strain plot of right side full chassis web at 70km/h between 0 and 2.5s

Strain standard deviation value of 2.5 seconds of the 70km/h test (µm/m)						
	Full chassis		**Tapered part**		**Neck flange**	
Time(s)	**Right**	**Left**	**Right**	**Left**	**Right**	**Left**
0-2.5	3.78	3.14	2.86	2.75	40.4	41.7
10-12.5	3.02	3.04	3.36	2.55	32.5	33.4
17-19.5	2.9	2.62	2.64	1.91	26.4	28.4

Table 4-2 Chassis sample strain values at 70km/h vehicle speed

Stress standard deviation value of 2.5 seconds of the 70km/h test (MPa)						
	Full chassis		Tapered part		Neck flange	
Time(s)	Right	Left	Right	Left	Right	Left
0-2.5	0.756	0.628	0.572	0.551	8.083	8.337
10-12.5	0.604	0.607	0.673	0.511	6.494	6.677
17-19.5	0.579	0.525	0.527	0.384	5.278	5.680

Table 4-3 Chassis sample stress values at 70km/h vehicle speed

Strain standard deviation value of 2.5 seconds of the 70km/h test (μm/m)				
	Rear supporting plate		Front supporting plate	
Time(s)	Right	Left	Right	Left
0-2.5	34.8	37.5	17.8	9.81
10-12.5	30.3	31.6	17.8	8.47
17-19.5	32.4	36.6	18.4	12.5

Table 4-4 Supporting plate strain values at 70km/h vehicle speed

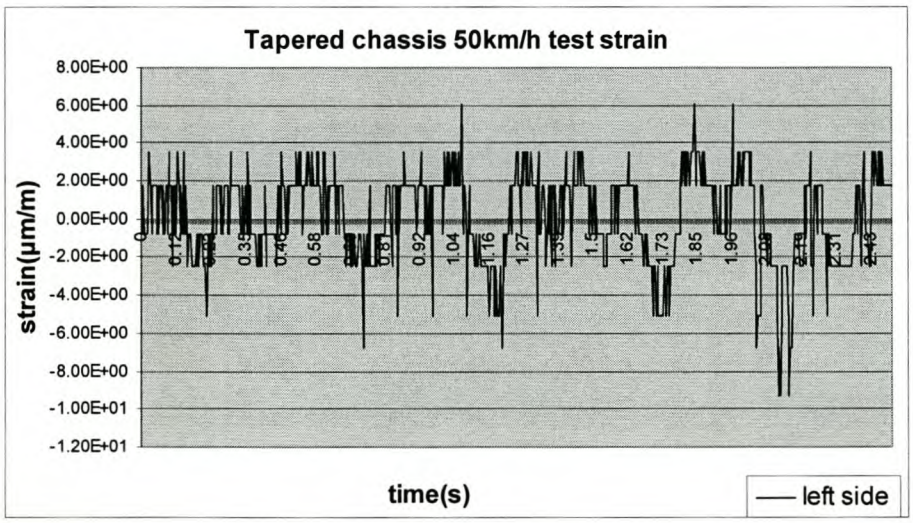

Fig. 4-13 Tapered chassis web strain plot at 50km/h for the interval 13-15.5s

Strain standard deviation value of 2.5 seconds of the 50km/h test (μm/m)						
	Full chassis		Tapered part		Neck flange	
Time(s)	Right	Left	Right	Left	Right	Left
2-4.5	3.3	3.43	2.14	2.76	35.2	37
11-13.5	1.74	1.66	1.33	1.64	17.7	20.8
13-15.5	2.65	2.43	1.94	2.03	26.6	28.7

Table 4-5 Chassis strain values at 50km/h vehicle speed

Stress standard deviation value of 2.5 seconds of the 50km/h test (MPa)						
	Full chassis		Tapered part		Neck flange	
Time(s)	Right	Left	Right	Left	Right	Left
2-4.5	0.659	0.685	0.427	0.552	7.043	7.394
11-13.5	0.348	0.332	0.266	0.328	3.543	4.153
13-15.5	0.531	0.487	0.387	0.407	5.332	5.740

Table 4-6 Chassis sample stress values for the 50km/h vehicle speed

Strain standard deviation value of 2.5 seconds of the 50km/h speed (μm/m)				
	Rear supporting plate		Front supporting plate	
Time(s)	Right	Left	Right	Left
2- 4.5	55.6	57.7	29.4	17.6
11- 13.5	20.4	23.1	15.4	75.9
13-15.5	21.4	25.8	13.9	80.1

Table 4-7 Supporting plate sample strain reading for the 50km/h vehicle speed

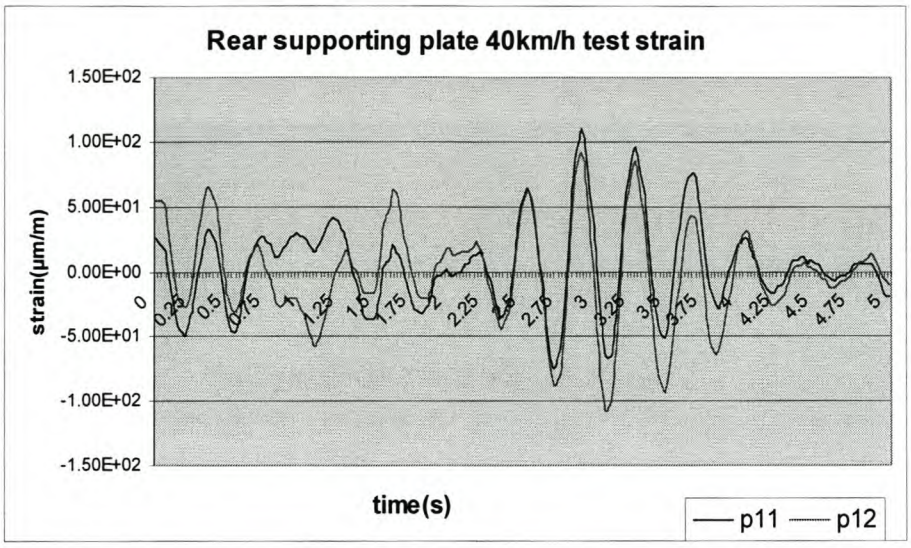

Fig. 4-14 Rear supporting plate sample strain reading for the 40km/h between 0-5s

Strain standard deviation value of 5 seconds of the 40km/h test (µm/m)						
	Full chassis		**Tapered chassis**		**Chassis neck flange**	
Time(s)	**Right**	**Left**	**Right**	**Left**	**Right**	**Left**
0-5	2.08	2.08	2.56	1.73	23.3	27.3
10-15	2.1	1.95	2.06	1.64	22.1	26
15-20	1.61	1.71	1.97	1.56	16.8	20.2

Table 4-8 Chassis sample strain values for the 40km/h vehicle speed

Stress standard deviation value of 5 seconds of the 40km/h test (MPa)						
	Full chassis		**Tapered chassis**		**Chassis neck flange**	
Time(s)	**Right**	**Left**	**Right**	**Left**	**Right**	**Left**
0-5	0.417	0.416	0.512	0.346	4.658	5.463
10-15	0.421	0.389	0.412	0.327	4.415	5.208
15-20	0.323	0.341	0.394	0.312	3.365	4.035

Table 4-9 Chassis sample stress values for the 40km/h vehicle speed

Strain standard deviation value of 2.5 seconds of the 50km/h test (μm/m)				
	Rear supporting plate		Front supporting plate	
Time(s)	Right	Left	Right	Left
0-5	25.5	29	15.8	7.68
10-15	19.9	23.7	16.1	6.7
15-20	15.1	17.4	12.5	4.65

Table 4-10 Supporting plate sample strain reading for the 40km/h vehicle speed

4.4 Conclusion

As can be seen from the plots of the experimentally measured data in Appendix E, most of the strain gauges gave usable data. Strain gauges at the right front supporting plate and right tapered chassis part seems to have been defective. The left side gauge of the chassis neck was also a bit unstable. As a reference to the finite element results at the defective strain gauge points, their symmetric counter parts are to be used.

Having these test results at hand, the next chapter will deal with finite element analysis results at the same intervals, as the aim of the paper is to verify how reliable the numerical analysis results would be in analysing or redesigning a structure. The finite element model will be tested for its results at the same intervals as the test results.

Chapter 5 FINITE ELEMENT ANALYSIS METHOD

The complete modelling, geometry and the finite element entities, was done in MSC NASTRAN for Windows V4. Except for small changes made, like ignoring some appendages having no contribution to the overall stiffness of the structure, the geometry was modelled with the exact physical dimensions of the parts of the trailer. Some curved geometrical shapes which may have resulted in high aspect ratio, when meshed, were also simplified to more regular shapes. For instance, the curved corner surfaces of the top beam were modelled with right-angled corners. MSC NASTRAN is the solver used for the dynamic analysis of the trailer.

5.1 Finite Element Modelling

Most parts of the semi-trailer were modelled with plate elements. H.J. Beermann [10] recommends plate elements for analysing vehicle structures using the finite element method. A few long slender steel bars, used as stiffeners to some part of the trailer, were modelled using beam elements.

The suspension part of the semi-trailer was modelled so as to simulate the forces transferred to the chassis only. The axles and wheels were completely excluded from the finite element model. Spring elements, dampers and bar elements were used to model the suspension effect.

Welding effect of all welded parts of the semi-trailer was ignored in the finite element model, as it is not the aim of this research to give a detailed part-analysis of the semi-trailer. Taking St Venant's principle into consideration, the strain gauges were bonded at points relatively far from any welded part. This is believed to give results not influenced to an unacceptable degree in the finite element model. Including the welding effect as part of the whole semi-trailer finite element analysis would lead to incorrect estimates, especially on the area of the weld. If the analysis of welding effects or joints is required, H.J. Beermann [10] recommends a separate part analysis. "It is obvious that it is not possible to analyse the stress distribution within the joint areas ... it is necessary to use a separate finite element analysis".

The effects of temperature and rust were also excluded form the finite element analysis. The gauges were temperature compensated, while the effect of temperature change during the test

period is believed not to have had any significant influence compared to the nature of the forcing function, and the properties of steel.

The semi-trailer was taken as moderately in good condition, where the steel is not affected by rusting or manufacturing defects at all. But the material property description or specification of the semi-trailer and the monitored present situation data of the trailer is not available.

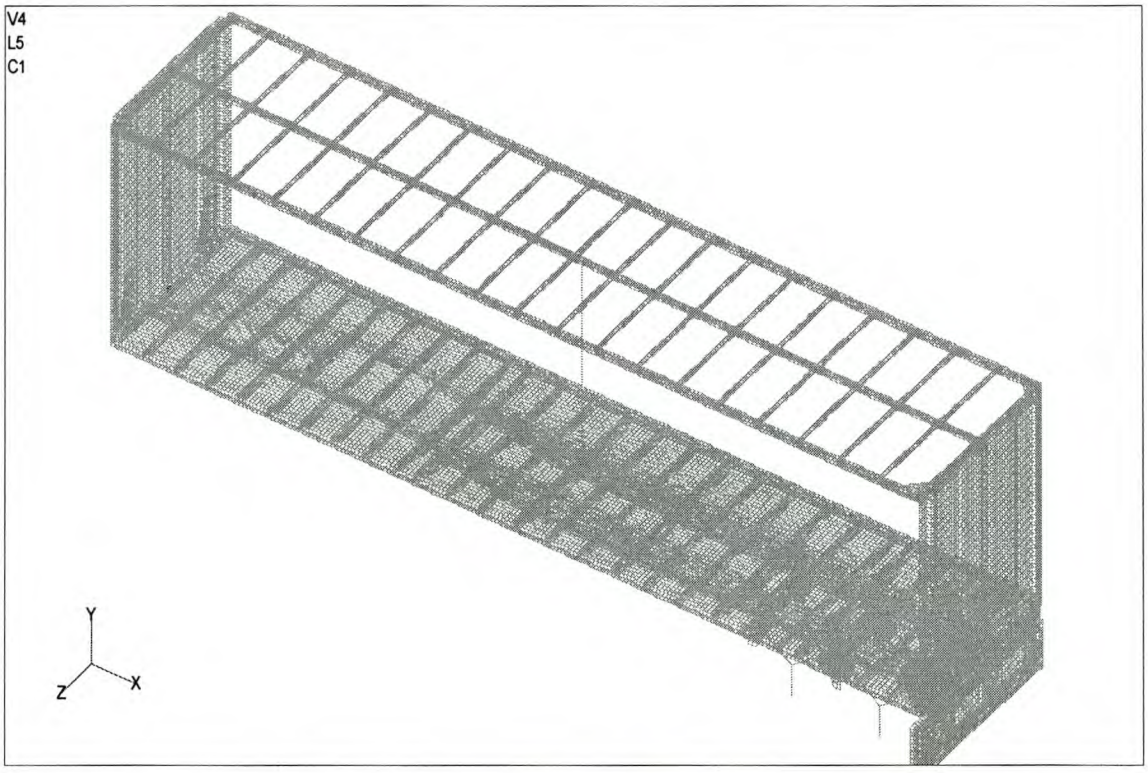

Fig. 5-1 Finite element model of the semi-trailer

5.1.1 Finite Element Meshing

As much as possible, meshing was done to give a regular quadrilateral shape of elements. The only way of achieving this outcome is by using manual meshing. No automatic method would result in a fairly regular geometric shape due to the existence of different crossbars and stiffeners of different size and shape. Surfaces were partitioned manually at their intersection lines and points in order to give regular geometric shapes when meshed separately.

Plate elements were meshed with bilinear quadrilateral elements, CQUAD4, having a size of 50mm. This size was taken to be fine enough, with respect to the size of the structure, and was expected to

give fairly good results. In areas where the geometry was irregular or at points where two or more parts had been welded, the mesh is finer than that mentioned above. At fine-meshed areas or joints, the plate element shape is not necessarily quadrilateral. It was determined by the elements boundary compatibility condition. Mostly, it was made to satisfy the compatibility condition manually. Triangular plate elements, resulting from mesh refinement or inter-elements boundary compatibility requirements, were meshed with three node elements, CTRIA3. The neighbourhood of the strain gauge-bonded locations is also finely meshed. It is not as fine as the size of the strain gauges, to account for the inaccuracy of hand measurement of the strain gauge positions, but fine enough to approximate the average stress value of the gauges in low gradient stress areas.

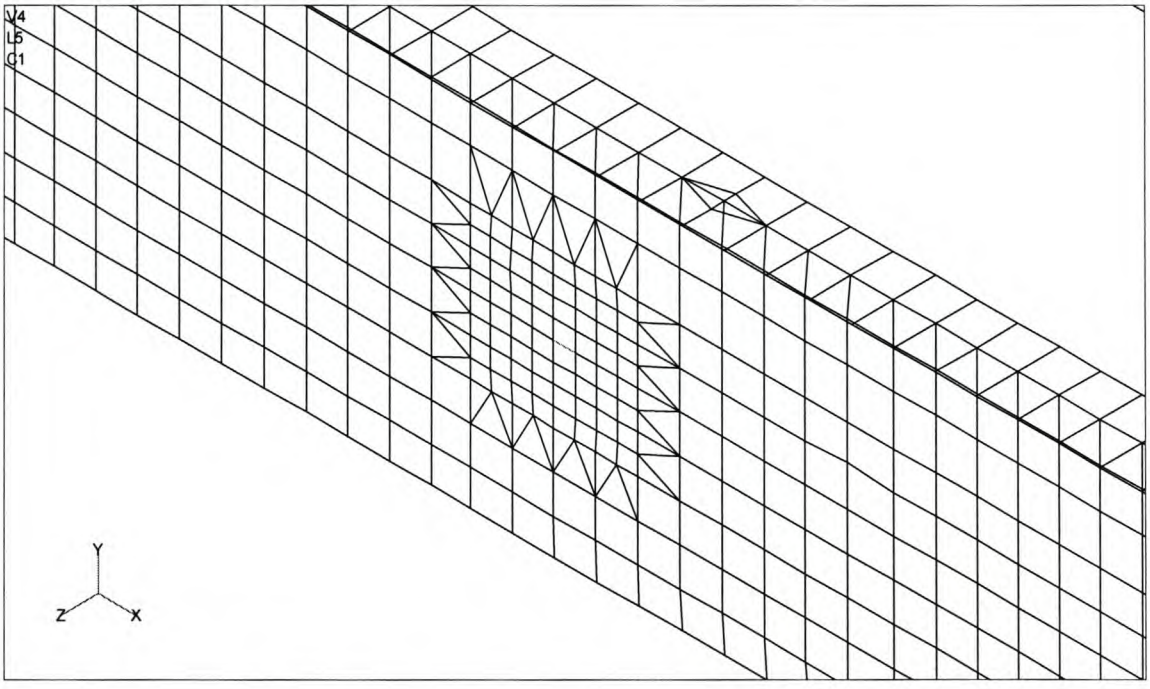

Fig. 5-2 A sample mesh of the gauge bonded areas on the chassis web

Plates welded one on top of the other, like the flanges of the chassis neck of the trailer, were modelled to have the same mid-plane.

Size of beam elements is determined by the size of the plate elements of the parts of the trailer in which the steel bars were used as stiffeners. For bars which were not welded to other parts of the trailer longitudinally, the size of the beam elements was approximately 50mm.

Suspension was modelled with spring, bar and damper elements. The total combination is to simulate the stiffness and damping effect, as well as the degrees of freedom of the semi-trailer at its

suspension. This is for the full contribution of the leaf springs and other accompanying assemblies of the semi-trailer suspension. Displacement of the deck at the spring ends is to a greater extent governed by the leaf spring geometry. That is, the suspension is modelled in a way so that the vertical forces at the wheels are transferred to the chassis in the geometrical fashion of the leaf spring. This was done to simulate the actual motion of the trailer as much as possible, although H.J. Beermann [10] suggests approximation of leaf springs using single vertical springs is sufficient to get quite reasonable results.

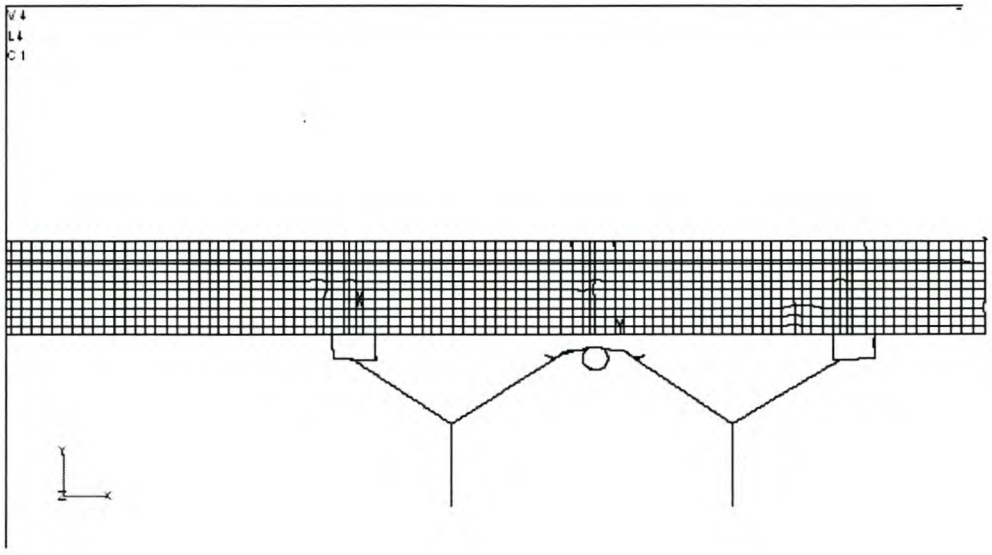

Fig. 5-3 Spring configuration

5.1.2 Approximation of Dynamic Parameters of Suspension

Due to the lack of specifications from the manufacturer of the semi-trailer, almost all the dynamic parameters of the trailer are approximated either from other recommended sources or from the geometrical configuration of the trailer itself. Spring constants of the suspension of the trailer is approximated from the space at the free-end of the leaf springs and the payload of the semi-trailer. There is approximately a 70mm gap between the chassis of the trailer and a welded cross-bar that allows vertical movement of the spring ends. This gap was taken to be the maximum displacement of the chassis at the payload weight of 9 tonnes per axle of the trailer. SABS [10] recommends tanks for road vehicles using petroleum based flammable liquids to withstand an acceleration of 2g in the vertical downward direction. Taking this recommendation as a first trial for the analysis of

the finite element method, the above-mentioned parameters were set to the stiffness of the semi-trailer at a tyre. The final value of the spring constant hade to be determined by tuning the finite element results to curve fit the test values though.

The effective stiffness of the spring geometric configuration at the suspension was tested using a simpler finite element model sample, for its effective spring constants value. A relatively stiff beam element was configured and constrained in the same way as the suspension of the semi-trailer. A vertical force was applied as shown in figure 5.4 and the effective spring constant calculated from the displacement of the intersection of the stiffness assembly.

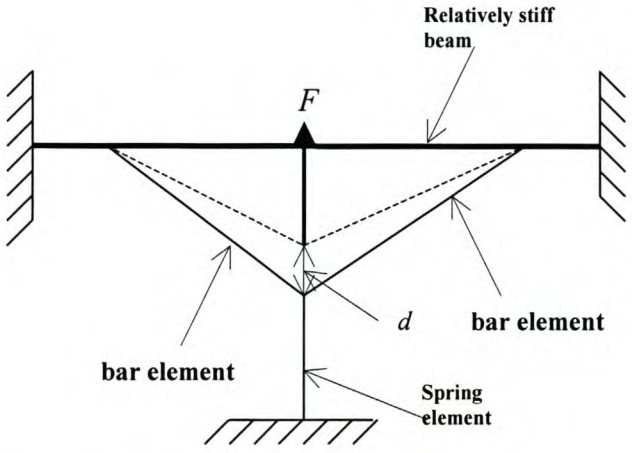

Fig. 5-4 Finite element spring configuration checking

Where F – is applied force

d – vertical displacement

At the interlink-point, stiffness was estimated to balance the rear suspension value, with approximately twice the minimum requirements of SABS [5] recommendation of a semi-trailer definition.

Damping is used to represent the energy dissipation characteristics of a structure. In MSC NASTRAN for Windows a damping matrix can be modelled as a contribution of one or a combination of the following properties:

- damping elements

- overall structural damping coefficient (G) at a frequency of interest (W3) in radians per unit time
- elemental structural damping coefficient (Damping Coefficient in Material Properties) at a frequency of interest (W4) in radians per unit time.

In this particular analysis, since the whole trailer body was made of steel and was relatively stiff, the response signal in the body of the trailer was assumed to attenuate quickly, except at the suspension part. Due to this reason the trailer was assumed to be structurally damped by nature, and damping elements were used to model the damping effect at the suspension only. H.J. Beermann [10] recommends also that viscous damping is satisfactory for vehicle structural analysis.

Similar to the suspension spring constant the viscous damping coefficient of the trailer was estimated by assuming trucks have a damping ratio of 0.37 as a first approximation. The figure is just to start with a high damping ratio, although it is tuned to fit the test data. From equation (2.17c), the damping ratio is

$$\zeta = \frac{c}{c_{cr}} \quad \text{... 5-1}$$

Where c is the damping coefficient of the structure and $c_{cr} = 2m\omega$ is the critical damping coefficient.

Approximating the mass at each tyre from the payload of the semi-trailer the damping coefficient, c, was calculated for equation (5.1).

All the values mentioned above were used as first approximation parameters only, while the final values had to be determined by the experimental curve fit. These first approximation parameters were used also as extreme boundary values for identifying unrealistic parameters.

5.1.3 Constraints and Boundary Conditions

The suspension part and interlink point are constrained in a way to simulate the actual movement of the trailer as much as possible. The non-linear effect of the free-end of the leaf spring and the interlink point is ignored in this finite element analysis. All constraints were made in relation to the nature of movement of the trailer and its actual loading condition during testing. Any transverse translational motion and rotation along the axial direction of the semi-trailer were constrained at all possible forcing function application points, since there is no physical structure that allows any rolling or transverse translation. Other degrees of freedom were constrained according to their necessity. The interlink point was relieved in its pitching and heaving motion, while the suspension was constrained in all rotational motions except swaying.

5.1.4 Load Application

The leaf springs were calibrated to give a force versus mV/V reading. And force deflection curves were calculated from the calibration data as in figure 4.2. Unfortunately a mistake was made in balancing the strain gauge bridges that resulted in fake calibration data. Then another way of estimating the amplitude of the forcing function was sought.

As compensation to the wrongly recorded calibration data, the pallet loading data was used in approximating the amplitudes of the forcing functions, or the weight-deflection characteristics of the leaf spring bridges. Observing the first part of figure 4.4 which is redrawn below, the pallet loaded on one side of the suspension of the trailer did not have much influence on the bridges on the other side.

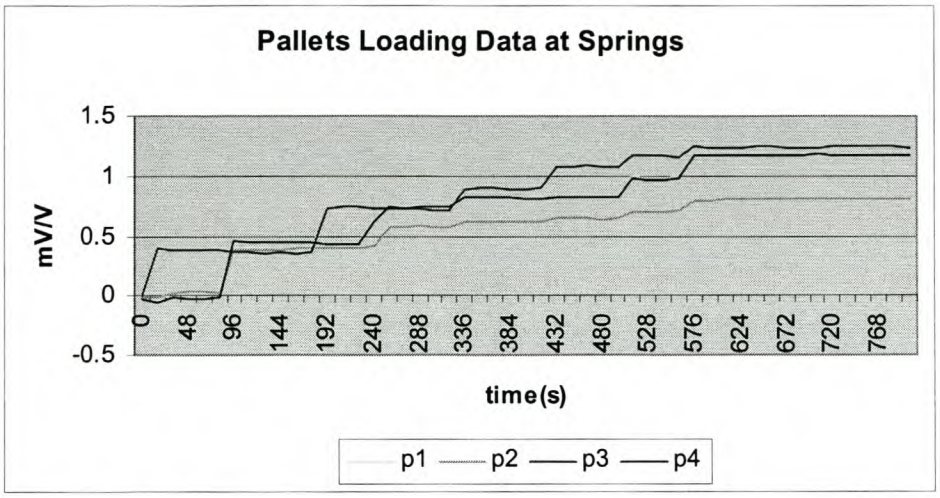

Fig. 5-5 Pallet loading data of axles

Where p1 = rear axle right wheel spring
p2 = rear axle left wheel spring
p3 = front axle right wheel spring
p4 = front axle left wheel spring

Referring to the curves in figure 5.5 in the interval of 0 and 180 seconds, the mass-deflection relation can be calculated taking one side of the springs at a time. Estimating the mass of each pallet to be 1.5 tonnes distributed equally on the two wheels, the calculated mass-deflection values are given below.

No	Leaf Spring	Mass(kg)	Deflection(mV/V)
1	Rear axle right side	750	0.3926
2	Rear axle left side	750	0.3883
3	Front axle right side	750	0.3870
4	Front axle left side	750	0.4477

Table 5-1 Mass-deflection values from pallet loading

Extrapolating the above results to the last part of the curves in figure 5.5, the mass distribution at the leaf springs of the trailer was calculated to be as in table 5.2.

No	Flat Spring	Mass Distribution(kg)
1	Rear axle right side	2040
2	Rear axle left side	1560
3	Front axle right side	2410
4	Front axle left side	1965

Table 5-2 Mass distribution on tyres calculated from pallet loading

The mass distribution at the interlink point was calculated from the difference of the total pallet weights and the flat springs to be 4 025kg.

To verify the above mass distribution, a theoretical calculation was made to find the mass influence at the interlink point from the geometrical positions of the pallets. As can be seen from the pallet loading data of the chassis neck part, figure 5.6, the nearest strain gauges to the interlink point, the curves do not look to make any significant change at least for the first 200 seconds. Comparing the chassis neck pallet loading data, figure 5.6, to the suspension loading data in figure 5.5, it is the time interval just before loading the second rows of pallets from the rear. This shows, the most rear two pallets have no significant contribution on the mass distribution of the interlink point.

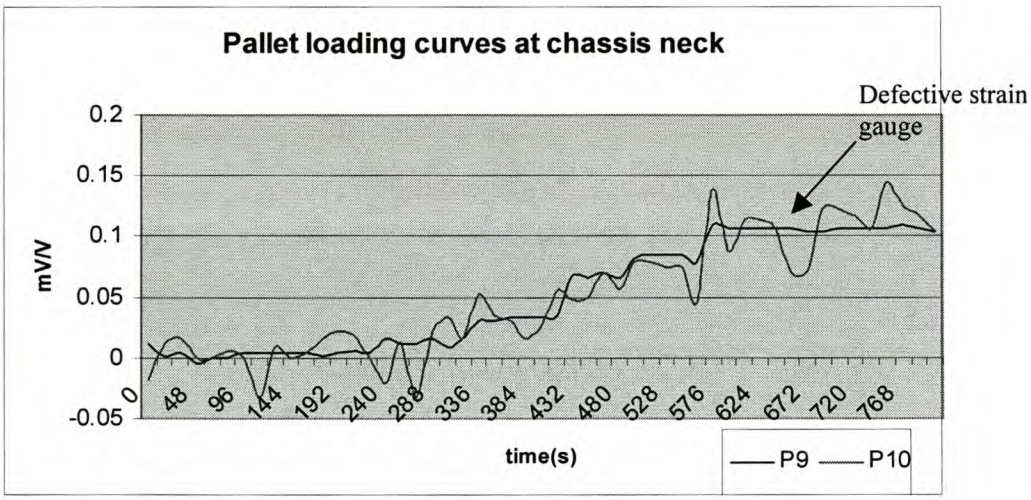

Fig. 5-6 Pallet loading data for the chassis neck strain gauges

Where P9 – right side chassis

P10 – left side chassis

The contribution from the four front pallets was more significant as can be seen from figure 5.6 and is what logically could be expected. There is a contribution from the pallets on top of the first axle to some extent, the interval between 200 and 300 seconds in figure 5.6.

A very crude approximation was used to calculate the fraction of mass at the interlink point from the pallets positions. Each pair of pallets on a lateral row was displaced virtually to the axial centreline of the deck. From their virtual position a reaction-force equilibrium equation was solved to calculate the mass distribution at the interlink point and the centre of the front axle, as shown in figure 5.7. The front four pallets were taken here for easiness of manipulation. The influence of the remaining pallets was to be calculated by extrapolating the results in comparison to figure 5.6.

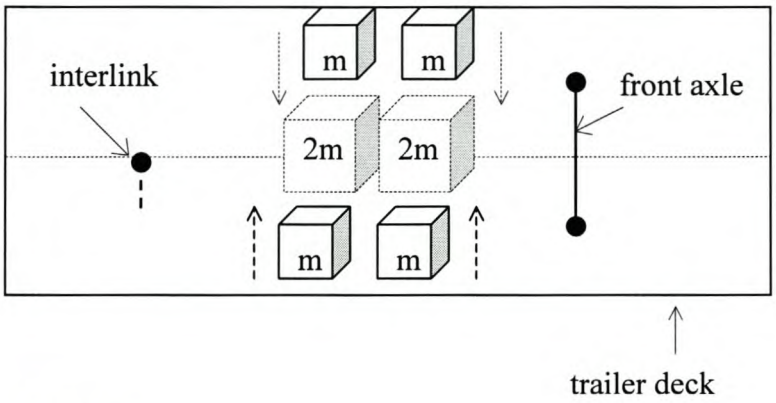

a. Actual pallet positions

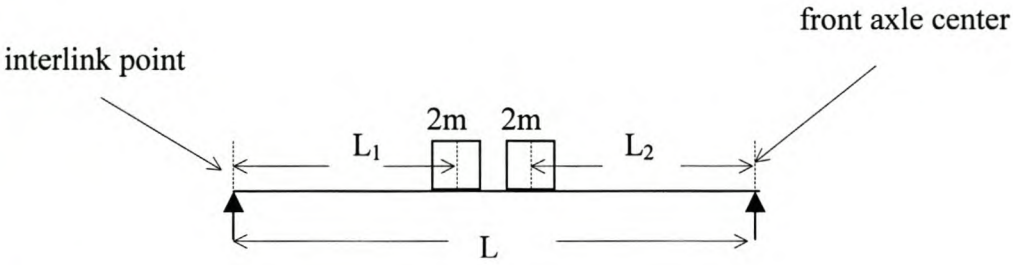

b. Virtual pallet position

Fig. 5-7 Theoretical calculation of mass distribution at the interlink point

Where L is the distance between the interlink point and the front axle, and L_1 & L_2 are distances of each pallet as indicated.

The calculated mass on the interlink using this method adds to about 3.2 tonnes. This value is about 80% of the value of the mass distribution at the interlink point calculated from table 5.2, which is quite reasonable to consider as a first estimate point.

The amplitude of the forcing functions at the suspension part of the semi-trailer was taken to be fixed, by estimating its value from section 4.2.2 and table 5.2. The input functions were normalised with the maximum of the four input points and the normalised experimental data was directly fed to respective input points. The magnitude of the amplitude was calculated from the normalising maximum and the estimated masses in table 5.2.

At the interlink point, a forcing function of the average of the measured data of the front axle was taken. The rear wheels of the tow-truck were assumed to trace almost the same road profile as the front-axle tyres of the semi-trailer. The dynamic impacts on the interlink point were also assumed to be the average of the two wheels due to the interlink point central position. The magnitude is calculated from the mass distribution and the normalising maximum value.

5.2 Finite Element Analysis Used

MSC NASTRAN is the solver used for analysis of the finite element problem. The forcing function of the dynamic analysis used is directly applied from the measured time-varying excitations. Since the input force is a time dependent function, a direct transient response analysis was used as a computing option for the forced dynamic response.

In direct transient response, the structural response is computed by solving a set of coupled equations using direct numerical integration. The fundamental structural response (displacement) was solved at discrete times, typically with a fixed integration time step. A central finite difference representation for the velocity and acceleration is used at discrete times, and the applied

force averaged over three adjacent time steps, similar to the classical Newmark-Beta direct integration method.

Taking the dynamic equation of motion, equation (2-30), for a discrete time $n\Delta t$ where Δt is the unit time interval and the n is the number of integration points

$$[M]\{\ddot{D}\}_n + [C]\{\dot{D}\}_n + \lfloor K \rfloor \{D\} = \{F\}_n \quad \text{... 5-2}$$

the steps used to get the solution at time $\Delta t(n + 1)$ using Newmark-Beta direct integration method is briefly described below. Equation (5.2) can be solved using an unconditionally stable implicit direct integration method known as the average acceleration method. Leaving the mathematical derivation of the method aside, we get the same results of the displacement and velocity expressions if we expand the displacement vector of equation (5.2) in Taylor series.

$$\{D\}_{n+1} = \{D\}_n + \frac{\Delta t}{2}\left(\{\dot{D}\}_n + \{D\}_{n+1}\right) \quad \text{... 5-3}$$

$$\{\dot{D}\}_{n+1} = \{\dot{D}\}_n + \frac{\Delta t}{2}\left(\{\ddot{D}\}_n + \{\ddot{D}\}_{n+1}\right) \quad \text{... 5-4}$$

The Newmark-Beta direct integration method, in its simplest form, is a general form of equations (5.3) and (5.4) given by;

$$\{D\}_{n+1} = \{D\}_n + \Delta t\{\dot{D}\}_n + \frac{\Delta t^2}{2}\left[(1-2\beta)\{\ddot{D}\}_n + 2\beta\{\ddot{D}\}_{n+1}\right] \quad \text{... 5-5}$$

$$\{\dot{D}\}_{n+1} = \{D\}_n + \Delta t\left[(1-\gamma)\{\ddot{D}\}_n + \gamma\{\ddot{D}\}_{n+1}\right] \quad \text{... 5-6}$$

Equation (5.5) and (5.6) are unconditionally stable for values of β and γ given by

$$2\beta \geq \gamma \geq \tfrac{1}{2} \quad \text{... 5-7}$$

Substituting $\frac{1}{2}$ both for β and γ we can find equations (5.5) and (5.6). Solving equation (5.3) and (5.4) for velocity and acceleration

$$\{\dot{D}\}_{n+1} = \frac{2}{\Delta t}(\{D\}_{n+1} - \{D\}_n) - \{\dot{D}\}_n \quad \text{... 5-8}$$

$$\{\ddot{D}\}_{n+1} = \frac{4}{\Delta t^2}(\{D\}_{n+1} - \{D\}_n) - \frac{4}{\Delta t}\{\dot{D}\}_n - \{\ddot{D}\}_n \quad \text{... 5-9}$$

With the values in equations (5.8) and (5.9), equation (5.2) is solved for the set of coupled equations of motion at time $\Delta t(n+1)$ as

$$[K^{eff}]\{D\}_{n+1} = \{F^{eff}\}_{n+1} \quad \text{... 5-10}$$

Where the effective stiffness matrix and the effective load vectors are given by

$$[K^{eff}] = \frac{4}{\Delta t^2}[M] + \frac{2}{\Delta t}[C] + [K] \quad \text{... 5-11}$$

$$\{F^{eff}\}_{n+1} = \{F\}_{n+1} + [M]\left(\frac{4}{\Delta t^2}\{D\}_n + \frac{4}{\Delta t}\{\dot{D}\}_n + \{\ddot{D}\}_n\right) + [C]\left(\frac{2}{\Delta t}\{D\}_n + \{\dot{D}\}_n\right) \quad \text{... 5-12}$$

The displacement at each integration point is iterated from equation (5.10). Other elasticity parameters are solved once the displacement vector is known.

No initial conditions are imposed on the analysis.

The finite element analysis method followed is an intensive trial and error procedure, since most of the dynamic parameters of the trailer are estimated values. Starting from the first approximation of the stiffness of the trailer and damping both at the suspension and interlink points, each parameter is changed at a time. The influence of each changed parameter was recorded so that it helps tuning to the best test-curve-fit. The parameters that gave fairly good curve fitting were tried for all the tests made.

5.3 Finite Element Results

Before tabulating the finite element analysis results, it is worthwhile to make some notes about the nature of the analysis of the finite element model. All the points are mentioned above at their respective topics. They are repeated here for more emphasis and clarification.

Please note that this finite element analysis is made to have a curve fit or correlation of results on average. Making a detailed analysis would be very expensive time wise due to the reasons summarised below. In this case the target point of the finite element method analysis is to get a sound finite element model which generates results that correlate fairly to the test on average, on relatively shorter run time. But it should be noted also that this does not mean to influence the efficiency or the validity of the finite element model. It is just to use as few parameters as possible to get results within an acceptable error margin for this particular test only. The finite element model is modelled to give closer results to the test if more parameters are included that reflect the physical situation of the tests.

All the dynamic trial analyses of the finite element model are carried out on the network, no finite element package that simulates dynamic analysis was available at the workstations. The time needed for an analysis is then dependent, not only on the speed or computing power of the machine to be used but also on the traffic of the network. In this particular model for example, where the computer used for analysis was a Pentium IV, of processor speed 2.4GHz, and RAM 512MB, the time needed to analyse a dynamic input data of 2.5 seconds at a frequency of 320Hz is 3.5 to 4 hours. This time is the time needed for one analysis during that times the network is not busy, normally between 00:00 and 08:00 hours and if the work station is busy analysing the finite element model only. If there are many people using the network at the same time, the time needed to analyse the same data interval increases to 10 hours.

The number of input points also has great impact on the analysis run time. As the number of input points increases the run time increases tremendously. Then a shorter data input interval is taken also as much as possible to get a shorter run time, but not too short so that there wouldn't be significant bias of averaged results. To check the validity of the model for the complete correlation of the finite element and experimental results in a test, finite element analysis is done at different time intervals of the same test. Many short time intervals are preferred to one long-duration input because the run time is not linear to the number of input entries. As mentioned in the above paragraph, where the data input interval is 2.5 seconds at 320Hz, the run time is about 4.5 hours on average. This time is to get strain and stress outputs of 10 elements at output points of every fourth entry of the input. Making the input interval one second in this case for example, does not make the run time to be about one hour as the law of linearity would give, it is rather a few minutes, perhaps 5 to 10.

Table 5.2 shows that there is at least a slight difference in the mass-deflection curves of the four input points of the semi-trailer that may have resulted from the load distribution or stiffness difference. If a detailed analysis is needed to see the influence of stiffness and mass variation at each axle and tyre of the semi-trailer on each strain gauge point, at least 16 analyses are needed, if only two trial points are considered for each parameter. This is quite expensive considering the run time of each analysis. It would have been much better to see the influence of mass variation on each wheel and tune the amplitudes similarly to get a better curve fit, since the exact distribution of the pallets on the trailer deck is not known. But due to the above reason it is preferred to approximate the amplitude on each wheel from table 5.2 and keep it fixed for the total finite element analysis of a test. It is good to note here that the exact mass distribution could have been measured experimentally if not for the calibration error made.

The stiffness and damping may also be different for the two axles at least, as their geometrical configuration is different. But they are approximated to be the same so that there would be a minimum number of trial analysis runs, for the same reason. The complete axle suspension is assumed to have equal spring stiffness and damping coefficients. Then, there are two sets of springs and dampers to be tuned, the axle suspension and the interlink point.

The constraint positions, which result from load distribution, are also other key parameters in getting the actual results in the finite element method. As can be seen from figure 4.3, the trailer was loaded with two groups of pallets at a relatively large separating distance, one group on top of the axles and the other almost in the middle of the trailer deck. It is more logical to model the constraints, at least in a way to resist the loading at the centre of gravity of the two groups of pallets. This would have resulted in more accurate results with fine-tuning of the two weight resisting points. But the cost of it is adding more tuning parameters in two dimensions resulting in more trial analysis numbers. The simpler option, modelling the constraint to resist a single centre of mass was chosen. Without loss of generality, it is good to mention here that the wheel constraints on each axle helps to work as force resisting points to each other. Please note also that the loading at the input points was modelled as nodal forces not nodal acceleration.

Considering the above-mentioned drawbacks, the finite element model analysis is aimed to get results that correlate fairly well to these specific test results on average.

The following tabulated finite element analysis results were obtained at about 650kN/m of spring stiffness per tyre and approximately 18% damping ratio of the semi-trailer. Finite element analysis sample plots are given from each test for the sake of briefing the nature of the curve trace of the finite element results, in addition to the tabulated results.

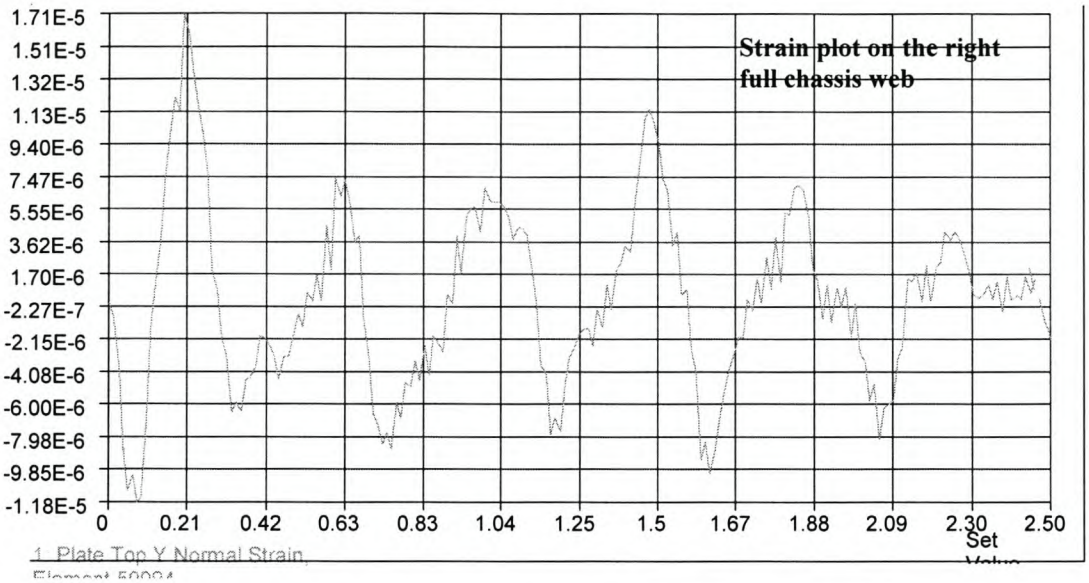

Fig. 5-8 Strain-time plot of finite results for the 70km/h between 0 and 2.5 seconds

Finite element strain standard deviation values

(μm/m, micrometer per meter)

	Full chassis		Tapered part		Neck flange	
Time(s)	**Right**	**Left**	**Right**	**Left**	**Right**	**Left**
0-2.5	4.0854	3.6032	2.1920	2.8537	42.622	44.195
10-12.5	3.0258	2.8791	1.6215	2.3226	33.552	33.911
17-19.5	3.4514	3.1966	2.0301	2.3874	29.582	29.470

Table 5-3 Chassis finite element strain values of semi-trailer

Finite element strain standard deviation values (μm/m)

	Rear Plate		Front Plate	
Time(s)	**Right**	**Left**	**Right**	**Left**
0-2.5	41.000	42.035	13.968	13.768
10-12.5	21.742	21.885	8.5806	8.4188
17-19.5	21.193	20.946	5.0712	5.2679

Table 5-4 Supporting plate finite element strain values of semi-trailer

Finite element stress standard deviation values

(MPa, Mega Pascal)

	Full chassis		Tapered part		Neck flange	
Time(s)	**Right**	**Left**	**Right**	**Left**	**Right**	**Left**
0-2.5	0.817	0.721	0.438	0.571	8.524	8.839
10-12.5	0.605	0.576	0.324	0.464	6.710	6.782
17-19.5	0.690	0.629	0.406	0.478	5.917	5.894

Table 5-5 Chassis finite element stress values of semi-trailer

Finite element stress standard deviation values (MPa)

	Rear Plate		Front Plate	
Time(s)	**Right**	**Left**	**Right**	**Left**
0-2.5	8.2	8.407	2.794	2.754
10-12.5	4.348	4.377	1.716	1.684
17-19.5	4.239	4.189	1.014	1.054

Table 5-6 Semi-trailer supporting plate finite element stress values

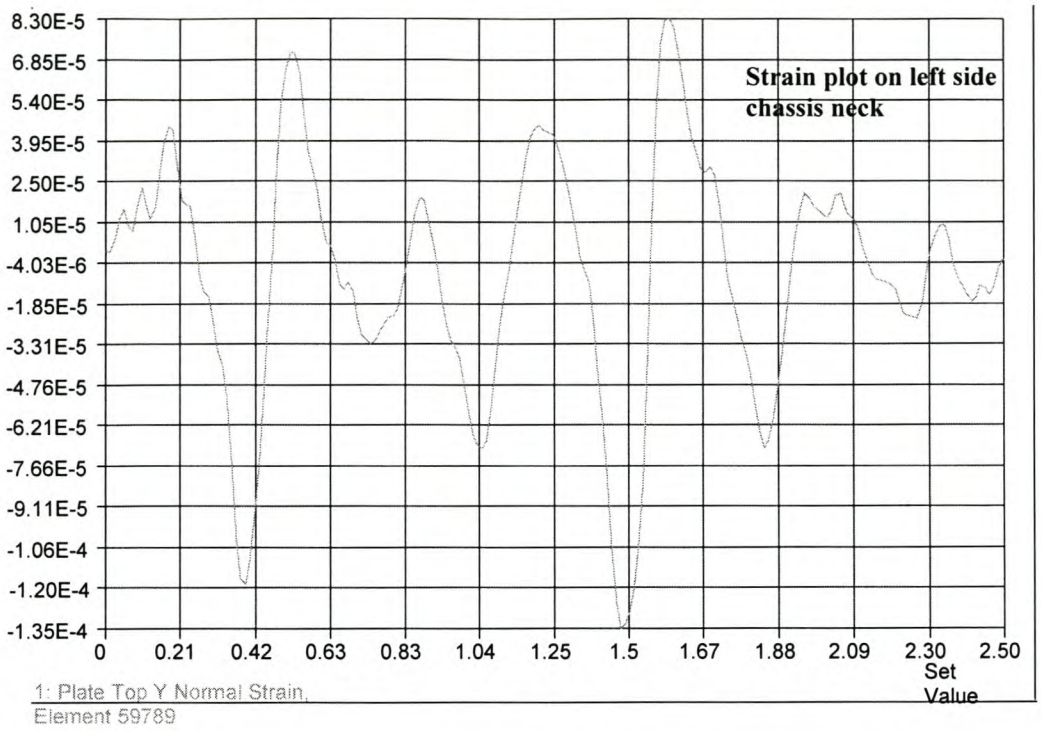

Fig. 5-9 Finite element analysis strain plot of the 50km/h speed between 2 and 4,5 seconds

Finite element strain standard deviation values (µm/m)

	Full chassis		Tapered part		Neck flange	
Time(s)	**Right**	**Left**	**Right**	**Left**	**Right**	**Left**
2 – 4.5	2.916	3.809	2.194	3.377	40.182	37.836
11 – 13.5	1.571	1.508	0.815	1.312	17.695	17.450
13 – 15.5	2.274	2.215	0.969	2.289	28.480	31.464

Table 5-7 Chassis finite element strain values of semi-trailer

Finite element strain standard deviation values (µm/m)

	Rear Plate		Front Plate	
Time(s)	**Right**	**Left**	**Right**	**Left**
2 – 4.5	48.410	48.302	14.882	15.024
11 – 13.5	18.714	18.571	6.4399	6.2810
13 – 15.5	15.227	15.408	4.6443	4.7475

Table 5-8 Supporting plate finite element strain values of semi-trailer

Finite element stress standard deviation values (MPa)

	Full chassis		Tapered part		Neck flange	
Time(s)	**Right**	**Left**	**Right**	**Left**	**Right**	**Left**
2 – 4.5	0.583	0.762	0.439	0.675	8.036	7.567
11–13.5	0.314	0.302	0.163	0.262	3.539	3.490
13–15.5	0.455	0.443	0.197	0.458	4.696	6.293

Table 5-9 Chassis finite element stress values of semi-trailer

Finite element stress standard deviation values (MPa)

	Rear Plate		Front Plate	
Time(s)	**Right**	**Left**	**Right**	**Left**
2 – 4.5	9.682	9.660	2.977	3.005
11 – 13.5	3.743	3.714	1.288	1.256
13 – 15.5	3.045	3.082	9.288	9.495

Table 5-10 Semi-trailer supporting plate finite element stress values

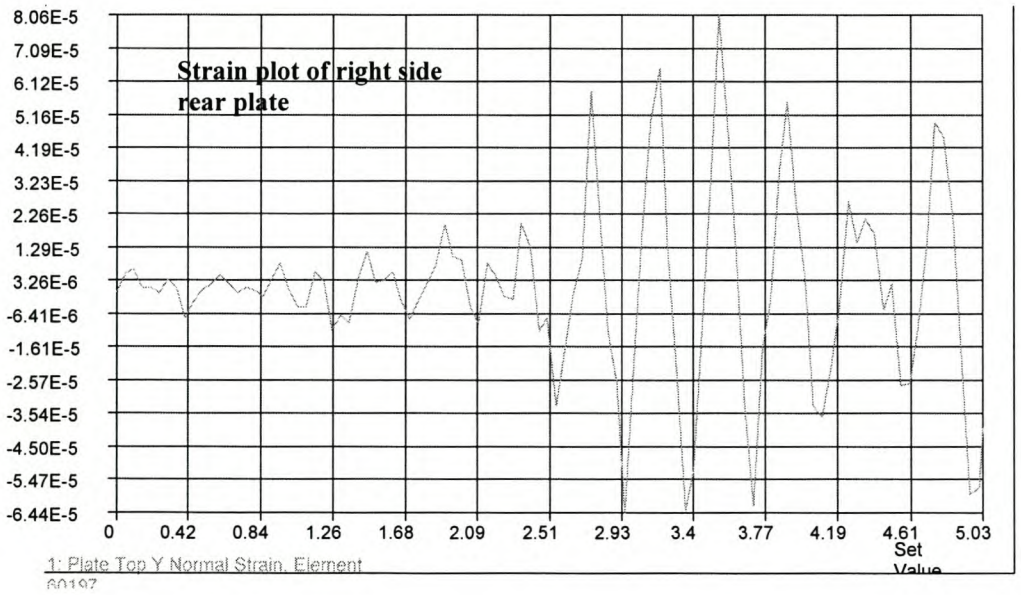

Fig. 5-10 Finite element analysis strain plot of the 40km/h between 0 and 5 seconds

Finite element strain standard deviation values (μm/m)

	Full chassis		Tapered part		Neck flange	
Time(s)	**Right**	**Left**	**Right**	**Left**	**Right**	**Left**
0 - 5	2.0419	2.3689	1.6470	2.2010	28.693	32.804
10 - 15	2.1718	2.3168	1.5349	2.2957	25.785	27.524
15 - 20	2.0066	1.8360	0.94253	1.3984	18.724	20.255

Table 5-11 Chassis finite element strain values of semi-trailer

Finite element strain standard deviation values (μm/m)

	Rear Plate		Front Plate	
Time(s)	**Right**	**Left**	**Right**	**Left**
0 - 5	32.716	32.777	10.080	10.213
10 - 15	35.411	35.061	11.323	11.035
15 - 20	27.337	26.509	9.4395	8.9583

Table 5-12 Supporting plate finite element strain values of semi-trailer

Finite element stress standard deviation values (MPa)

	Full chassis		Tapered part		Neck flange	
Time(s)	**Right**	**Left**	**Right**	**Left**	**Right**	**Left**
0 - 5	0.408	0.474	0.330	0.440	5.739	6.561
10 - 15	0.434	0.463	0.307	0.459	5.147	5.505
15 - 20	0.401	0.367	0.189	0.280	3.745	4.051

Table 5-13 Chassis finite element stress values of semi-trailer

Finite element stress standard deviation values (MPa)

	Rear Plate		Front Plate	
Time(s)	**Right**	**Left**	**Right**	**Left**
0 - 5	6.543	6.556	2.016	2.043
10 - 15	7.082	7.012	2.265	2.207
15 - 20	5.467	5.302	1.888	1.792

Table 5-14 Semi-trailer supporting plate finite element stress values

5.4 Conclusion

The finite element modelling and analysis has been outlined in this chapter. The summarised finite element analysis results are also given here. In the next chapter these finite element results will be compared to the experimental values outlined in chapter 4.

Chapter 6 COMPARISON AND DISCUSSION

Based on the experimentally measured and finite element results, this chapter outlines some of the discrepancies and correlations of the two methods. As mentioned in earlier chapters, the finite element model was modelled with limited resources of the specifications of the semi-trailer. Any parameter not readily available was approximated from similar vehicles or any other means that helped to give a first estimate. The variables were then tuned to curve fit the experimental results. There was not only a lack of specifications for the trailer, there was also some shortage of test input variables. Aspects such as the mass distribution, exact pallet position and the weight-deflection relation of the springs were not known, for example. Even the precise pallet mass was unknown. It is believed to have been between 1.5 to 1.7 tons. To get a sound agreement between the results of the two analyses, estimating all the above-mentioned unknown parameters correctly was needed. Determining the precise constraining condition that would simulate the test-loading condition of the semi-trailer also had its own influence. Therefore, it is natural to expect each of the above assumptions to contribute to the field of error, on top of the deviations that may have risen from the nature of numerical approximation of the finite element method. There is also a great chance of not getting a unique solution, especially at intervals where the natural frequencies of the trailer were closely packed.

Taking all the limitations into consideration, the aim of the finite element analysis was to get averagely correlating curves to these particular test results. Then, the finite element model could be used to modify the design of the trailer by extrapolating the loading case to the full capacity of the trailer with confidence, under controlled conditions.

Broadly speaking, the results of the two systems are in correlation to an acceptable degree. Some results are better in some parts of the semi trailer than others. There are some noticeable phase shifts in almost all the results. There may be many factors that cause this discrepancy or time-lag. As explained in chapter 5 dealing with the finite element modelling, the loading condition was kept constant once it had been estimated from the pallet loading curves. This was done to limit the number of trial-analysis run times. Otherwise it would not have been the closed estimate of the mass distribution. In addition to the mass distribution, it is obvious that the trailer spring stiffness and damping variations have their own contribution to the shift. On the one hand, it is hard to tell at this point the exact reason for the shift as the test was not under fully controlled conditions. On the other hand, it is a bit unwise to kill unnecessary time fine-tuning the parameters to eliminate the

time-shift as it has no significant importance in designing or analysis as to when the maximum occurred.

The comparison was made mostly on visual observation of the curve path and the standard deviation of the two analyses, in this case the average of the absolute value. A more mathematically sound parameter, like the correlation coefficient (equation C-13, in Appendix C) would be better as a comparison criterion. But due to the time-lag of the two signals this would result in a very poor correlation coefficient. The author preferred to stick to the simpler option, as it gives average fitting results. The tabulated comparison at different points of the chassis is given in the following sections.

6.1 Comparison of Results

6.1.1 Full Chassis Results of the Trailer

As can be seen from figure 5.2, this part of the chassis of the trailer is the part which was modelled with relatively regular plate elements. There are no web stiffeners and cross bars, especially in the areas where the strain gauges were bonded. The finite element results on this part are relatively closer to the test results than those in the web of the tapered part. Both the experimental and the test curves trace fairly similar paths with some time shift. A sample comparison of curves on the right side full chassis web for the 70km/h speed test is given in figure 6.1. The test and finite element results from chapters 4 and 5 are summarised here for comparison. All comparison results are absolute averages. The averages of absolute magnitudes are compared for each analysis interval. The strain along the direction of the strain gauge length in the biaxial strain component of the finite element analysis is filtered out for comparison with the uni-axial measured strain. As can be seen from the results in table 6.1 the strain results match to an error of less than 30% for worst scenario for all the comparisons of the tests on the full chassis web, except for one of the intervals of the 40km/h test.

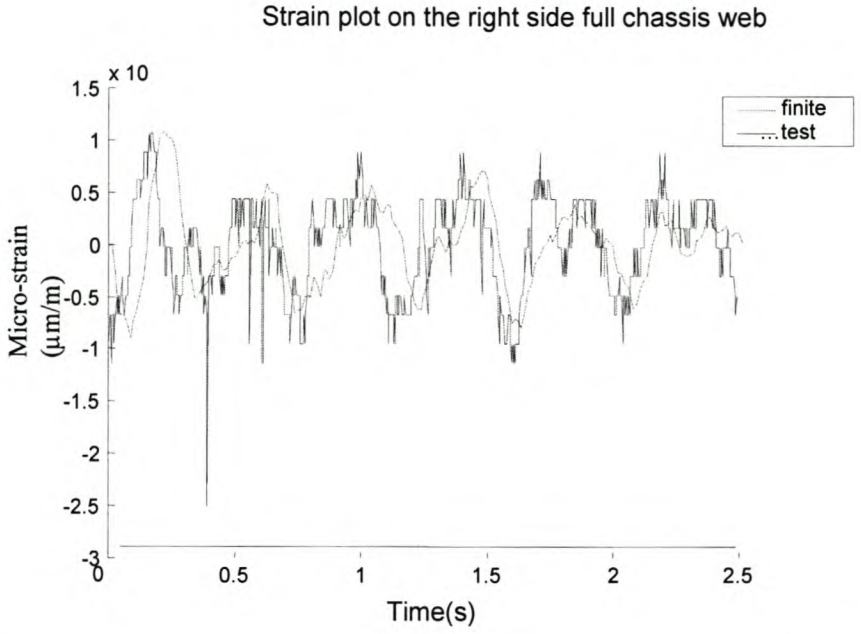

Fig. 6-1 Plot of finite element and test result curves at the right side full chassis web

Semi-trailer speed	Time in seconds	Right side strain results (µm/m)		Deviations (percentage)	Left side strain results(µm/m)		Deviation (percentage)
		Test strain	FEM strain		Test strain	FEM strain	
70km/hr	0 – 2.5	3.78	4.0854	-8.08	3.14	3.6032	-14.8
	10 –12.5	3.02	3.0258	-0.19	3.04	2.8791	5.29
	17 –19.5	2.9	3.4514	-19.0	2.62	3.1966	-22.0
50km/hr	2 - 4.5	3.29537	2.9157	11.5	3.43	3.8088	-11.04
	11 –13.5	1.74064	1.5707	9.76	1.66	1.5075	9.19
	13 –15.5	2.65688	1.9519	26.5	2.44	2.3678	2.96
40km/hr	0 – 5	2.08496	1.7773	14.8	2.08	2.4780	-19.1
	10 – 15	2.10352	2.1718	-3.25	1.95	2.9168	-49.6
	15 – 20	1.61314	2.0066	-24.4	1.71	1.8360	-7.37

Table 6-1 Comparison of strain results at full chassis

The uni-axial stress component in the finite element analysis is calculated from the stress-strain relations of two dimensional objects, equation (1.12a) given below. This result is compared to the stress value calculated from the measured strain using the strain-stress relation equation, $\sigma = E\varepsilon$.

$$\varepsilon_y = \frac{1}{E}(\sigma_y - \upsilon\sigma_x) \quad \text{... 6-1}$$

Semi-trailer speed	Time in seconds	Right side stress results in MPa		Deviations percentage	Left side stress results in MPa		Deviation percentage
		Test stress	FEM stress		Test stress	FEM stress	
70km/hr	0 – 2.5	0.7557	0.817	-8.12	0.628	0.721	-14.7
	10 -12.5	0.603	0.605	-0.26	0.607	0.576	5.18
	17 – 19.5	0.579	0.690	-19.2	0.525	0.629	-20.0
50km/hr	2 - 4.5	0.659	0.583	11.5	0.685	0.762	-11.1
	11 –13.5	0.348	0.314	9.74	0.332	0.302	9.06
	13 – 15.5	0.531	0.390	26.5	0.487	0.474	2.83
40km/hr	0 – 5	0.417	0.355	14.7	0.416	0.496	-19.1
	10 – 15	0.421	0.434	-3.27	0.389	0.583	-49.9E
	15 – 20	0.323	0.401	-24.0	0.341	0.367	-7.53

Table 6-2 Comparison of stress results at full chassis

Similar to the strain the stress compares to an acceptable level. In fact, table 6.2 shows that the deviation of the stress is almost the same as the strain deviations in table 6.1a.

6.1.2 Tapered Chassis Results

The web of the tapered chassis is the part of the chassis of the semi-trailer which is geometrically irregular. To avoid any irregularities of finite element plate elements in meshing, the meshing at this part was made manually to give geometrically regular elements as much as possible. The web stiffeners in this part were closer to the strain gauge points than in others parts of the chassis, although it was the best location in its neighbourhood. From the finite elements result, they seem to be far enough from any stress localisation effect. The strain gauge on the right side of the tapered part seems to be defective, see figure 6.2. The strain gauge at this location was highly amplified by mistake. This may be the reason for the unstable curve trace as shown in the figure. Therefore the results of this part are not discussed in the comparison of results at all.

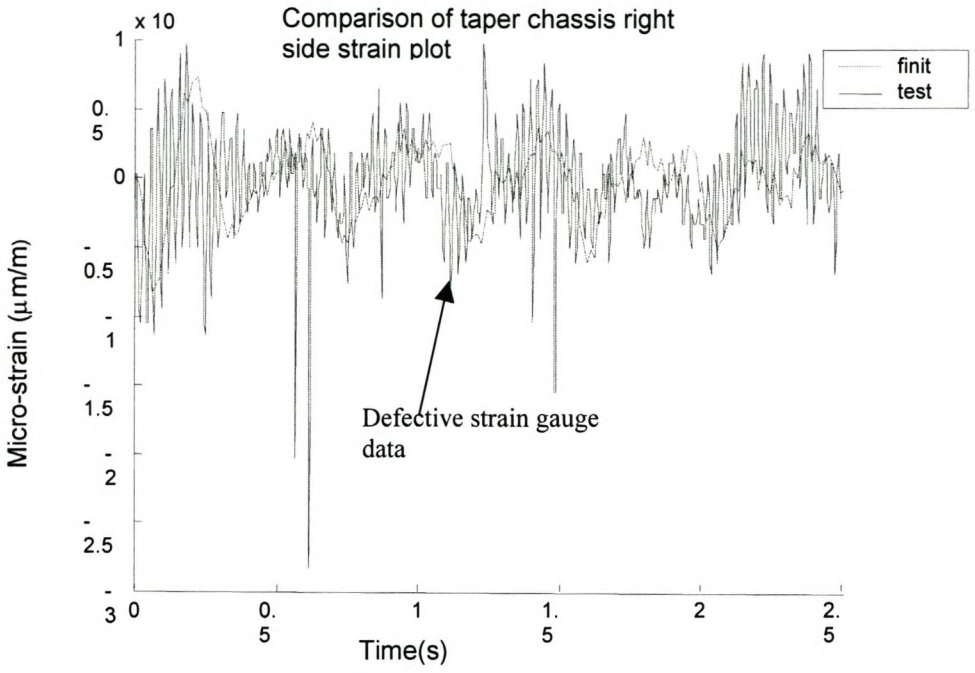

Fig. 6-2 Strain plot on the right side tapered chassis web

As can be seen from figure 6.3 the curve path on the left side of the tapered part is very similar to those of the full chassis web, figure 6.1. The correlation between the finite element and the test results is also not quite far from the correlation of the results on the full chassis web, except in one of the tests where the deviation is as much as 50%.

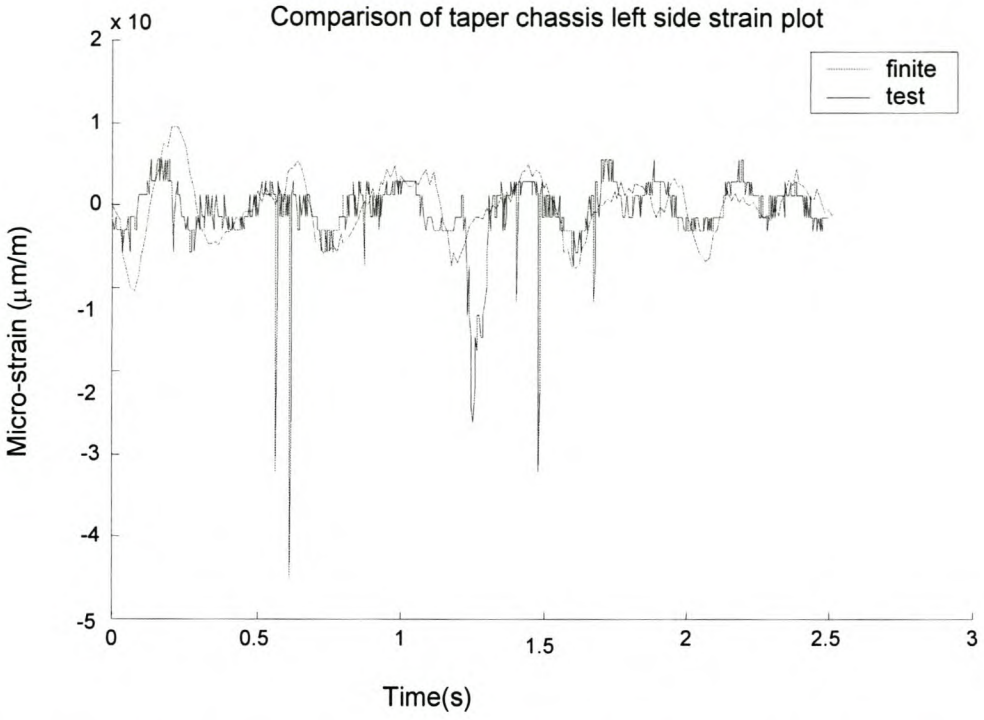

Fig. 6-3 Strain plot at the left side tapered chassis web for the 70km/h test

Semi-trailer speed	Time in seconds	Right side strain results (µm/m)		Deviations	Left side strain results (µm/m)		Deviation
		Test strain	FEM strain		Test strain	FEM strain	
70km/h	0 – 2.5	2.86**	2.1920		2.75	2.8537	-3.77
	10 –12.5	3.36**	1.6215		2.55	2.3226	8.92
	17 –19.5	2.64**	2.0301		1.91	2.3874	-25.0
50km/h	2 - 4.5	2.14**	2.1937		2.76	3.3773	-22.4
	11 –13.5	1.33**	0.81471		1.64	1.3122	20.0
	13 –15.5	1.94**	1.2029		2.04	1.6393	19.6
40km/h	0 – 5	2.56**	1.4523		1.73	1.9080	-10.3
	10 – 15	2.06**	1.5349e		1.64	2.2957	-40.0
	15 – 20	1.97**	0.94253		1.56	1.3984	10.4

Table 6-3 Comparison of strain results at the tapered chassis

Semi-trailer speed	Time in seconds	Right side stress results (MPa)		Deviations percentage	Left side stress results (MPa)		Deviation percentage
		Test stress	FEM stress		Test stress	FEM stress	
70km/h	0 – 2.5	0.572**	0.438		0.551	0.571	-3.68
	10 – 12.5	0.672**	0.324		0.511	0.464	9.04
	17 – 19.5	0.527**	0.406		0.383	0.478	-24.8
50km/h	2 - 4.5	0.427**	0.439		0.552	0.675	-22.4
	11 –13.5	0.266**	0.163		0.328	0.262	19.9
	13 – 15.5	387**	0.241		0.407	0.328	19.5
40km/h	0 – 5	0.512**	0.290		0.346	0.382	-10.2
	10 – 15	0.412**	0.307		0.327	0.459	-40.4
	15 – 20	0.394**	0.188		0.312	0.280	10.3

Table 6-4 Comparison of stress results at the tapered chassis

6.1.3 Chassis Flange Results

The results on the chassis neck also fit to a percentage of deviation less than 30% in the worst case. The curves trace a similar path for both analyses.

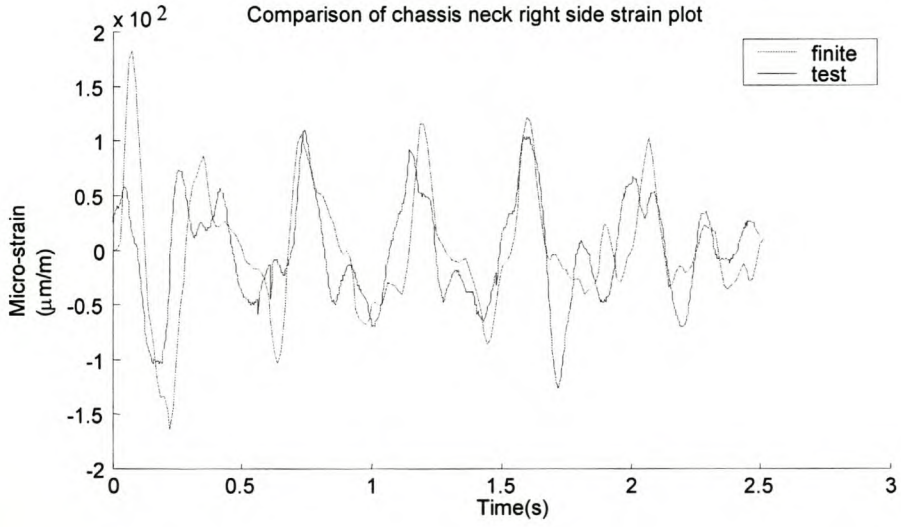

Fig. 6-4 Plot of finite element and test result curves at the right side chassis neck

Semi-trailer speed	Time in seconds	Right side strain results (µm/m)		Deviations percentage	Left side strain results (µm/m)		Deviation percentage
		Test strain	FEM strain		Test strain	FEM strain	
70km/h	0 – 2.5	40.4	42.622	-5.50	41.7*	4.4195	-5.98
	10 – 12.5	32.5	33.552	-3.24	33.4*	33.911	-1.53
	17 – 19.5	26.4	29.582	-12.1	28.4*	29.470	-3.77
50km/h	2 - 4.5	35.2	40.182	-14.2	37.*	37.836	-2.26
	11 – 13.5	17.7	17.695	0.03	20.8*	17.450	16.1
	13 – 15.5	26.7	21.954	17.8	28.7*	20.788	27.6
40km/h	0 – 5	23.3	26.703	-14.6	27.3*	24.824	9.07
	10 – 15	22.1	29.785	-34.8	26.*	27.524	-5.86
	15 – 20	1.6.8	1.8.724	-11.5	20.2*	20.255	0.00

Table 6-5 Comparison of strain results at chassis neck

Semi-trailer speed	Time in seconds	Right side stress results (MPa)		Deviations percentage	Left side stress results (MPa)		Deviation percentage
		Test stress	FEM stress		Test stress	FEM stress	
70km/h	0 – 2.5	8.083	8.524	-5.46	8.337	8.839	-6.02
	10 – 12.5	6.494	6.710	-3.33	6.677	6.782	-1.57
	17 – 19.5	5.278	5.917	-12.1	5.680	5.894	-3.77
50km/h	2 - 4.5	7.043	8.036	-14.1	7.394	7.567	-2.34
	11 -13.5	3.543	3.539	0.12	4.153	3.490	16.0
	13 – 15.5	5.332	4.696	11.9	5.740	6.293	-9.63
40km/h	0 – 5	4.658	5.341	-14.7	5.463	4.965	9.13
	10 – 15	4.415	5.957	-34.9	5.2078	5.505	-5.70
	15 – 20	3.365	3.745	-11.3	4.035	4.051	-0.41

Table 6-6 Comparison of stress results at chassis neck

6.1.4 Results of Supporting Plates

The rear and front supporting plates of the semi-trailer are the parts where it was difficult to get reasonable fitting of curves for the two analyses, the test and the finite element. It can be said the whole effort of the finite element analysis was tuning the variables of the trailer to get a reasonably good fitting of curve on those parts. The sources of discrepancies may be many. As first observation it is good to mention the following finite element modelling defects that can contribute much to the problem.

The ceiling of the semi-trailer was made of rectangular hollow section edge beams and a central longitudinal beam running the full length of the trailer. These beams were strengthened by a rectangular composite plate that covers the total ceiling of the trailer and further strengthened with transverse steel strips or ribs at about 600mm separation distance. The complete composition made the ceiling of the trailer quite rigid. As a first observation, walking on the ceiling of the semi-trailer, to bond strain gauges, and a weight guess of a sample cut from the composite, the composite skin adds much more rigidity to the ceiling than it adds mass. The cut sample was very light, but the ceiling rigid enough to let someone walk on it without noticeable vibration.

In the finite element model the composite plate, the main component for the stiffness of the ceiling, was not modelled. Presumably the finite element model ceiling was much weaker as regards bending and torsion if not tension. As mentioned in the above paragraph, the finite element model was not much lighter than the actual ceiling compared to the decrease in stiffness. Considering these points, it is not that much difficult to see the change of mode shapes and amplitudes that may have resulted in the two analyses. It is just like forcing two different beams, one stiff and the other less stiff, with the same forcing function.

Another noticeable point that may have resulted in a deviation of results of the test and finite element analyses, was on the strain gauge locations of the rear supporting plate. The strain gauges were bonded in a closed structure. There was no chance to determine the thickness of the plates where the gauges were bonded. The thickness of the plate was an estimated value. There may be some stiffeners inside the closed structure too, since the structure was designed for installing the rear lights and other necessary precaution accessories of the trailer. These limitations are big enough not to compare the two results with confidence. Only sample curves of the two results are given in the figures below for observation of the general curve trace.

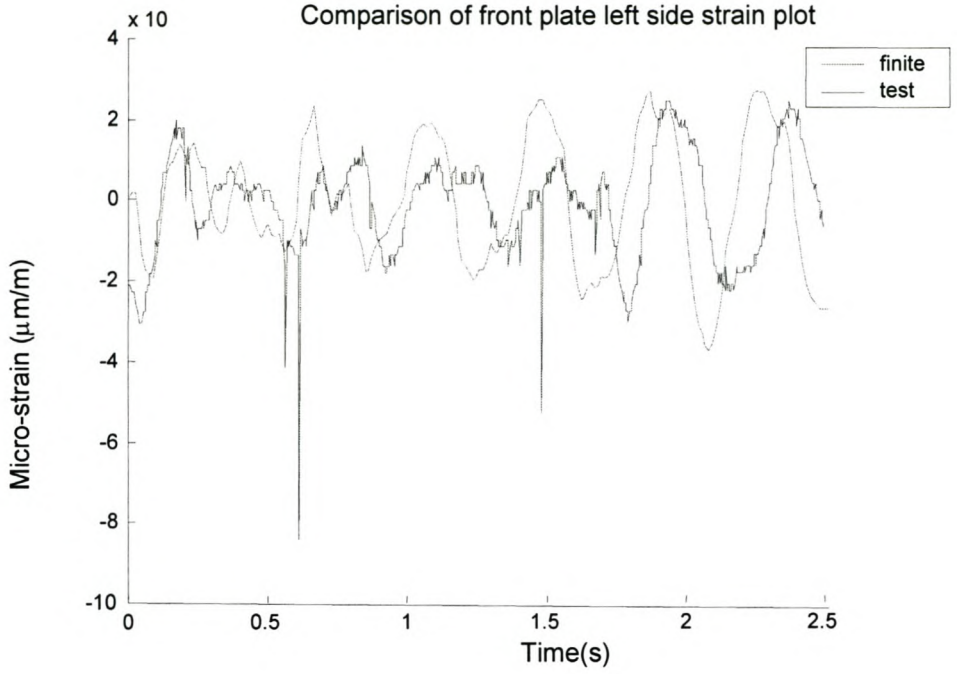

Fig. 6-5 Strain plot at left side front supporting plate for the 70km/h test

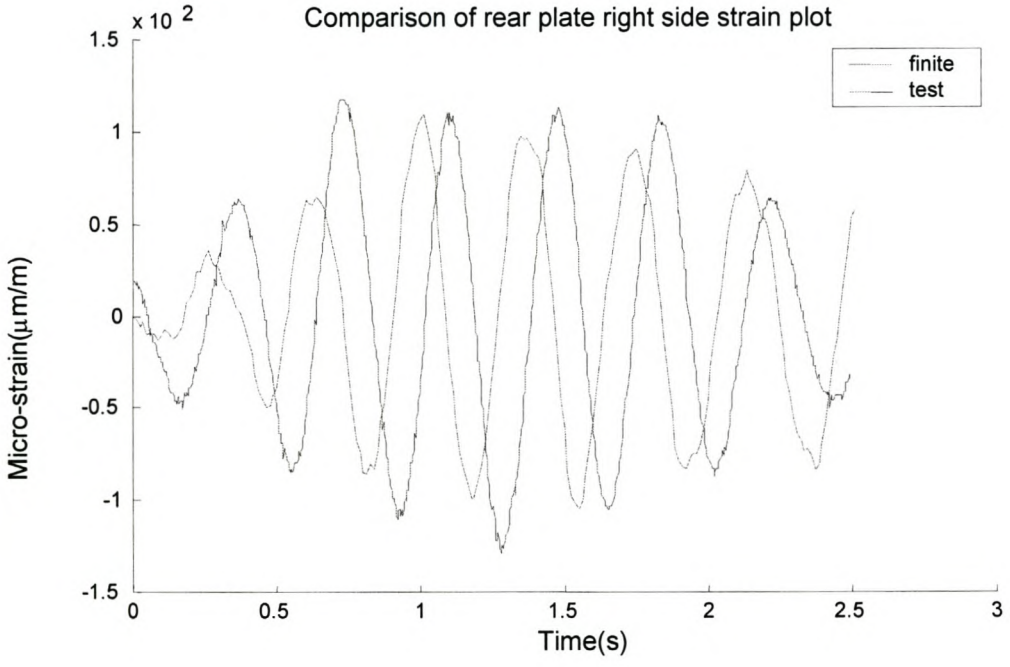

Fig. 6-6 Strain plot at right side rear supporting plate for the 50km/h test

6.2 General Observation

In addition to the discrepancies compared and the phase shifts mentioned above, the following discrepancy points between the finite element and test plot curves can be observed clearly:

At the start of all the curve plots there is a gap between the finite element and test values. The point of result discrepancies differ form time to time and from point to point in all the comparison results or plots, except at the starting time which is a common discrepancy to all. The finite element results start at zero always, while the test value starts at some non-zero value. As explained in the finite element modelling topic, there is no initial condition modelled in the finite element analysis. The nearest strain gauge point from any forcing signal point is nearly 1 metre. This distance will create approximately 3ms time-lag between the two nearest input and output points. 3ms is almost the sampling time interval at 320Hz. Therefore there is a signal delay at the output points at least long enough not to disturb the strain gauges for the first data catching interval of the inputs. The gap between the two values at start depends on the magnitude of the test result at the start of sampling. As can be noticed in figure 5.1, this time delay undermines the finite element results in magnitude at the first part of the comparison interval, especially for low input start signals.

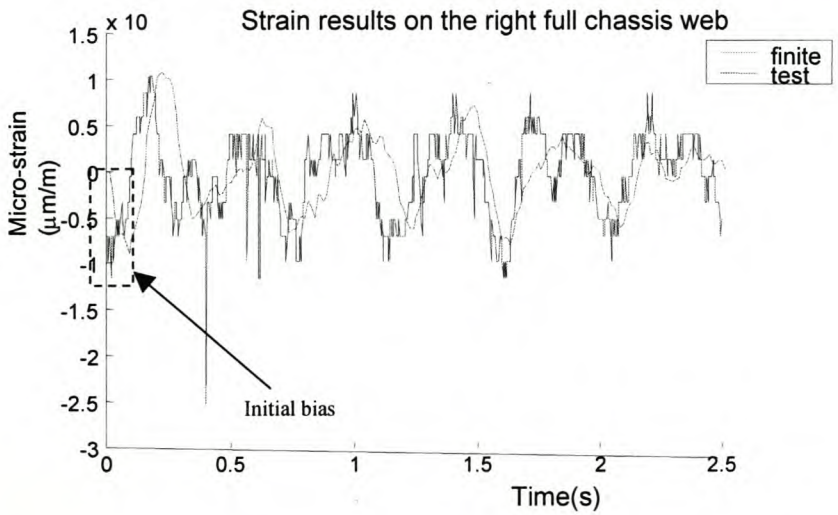

Fig. 6-7 Plot of finite element and test result curves at the right side full chassis web

There are also some exaggerated peaks that do not look to fit at the point where they appear. Similar to the time-lag, this discrepancy can be attributed to different aspects of the finite element model problems, but it is a bit premature to give some specific reason for this.

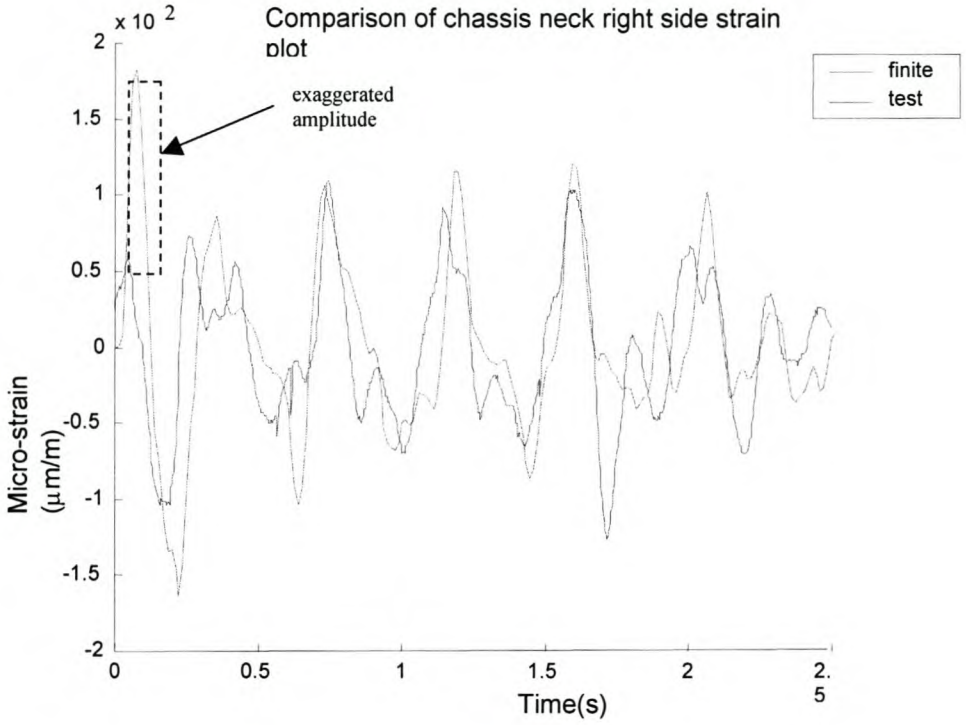

Fig. 6-8 Plot of finite element and test result curves at the right side chassis

The sharp curve tips of the test results do not appear in the finite element analyses results. That is, there are more spikes in the test results than in the finite element. The finite element curves are smoother than the test results. Of course they are the differential and integral form of the problem and it is reasonable to expect the finite element curve to be smoother. The approximation of the integral problem by direct integration method in the finite element method also adds to the smoothness of the curve. In addition to these properties which are part of the essence of the finite element problem, the finite element results are extracted at every fourth point. There is a 75% chance that the sharp tips not to appear on the finite element results. There is a chance that the last point influences the comparison of the two results as well. There is a possibility that the sharp peaks could be noise too, which in essence can be filtered out.

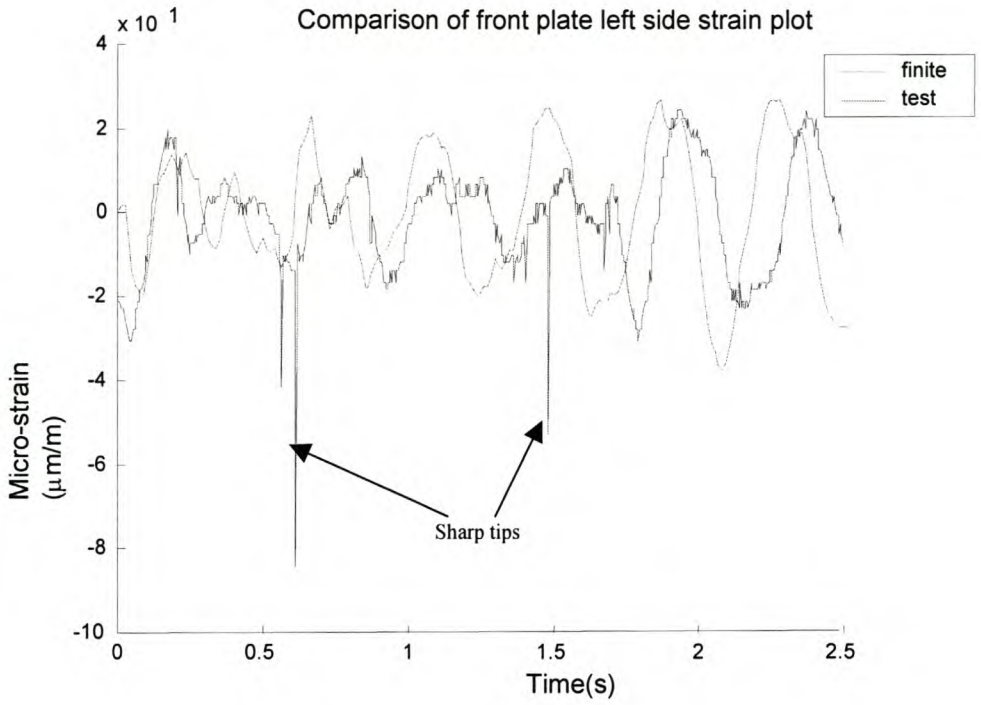

Fig. 6-9 Strain plot at left side front supporting plate for the 70km/h test

Apart from the above lists of discrepancies of the finite element and the test results, all the comparison tables show that the error calculated for the strains and for the stresses are almost equal for all tests, note here that the two quantities are calculated from two different domains. This shows that the finite element model is convergent.

6.3 Extrapolation of Finite Element Results

A static finite element analysis for the recorded extreme loading amplitude of the test is given in this part. It is to give an insight of the stress distribution for extreme loading conditions of the test. It is not a detailed stress analysis, but just for checking the stress fields for the extreme values and the preliminary assessment of the trailer for adverse loading conditions.

From the loading condition of the 70km/h test, figure 4.7, the maximum recorded forcing value is about -2mV/V, only for the dynamic input. This value is approximately 5g. It seems to be a bit exaggerated, but there was quite a strong impact during the test that drove the equipment and personnel a couple of inches, if not feet, high into the air from the trailer deck. And it is not a bad approximation to give a reasonable stress distribution for a similar loading.

A static finite element analysis was made with an input vertical force of 6g, taking the constant acceleration into consideration, for the same mass distribution of the test, and the analysis results are outlined below.

A. Trailer Chassis

The stress over the complete chassis is below the yield point. Generally the stress is high on the bending resisting member of the chassis, with the highest stress distribution around the neck of the chassis. Especially two points on each chassis side are highly stressed. The region where the neck and the taper part of the chassis intersect, and a point almost half way between the end of the taper and the start of the interlink reinforcement plate. Although this is the area where a high stress distribution is naturally expected, the relatively sharp geometry corner on the intersection region of the neck and the taper has its own contribution to the high stress. The lowest stress distributions are the part of the chassis in front of the interlink point and to the rear of the trailer axles, as it should be in accordance to the loading condition of the trailer. Refer to figure 6.10 and figure 6.11 for the stress gradients.

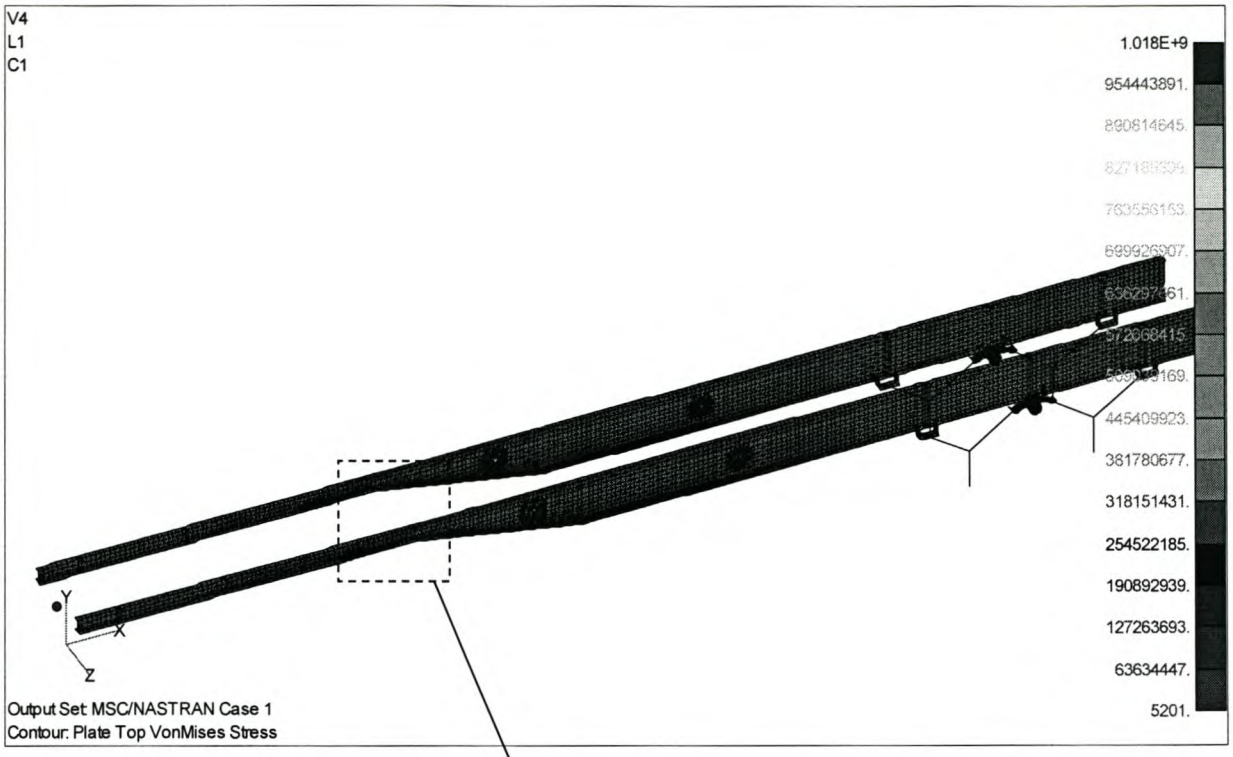

Fig. 6-10 Chassis stress gradient

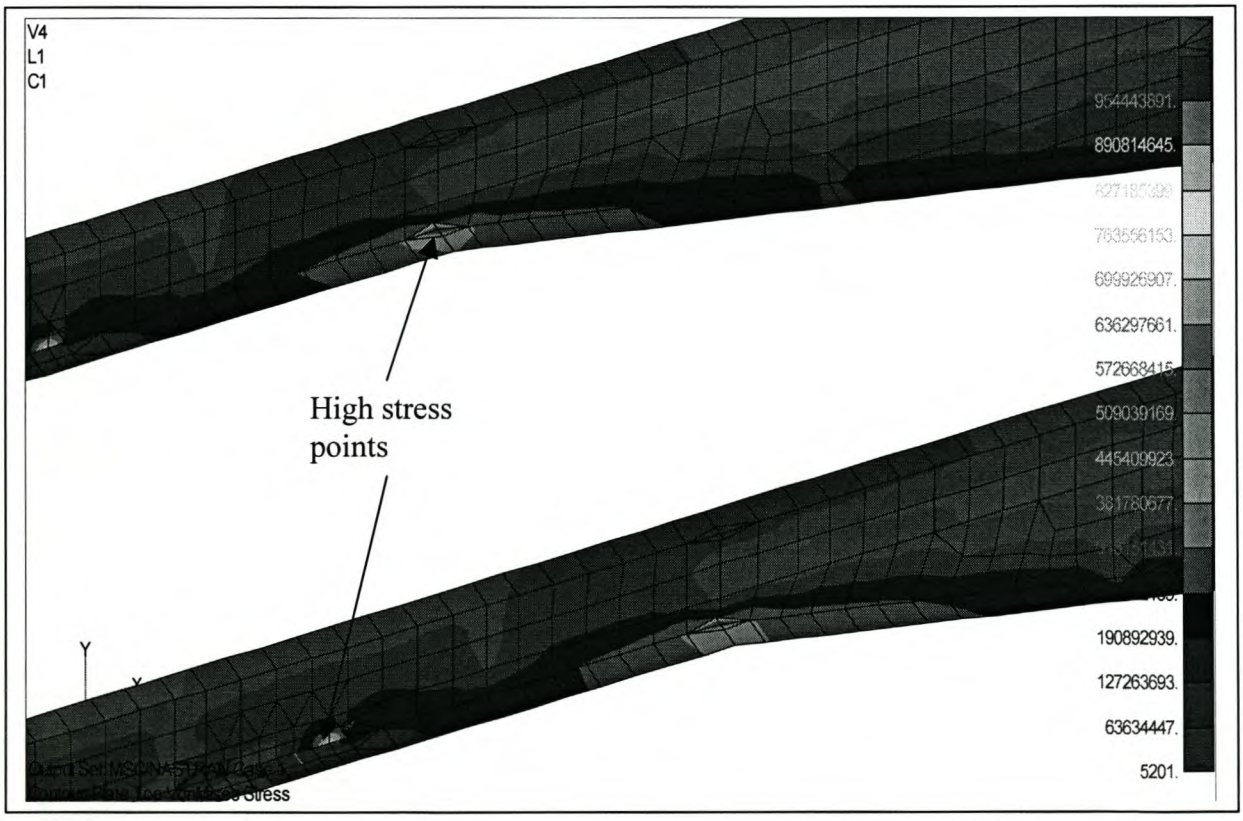

Fig. 6-11 Chassis high stress points

Small localised high stress islands are observed on the chassis part around the axle areas. They are not of concern as to their stress value, but they look to be unreasonable on the areas of low stress gradients. They are just localised stress highs due to the modelling of the brick pallets as mass elements. Otherwise the area is almost the least stressed part second to the front chassis part.

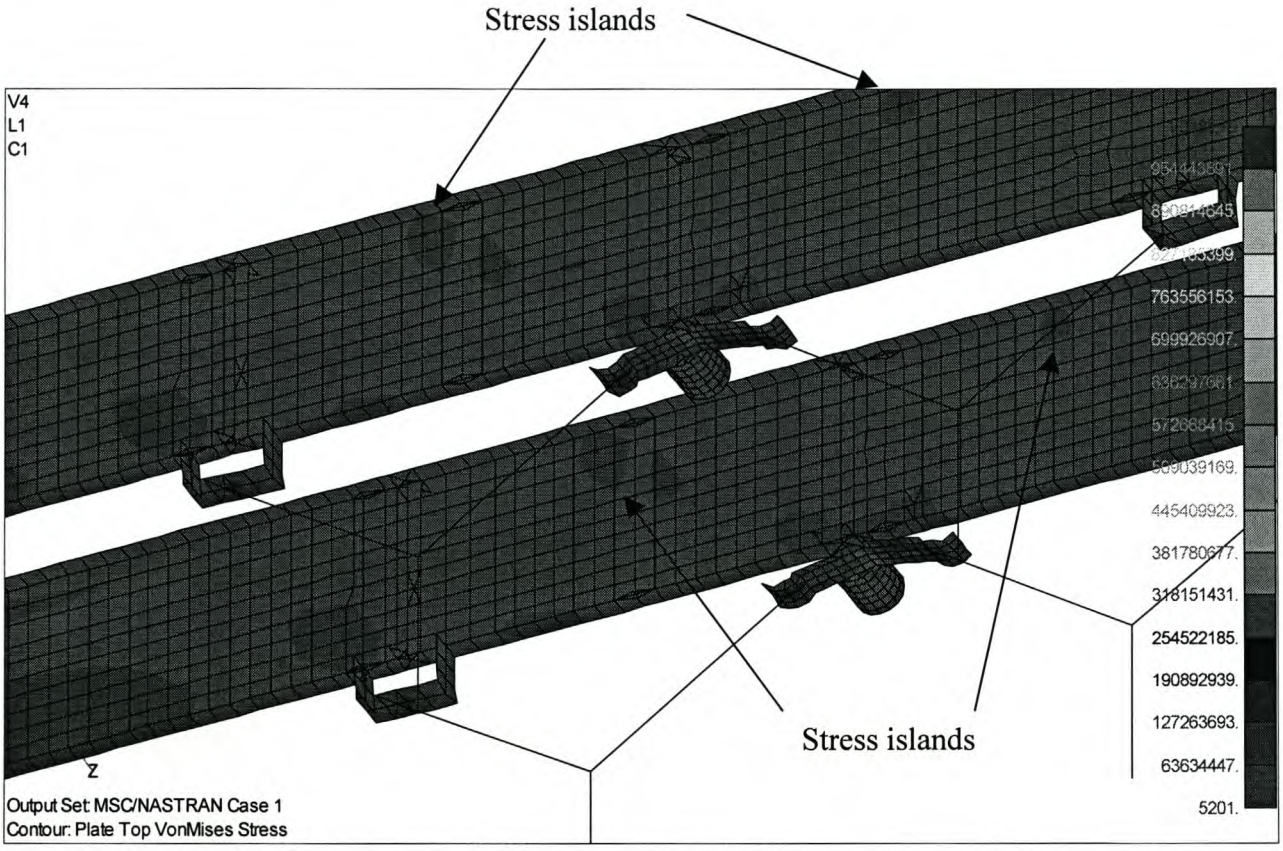

Fig. 6-12 Chassis localised stress points

B. Interlink Reinforcement Plate

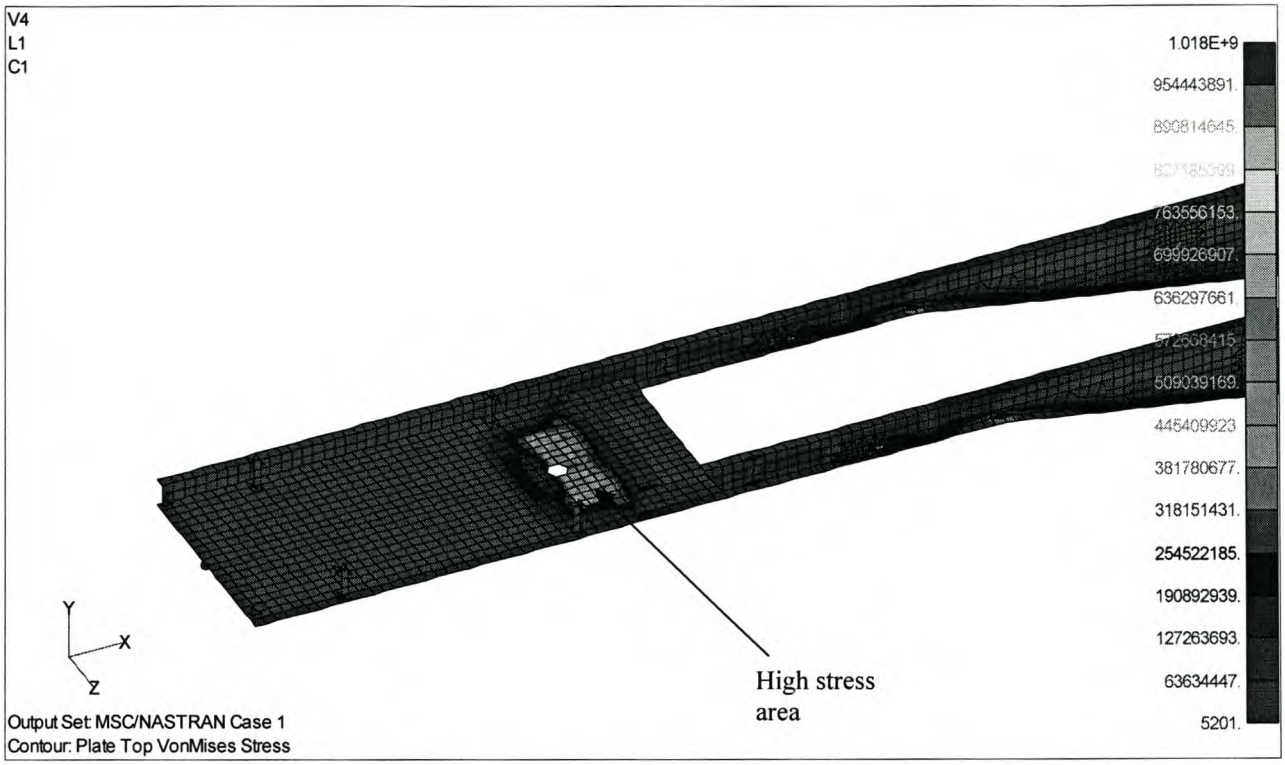

Fig. 6-13 Stress distribution at the interlink point

The chassis neck front part was reinforced with an 8mm plate. In the finite element model, some plate stiffeners were added in addition to the 8mm plate around the interlink point. In the physical trailer this part is supported with a very stiff structure of approximately 0.25 square metre plate of the tow-vehicle in addition to its own reinforced body. Therefore it is obviously weaker in the finite element model, which has less reinforcement and the load is resisted with few nodes. As can be seen in figure 5.6 this part is highly stressed and the stress value is greater than the steel yield point. The structure is not expected to fail as it did not, at least not measurably, during the test because the part is more rigid physically. The model is not modified to simulate the exact nature of the region either. One, it was difficult to measure all the reinforcements on the region, and two, this is aimed to give a general insight of stress distribution of the trailer to the extreme loading condition.

C. Deck Edge Beams

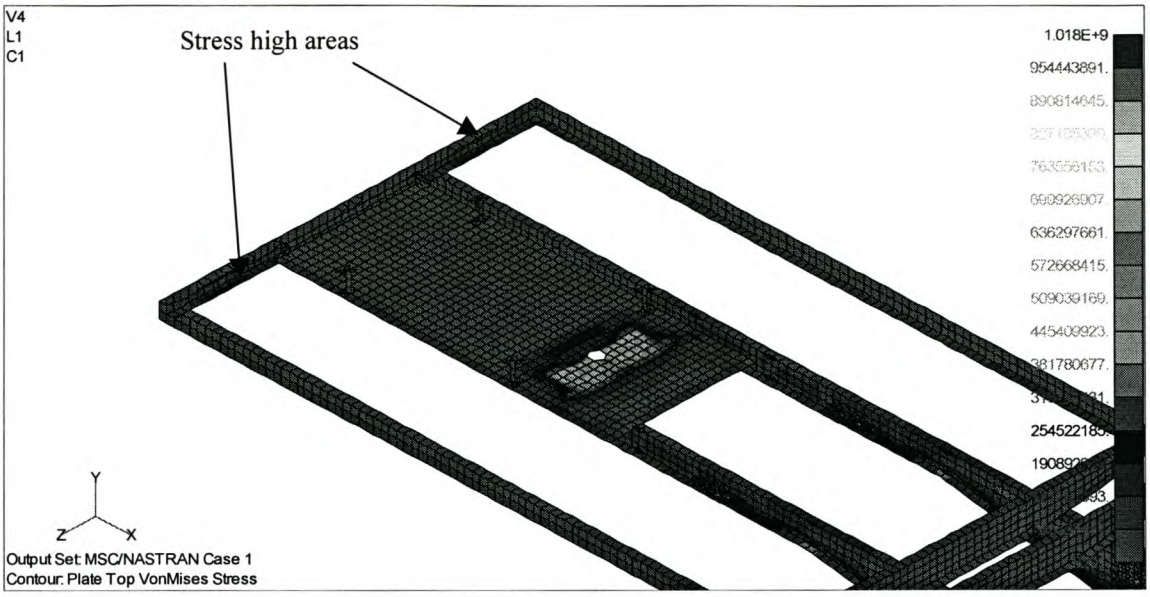

Fig. 6-14 Stress distribution of the deck edge beams

The stresses are relatively low on the deck edge beams with some highs on areas near to the corner of the front and rear part.

D. Deck Cross Bars

All the deck cross bars were almost uniformly stressed with greater stress distributions on the members on the middle part of the semi-trailer. But there is no sign that this can lead to immediate failure on these parts.

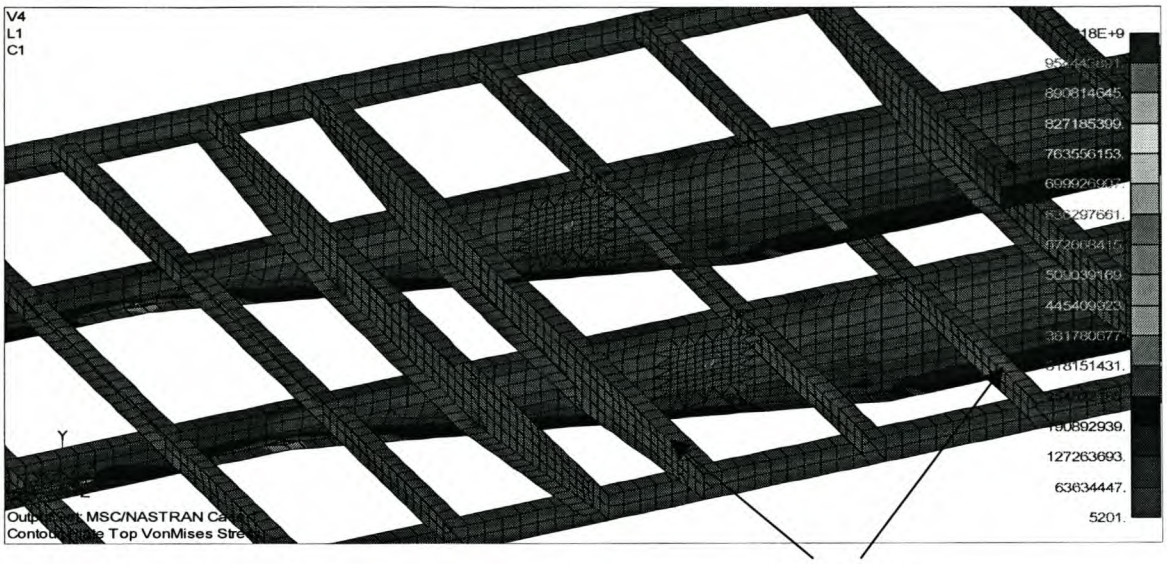

Fig. 6-15 Stress distribution on the deck cross bars

E. Chassis Stiffeners

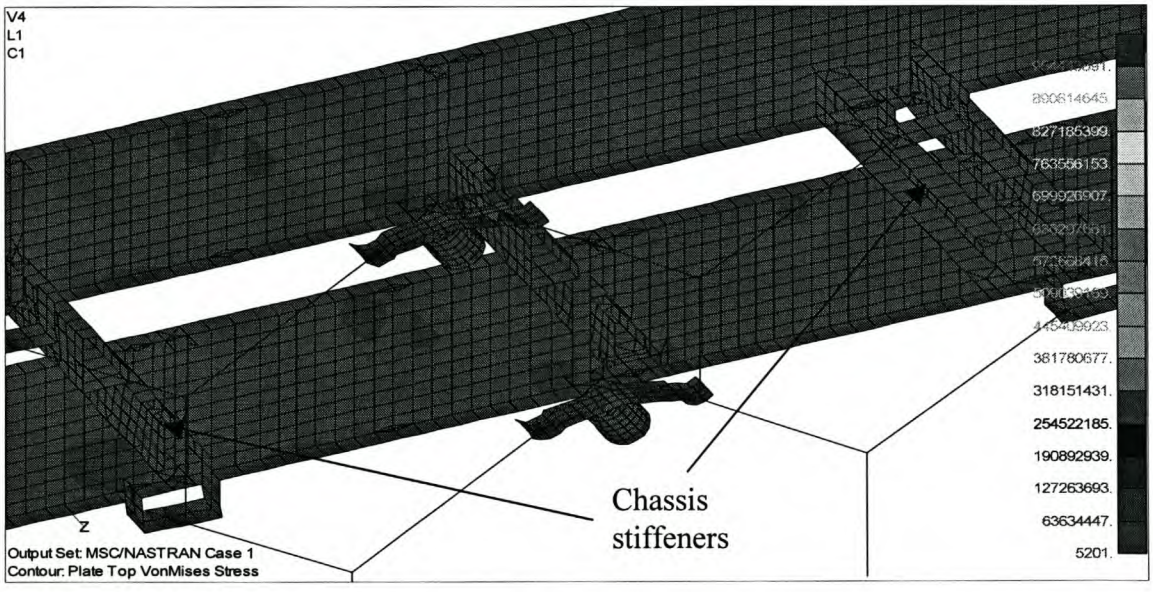

Fig. 6-16 Stress distribution on chassis stiffeners

There is no sign of any highly stressed areas in these members. Actually this area was loaded low in relation to the load that this part should resist. As a result it is almost the least stressed zone.

F. Ceiling Supporting Plates

The relatively high stress areas on the rear and front ceiling supporting plates are the parts near the corners of the plates. The areas are labelled as high in figure 6.17, and some of them zoomed in the accompanying figures to follow.

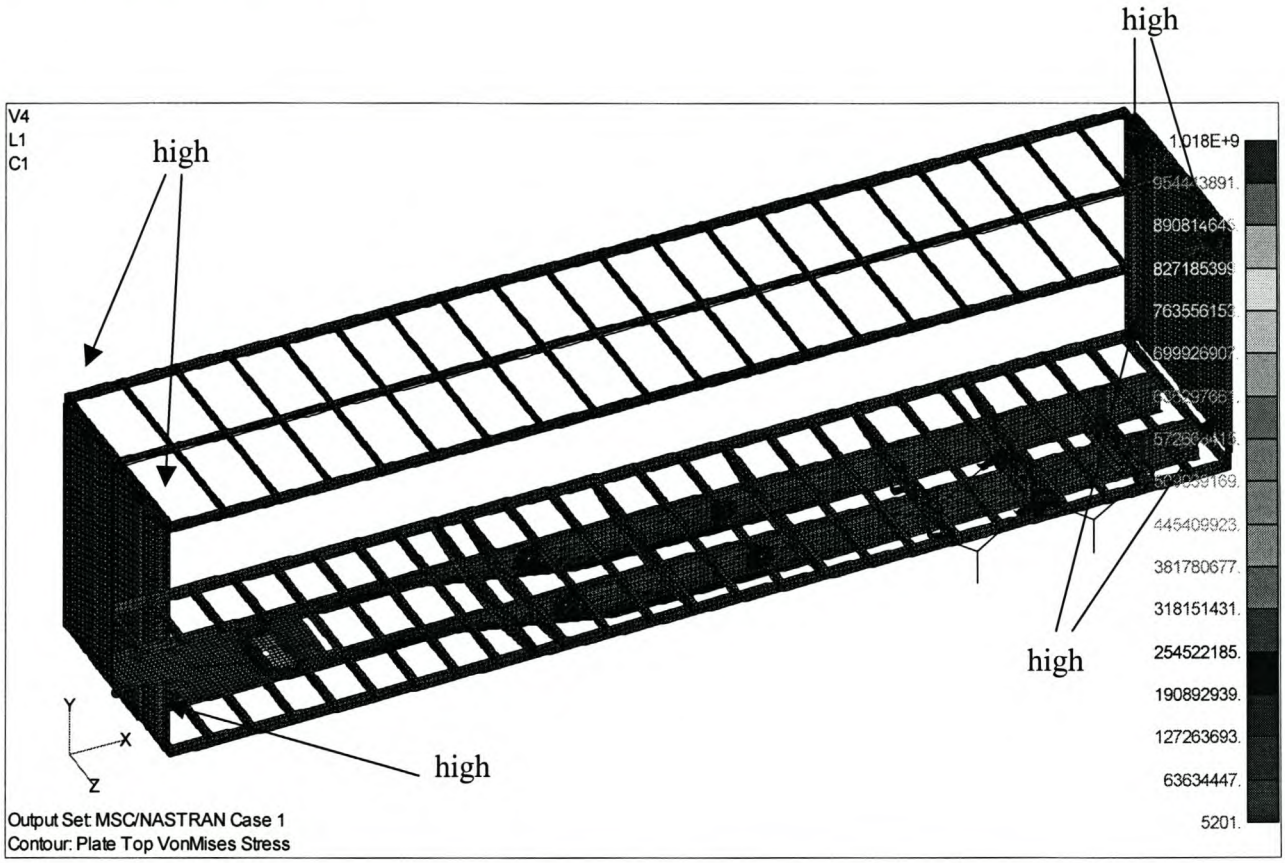

Fig. 6-17 Ceiling supporting plates high stress point areas

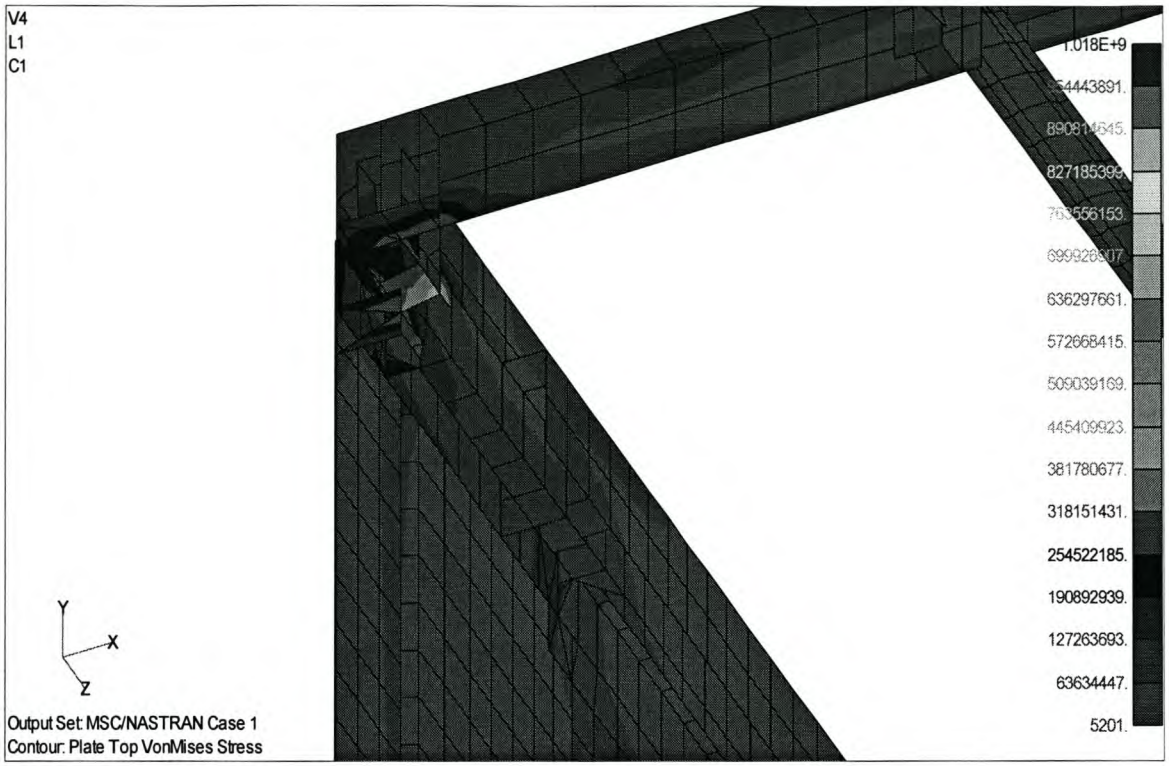

Fig. 6-18 Stress gradient at top front right side corner

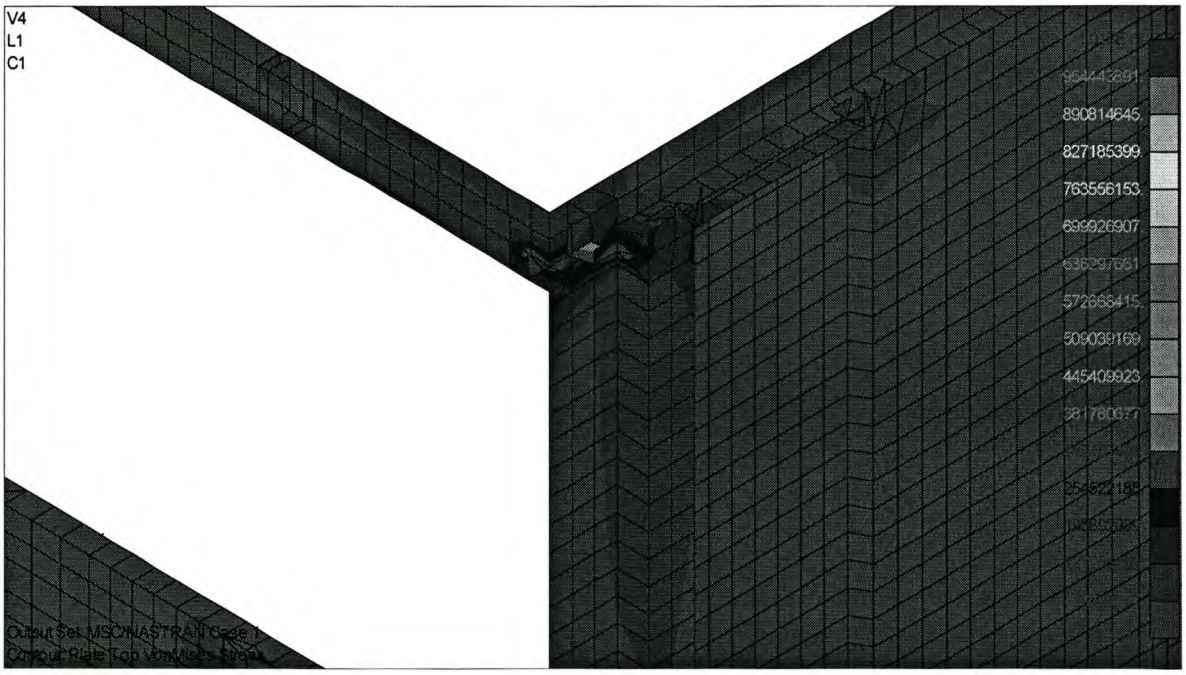

Fig. 6-19 Stress gradient at top rear left side corner

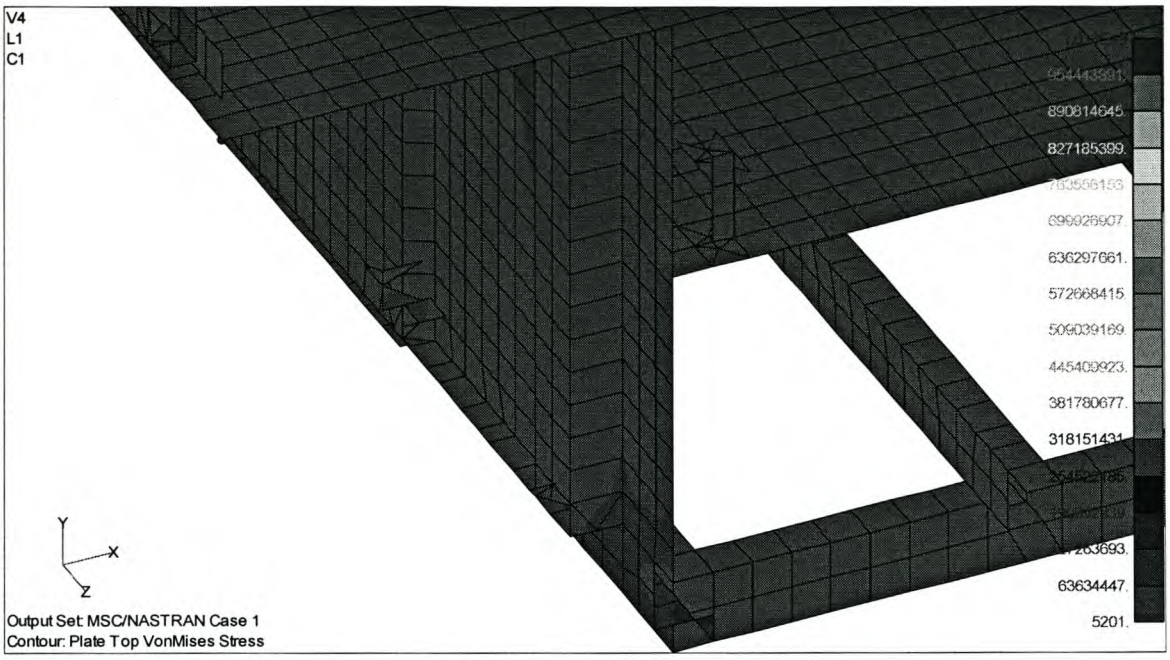

Fig. 6-20 Stress gradient at bottom front left side corner

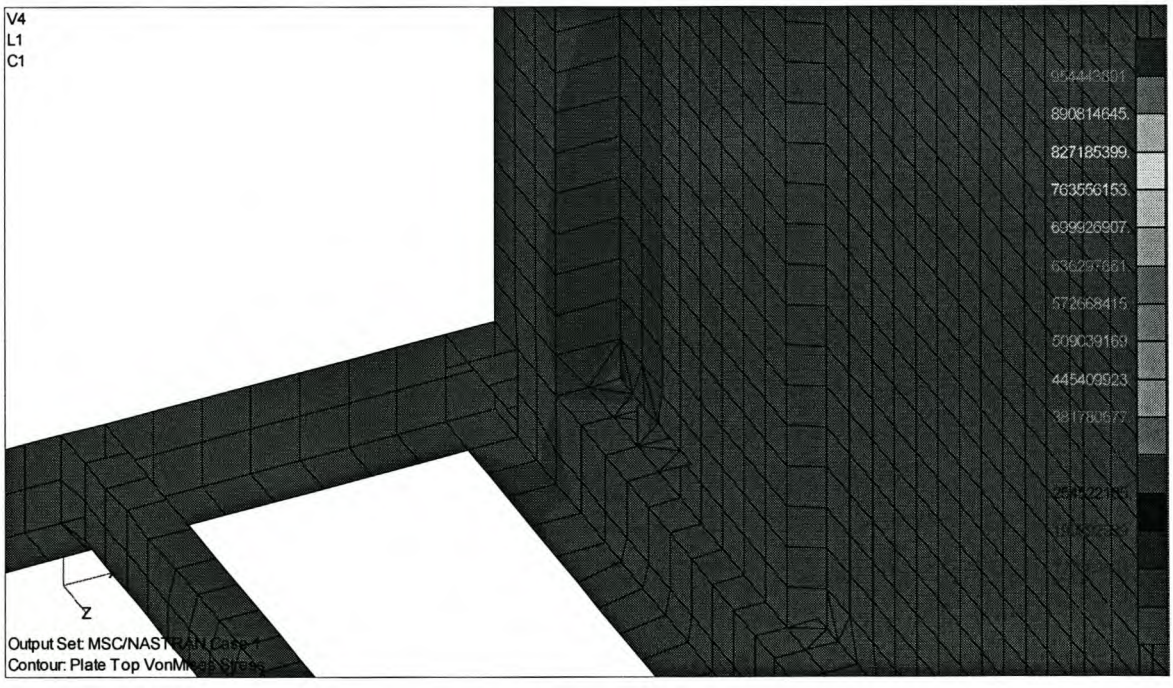

Fig. 6-21 Stress gradient at the bottom rear right side corner

G. Ceiling Beams

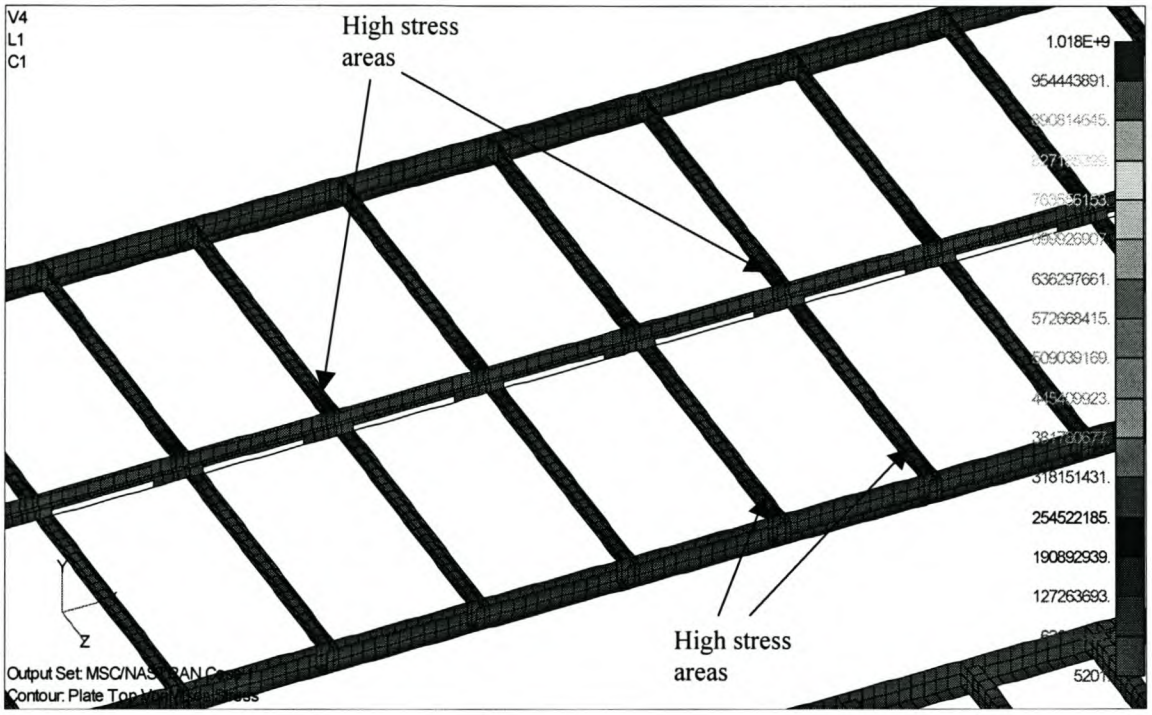

Fig. 6-22 Ceiling beams stress distribution

These members are relatively highly stressed members also, especially in the ceiling middle part. As can be seen in figure 6.11 the side ceiling beams are highly stressed on the top and bottom part of the beam, while the ceiling cross members are stressed towards their two ends.

H. Trailer Deck

At the centre of the trailer deck the ceiling was supported with a steel bar. As can be seen in figure 6.24 at the point where the bar is attached to the trailer, there is a high localised stress that biased the complete stress spectrum. The magnitude of the principal stress at that point is on the order of 1 1 570 MPa. If the failure criterion, equation (2.15), is applied, the structure will fail.

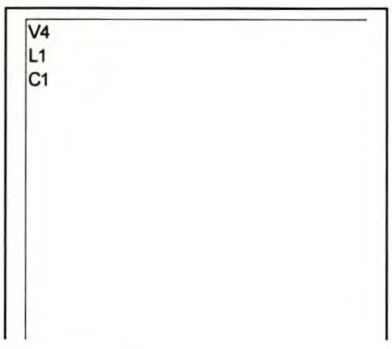

Fig. 6-23 Deck stress gradient

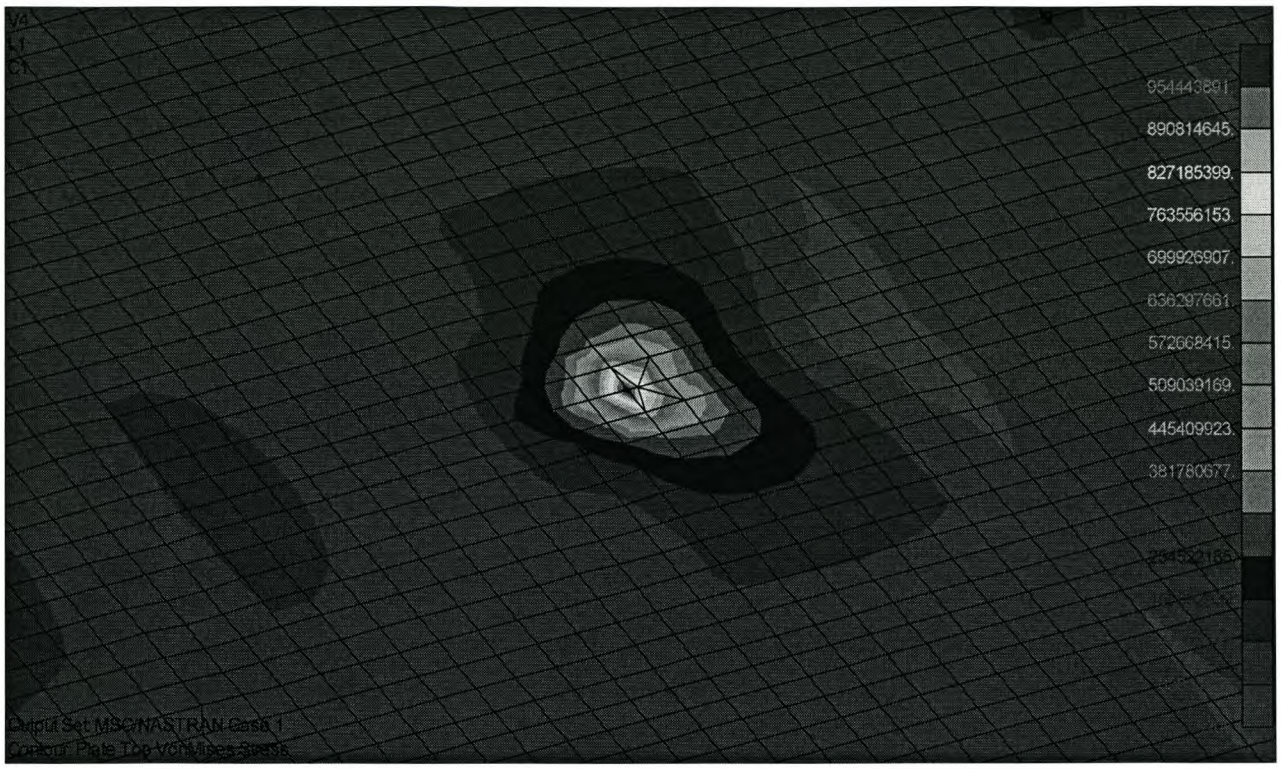

Fig. 6-24 Deck high stress point

It was not checked whether the structure failed physically during the test. The finite element analysis was made long after the test, while the trailer had been shipped off immediately. Apart

form this point there are no other parts that resulted in failure in the finite element model analysis for this high loading condition. There was no big failure that could be noticed immediately in the test either. What is promising of this high stress point is that, firstly it is the point where high stress concentration is to be expected. The bar was welded to a relatively less rigid member of 3mm deck plate at a position where high chassis bending is expected. The attempt of the bar to resist this high bending moment results in high stress concentration. From pre-test visual scanning of the body of the trailer, this point failed several times during the life of the trailer. The bar had been re-welded several times. There are signs that show the bar had been welded at least three times. Due to the frequent welding of the part, the intersection region is more rigid due to the plates added for re-welding purposes. These added structures may have helped the structure not to fail physically during the test like the finite element model.

6.4 Conclusion

The comparison of the results of the two analysis systems shows that they agree in less that 30% deviation on their average absolutes, except for one result which deviates by about 50%. Considering the methods used to approximate the test loading condition, this is not a result that agrees poorly. Following a more systematic way of approximation, like modal analysis or having a better controlled testing atmosphere, would have definitely resulted in closer results of the two systems.

The static finite element analysis made for the extreme recorded loading condition shows also that the noticed high stress areas are areas where we should expect high stress values, at least for the test loading condition. It is quite promising also that the finite element analysis predicted the first failure in an area where failure happened several times in the life of the semi-trailer.

Chapter 7 CONCLUSION AND COMMENTS

Summarising the content of the project, it must be pointed out that the task was executed merely to compare the finite element results with the experimental measured values, to check the validity of the finite element analysis method for further improvement in design or to make further detailed analysis. The test was done on a 12.2m long interlink semi-trailer driven off-road at different speeds.

The method followed to make the two results agree is a trial and error method. Most of the trailer dynamic parameters were extracted from the geometry of the trailer or from similar vehicles if the necessary manufacturing specifications were not available. These parameters were tuned to curve fit the experimental results. Taking the number of parameters to be tuned and the size of the model into consideration, there is no way one could expect a perfect curve fit or 100% accurate results. The parameters that gave the closest curve fit are reported. The comparison tables and curves show that the two analysis results are in agreement at least to the degree that can serve as a first analysis step. Especially taking the method followed for curve fitting, they are in a close agreement. The standard deviation of the two analyses is used as a comparison parameter.

The loading condition is estimated form the pallet loading curves at the beginning of the experiment; and the measured random forcing functions. To decrease the number of tuned parameters, the forcing functions were taken fixed. The amplitude at each forcing point was approximated from figure 4.4 which was verified by comparison to the mass distribution calculated form the geometry of the trailer, and showed about 80% agreement. The dynamic part of the input was directly fed from the normalised measured data at each forcing point.

The tuned trailer dynamic parameters in finite element model comprised are the spring stiffness and the damping. Starting with some estimated values the parameters were tuned to get a closer curve fit of the two results. Another parameter to be tuned was the constraint point. This point was tuned along the longitudinal direction of the trailer to approximate the centre of mass of the test loading condition of the trailer. Then, the finite element model was constrained to resist the vertical force at its centre of mass.

The tabulated results are results obtained at about 650kN/m and a damping ratio of 18%. The standard deviation of the two results shows that the results agree to less than 30% error on average.

These results give confidence for handling the finite element model for further detailed analysis and design modification of the interlink trailer; and predicting the behaviour of similar vehicles to similar forcing functions.

Equipped with the experimental data at hand and the finite element model, the author recommends the following further analyses for future actions.

To get a more profound understanding of the dynamic parameters of the trailer and as a second method of handling the problem, a modal analysis approach is to be followed by modifying equation (2.27) for the accelerance response function. The accelerance response data measured using accelerometers during the test are already at hand. This approach will give more information of the behaviour of the trailer as it is based on sounder principles of vibration.

Another recommendation is to analyse the cornering effects of the trailer. This was completely omitted in this study.

The ceiling composite plate could also be modelled with a similar material or its dynamic characteristics could be approximated. By including the ceiling plate, a detailed analysis on the force transferred onto the ceiling beams could be made, especially to determine the stress distribution of the relatively high stressed parts, e.g. the areas around the corners of the ceiling supporting plates.

Based on the results found with the above analysis improvements, some design improvements of the semi-trailer or similar vehicles can be predicted that can optimise it in terms of mass or other design factors. It is even possible to predict the life of the semi-trailer in places with adverse road infrastructure, for instance, most third world countries, although the prediction may be a bit biased to extreme situations.

Appendix A ELECTRICAL RESISTANCE STRAIN GAUGES

A-1 Introduction

Electrical resistance strain gauges are electrical conductors used to measure strain in materials. There are different types of strain gauges available commercially. They differ in their form and the purpose for which they have been constructed. Since this is a very brief explanation of the basic concepts of strain gauges related to this thesis, only the metal-foil strain gauges are considered. Although the basics are the same for all strain gauges, the gauge bonding and other treatments in handling the gauges in this report bears reference to the metal-foil strain gauges only, strain gauges fabricated from thin metal foil (150μin), used for stress-analysis work by directly attaching to the specimen using a thin layer of adhesive. They are mostly constructed in a zigzag form.

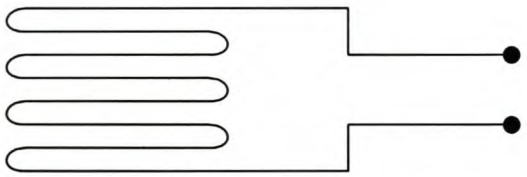

Fig. 1 Sample drawing of metal-foil strain gauge

A-2 Strain Gauge Basics

Lord Kelvin noted that the resistance of a wire increases with increasing strain and decreases with decreasing strain. He also observed that the change in resistance was different in the case of different metals under the influence of the same strain. Based on Lord Kelvin's principle, experiments showed that the ratio of resistance change is directly proportional to the strain for a given metal for a fixed interval, with a constant of proportionality K, known as gauge factor.

$$\frac{\Delta R}{R} = K\varepsilon \quad \text{... -1}$$

Where

ΔR – Change of resistance in the conductor

R – Conductor resistance

K – Gauge factor

ε - Material strain

Equation (A-1) is the basis for strain measuring principles in strain gauges.

The gauge factor is characteristic of a conductor. There are different factors that influence the gauge factor or gauge sensitivity (gauge factor is a combined effect of the axial and transverse sensitivity of the gauge). But, the purpose of this report is to give the basics on how to measure strain using strain gauges, and the method needed in attaching them to the specimen, not a detailed explanation of strain gauges. For detailed strain gauge properties, materials used in gauge installation and treatment, the reader may refer to A.L. Window [12].

The gauge factor ranges from -12 to 4 for most metals [1]. The yielding point for most metals is in mm/m, for example the yielding point for mild steel is 1 200μm/m. Then it is clear from equation (A-1), that most metals reach their yielding point before their resistance change is noticed by most commercial ohm-meters [24], in which an alternative measuring device is needed to sense the low level signals from strain gauges.

A-3 Wheatstone Bridge

The name of the circuit was taken from that of the English scientist, Sir Charles Wheatstone, for his work in developing the bridge to find an unknown resistance with the help of three other known resistances. The bridge is also very useful in measuring small resistance changes.

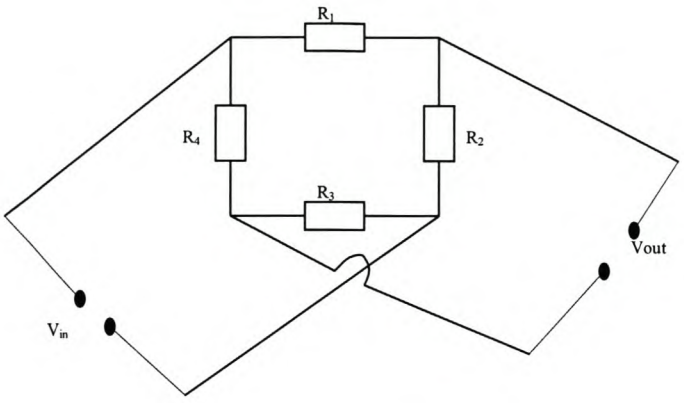

Fig. -2 Wheatstone bridge circuit

Applying the rules of electrical circuits to figure A-2, the following expression is found:

$$\frac{V_{out}}{V_{in}} = \frac{R_1}{R_1 + R_4} - \frac{R_2}{R_2 + R_3} \quad \text{... -2}$$

If equation (A-2) is zero or $\frac{R_1}{R_4} = \frac{R_2}{R_3}$, the bridge is called balanced.

Generally speaking the bridge works from the balanced point. First the zero, or the balanced point is sought by adjustment. If any of the resistors or a combination of the resistors experience any change, say ΔR_1, ΔR_2, ΔR_3 or ΔR_4, the voltage ratio can be calculated by taking Taylor's series of equations (A-2). The quadratic terms and above are ignored for their small contribution.

$$\frac{V_{out}}{V_{in}} = \frac{1}{4}\left[\frac{\Delta R_1}{R_1} - \frac{\Delta R_2}{R_2} + \frac{\Delta R_3}{R_3} - \frac{\Delta R_4}{R_4}\right] \quad \text{... -3}$$

The expression for strain gauges can be found by substituting equation (A-1) with equation (A-3).

$$\frac{V_{out}}{V_{in}} = \frac{K}{4}(\varepsilon_1 - \varepsilon_2 + \varepsilon_3 - \varepsilon_4) \quad \text{... -4}$$

Equation (A-4) is the equation used in strain measurement. The number of active strain gauges can differ on the arms of the bridge. If only one strain gauge is used on any one of the arms of the

bridge, the bridge is known as quarter ($\frac{1}{4}$) bridge, and the rest become dummy gauges. For two and four active gauges the bridge is called half ($\frac{1}{2}$) and full bridges respectively.

A-4 Strain Gauge Bonding

The methods and steps reported here were steps followed in bonding the gauges to the test piece and outlined in the strain gauge handout of the University of Stellenbosch by Dr. E.Terblanche[25].

A-4-1 Preparation of Surface

The first step in bonding strain gauges is cleaning the surface of the specimen from rust, dust and oil.

-Remove rust and dust with coarse (120 mesh) emery paper. In this particular experiment an electric grinder was used because the surface was too rusty to clean by hand using the emery paper only.

-Degrease the surface thoroughly with degreaser. Acetone was used as a degreaser and the surface was thoroughly cleaned using cotton buds.

-Abrade the surface again with finer emery paper (220) taking care not to touch the surface in order to avoid any finger oil contamination.

-Use an acid-etching agent to rid the surface of any static electric effect using gauze swab thoroughly. The swab should be in one direction and the old swab should be used twice at most, one side each time, to avoid re-contamination. Care must always be taken to avoid any skin contamination.

-Mark the position of the gauges with a 4H pencil for aluminium surfaces and ball point pen in the case of steel. Care must be taken when marking the gauge positions not to scratch the surface. The lines should drawn lightly only. Use the acid etching agent to clean the surface using cotton buds again.

-To clean the surface form the effect of the acid etching agent, apply a neutraliser, normally a weak ammoniac solution, using cotton buds rubbed vigorously over the surface. Wipe the surface clean

using gauze swab working in one direction only. The surface is clean and ready for the strain gauges now.

A-4-2 Bonding

-Prepare a clean glass surface. Clean the glass surface both of oil and dust, using acetone. Dry the surface with clean cotton gauze, one directional movement.

-Remove the strain gauge using tweezers (never touch by hand). Place it on the prepared clean surface with the surface to be bonded in contact with the glass.

-Use a length of cellotape to attach the strain gauge to the glass.

-Pull the cellotape starting from one point at a shallow angle to prevent any damage to the strain gauge from picking it up at a sharp angle.

-When the tape is completely free of the glass (obviously the strain gauge should be on the tape), take the tape in both hands and place the strain gauge carefully at the marked point of the prepared surface.

-Once again pull the tape off at a shallow angle from one end only until the strain gauge is off the surface. Then bend the free end over and loosely fix the tape end on the surface (for the sake of keeping the strain gauge away from the surface).

-Smear the surface of the open strain with catalyst lightly and wait a while until the catalyst dries.

-Place a small drop of the quickset type strain glue on the contact surface of the cellotape and the surface of the metal.

-Loosen the bended end of the cellotape and pass the index finger or the thumb firmly over the cellotape starting from the side where the glue was placed. This ensures that no air bubbles are trapped under the strain gauge. Stop when the finger is fully on the strain gauge.

-Maintain the pressure for few minutes depending on the type of glue used. In this particular experiment the pressure was held for 7 to 9 minutes. This is to provide the glue with enough pressure and heat.

-Free one end to the tape; pull it loosely and carefully. Remove the tape from the strain gauge and the metal. The strain gauge should remain firmly fixed to the metal if it has been properly installed.

Appendix B TRANSFORMS

B-1 Laplace Transform

The Laplace transform of an integrable function f(t) is defined by:

$$L[f(t)] = F(s) = \int_0^\infty f(t)e^{-st}dt \quad \text{... B-1}$$

Where $f(t) = 0$, for t < 0, and s is a complex variable.

Equation (B-1) is a transform function where f(t) is transformed from a t space domain into F(s) in s space domain using the Laplace operator L. Some of the properties of L are:

It is linear,

$$L[af(t) + bg(t)] = aL[f(t)] + bL[g(t)] \quad \text{... B-2}$$

The Laplace transform of the derivative of f(t) is

$$L\{f'(t)\} = sL\{f(t)\} - f(0) \quad \text{... B-3}$$

Laplace transform of integral

$$L\{\int_0^t f(\tau)d\tau\} = \frac{L\{f(t)\}}{s} \quad \text{... B-4}$$

Laplace Convolution

$$L\left[\int_0^t f(\tau)g(t-\tau)d\tau\right] = F(s)G(s) \quad \text{... B-5}$$

Where F(s) and G(s) are the Laplace transforms of f(t) and g(t) respectively.

The solution of equation (B-1) can be found in a closed form for many functions. The following example illustrates on calculating the Laplace transform of e^{at}.

$$F(s) = \int_0^\infty e^{at}e^{-st}dt = \lim_{c\to\infty} \frac{e^{-(s-a)t}}{-(s-a)}\Bigg|_0^c = \frac{1}{s-a} \quad \text{... B-6}$$

A list of Laplace transforms of some common functions is given below. The table is not to list all the functions whose Laplace transforms can be solved in a closed form. It is just to point out some common functions that are used as examples in some forcing functions or responses in this report.

For more function transforms or detailed properties of the Laplace transform see Michael D. Greenberg [16].

Laplace transform of some functions with zero initial conditions and t > 0

No	Function, f(t)	Laplace Transform, F(s)
1	$\delta(t_o)$, unit impulse at t_o	1
2	1, unit step	$\frac{1}{s}$
3	e^{-at}	$\frac{1}{s+a}$
4	$\sin \omega t$	$\frac{\omega}{s+\omega^2}$
5	$\cos \omega t$	$\frac{s}{s^2+\omega^2}$
6666	$\frac{1}{\omega_d} e^{-\omega\zeta t} \sin \omega_d t, \zeta < 1, \omega_d = \omega\sqrt{1-\zeta^2}$	$\frac{1}{s^2+2\zeta\omega s+\omega^2)}$
7	$1-\frac{\omega}{\omega_d} e^{-\omega\zeta t} \sin(\omega_d t+\phi), \phi = \cos^{-1}\zeta, \zeta < 1$	$\frac{\omega^2}{s(s^2+2\zeta\omega s+\omega^2)}$

Table B-1 Examples of Laplace transforms

B-2 Fourier Transform

Another common transform method is the frequency transform, which is known as Fourier transform. For an integrable non-periodic function f(t) the Fourier transform is given by:

$$F\{f(t)\} = \hat{f}(\omega) = \int_{-\infty}^{\infty} f(t) e^{-i\omega t} dt \quad \textbf{... B-7}$$

And its Fourier inverse transform is

$$F^{-1}\{\hat{f}(\omega)\} = f(t) = \frac{1}{2\pi}\int_{-\infty}^{\infty}\hat{f}(\omega)e^{-i\omega t}d\omega \quad \textbf{... B-8}$$

Some of the properties of Fourier transform are listed below:

Fourier transform of a derivative

$$F\{f'(t)\} = i\omega F\{f(t) \quad \textbf{... B-9}$$

Fourier transform of an integral

$$F\{f(t) = \int_{-\infty}^{x} g(\zeta)d\zeta\} = \frac{1}{i\omega}F\{g(t)\} \quad \textbf{... B-10}$$

Fourier convolution

$$F\{\int_{-\infty}^{\infty} f(t-\zeta)g(\zeta)d\zeta\} = F\{f(t)\}F\{g(t)\} \quad \textbf{... B-11}$$

Both Fourier transform and its inverse are linear

$$F\{\alpha f(t) + \beta g(t)\} = \alpha F\{f(t)\} + \beta F\{g(t)\} \quad \textbf{... B-12}$$

The Fourier transforms of few functions are given below

N°	Function	Fourier transform
1	$\delta(x-a)$	$e^{-i\omega a}$
2	$\frac{1}{x^2+a^2}$, a > 0	$\frac{\pi}{a}e^{-a\lvert\omega\rvert}$
3	$e^{-a\lvert x\rvert}$, a > 0	$\frac{2a}{\omega^2+a^2}$
4	e^{-x^2}	$\sqrt{\pi}e^{-\frac{\omega^2}{4}}$
5	$f(ax)\cos cx$, (a>0,c real)	$\frac{1}{2a}\left[\hat{f}\left(\frac{\omega-c}{a}\right)+\hat{f}\left(\frac{\omega+c}{a}\right)\right]$
6	$f(ax)\sin cx$,(a>0,c real)	$\frac{1}{2ai}\left[\hat{f}\left(\frac{\omega-c}{a}\right)-\hat{f}\left(\frac{\omega+c}{a}\right)\right]$
7	$f(x+c)+f(x-c)$, c real	$2\hat{f}(\omega)\cos\omega c$

Table B-2 Examples of Fourier Transforms

Appendix C A NOTE OF STATISTICAL CONCEPTS

The nature of the forcing function of the experiment executed for this thesis is of a random nature. It cannot be expressed as definite function of time or frequency. The best approach to such problems is from a statistical point of view. The problem can be approximated to have some probable value in a given time interval. To help handle the problem of this experiment from statistical point of view, some of the basic expressions of statistics are given below.

In their classical definition, probabilistic and statistical concepts are defined in terms of infinitely many sample records, $x_i(t)$, known as ensemble for a random process X(t).

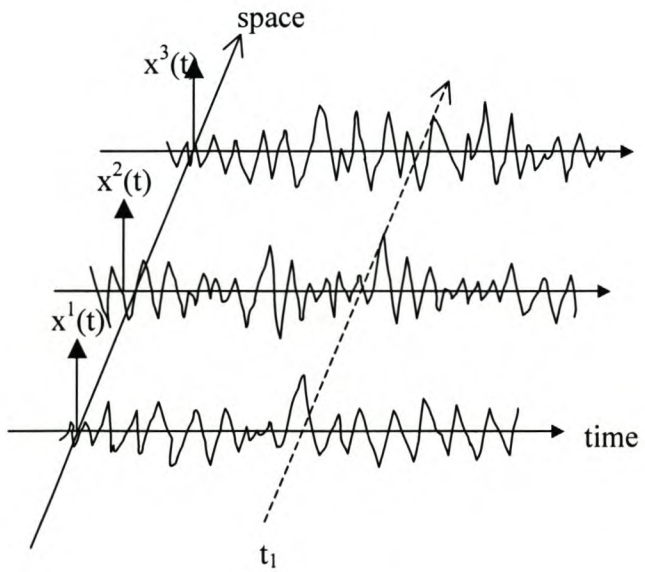

Fig. C-1 Example of random process samples

Fig. C-1 shows three samples $x^1(t)$, $x^2(t)$ and $x^3(t)$ of infinite sample values of some random variables X(t) in space and time. Each sample is taken as a function of time and has infinite values. If we take the values of the three samples at some time, say t_1, the three values $x^1(t_1)$, $x^2(t_1)$ and $x^3(t_1)$ are among the infinitely many in the ensemble representing the random variable X(t), say X_1 at time

t_1. The values of random variable $X(t_1) = X_1$, are calculated using the following probability definition.

The probability of X(t) in an interval of x and x + *d*x is the ratio of the values of X(t) in the given interval to the total expected values of X(t) at time t_1. Or in shorthand:

$$P(x < X < x + dx) = \lim_{N \to \infty} \frac{n}{N} \quad \text{... C-1}$$

Where P is the probability of the random process X(t) in the interval x and x + dx, N is the total number of samples in the ensemble and n is the number of samples between x and x + dx.

In practice it is not possible to have an amount of infinite samples. Most experimental practices are limited to have a limited number of samples. And sometimes they even work with a single sample only. That means, all the statistical parameters used to define the random variable are extracted from the single sample. For some stationary random processes called ergodic, the statistics extracted form a single, but long sample function of time called temporal statistics, approximate the ensemble statistics quite well [9]. Random processes are stationary if their statistical values (mean, variance, etc) do not change in time. The following note of some statistical terms are all for an ergodic stationary process which is relevant to the experimental samples of this report.

C-1 Probabilistic Density

The probability density p(x) is defined by the rate of the probable samples in an interval, so that the integral sum of all the probable or favourable samples give the probability of the random process in the same interval.

$$P(x_1 < X < x_2) = \int_{x_1}^{x_2} p(x)dx \quad \text{... C-2}$$

$$P(-\infty < X < \infty) = \int_{-\infty}^{\infty} p(x)dx = 1.0 \quad \text{... C-3}$$

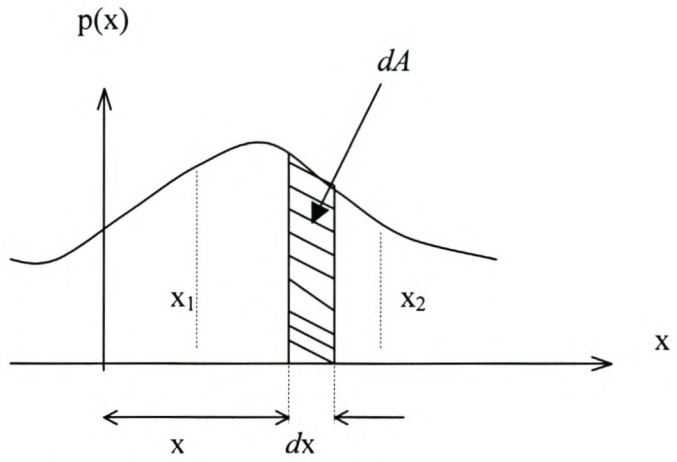

Fig. C-2 Probability density function of the random variable X

dA – is the elemental area which denotes the probability of the random process X between x_1 and x_2.

For a pair of random variables X_1 and X_2 the probability density $p(x_1,x_2)$ is defined similarly to give the probability volume of area dx_1dx_2 and height $p(x_1,x_2)$.

$$P(x_1 < X_1 < x_1 + dx_1 \text{ and } x_2 < X_2 < x_2 + dx_2) = p(x_1, x_2)dx_1dx_2 \quad \textbf{... C-4}$$

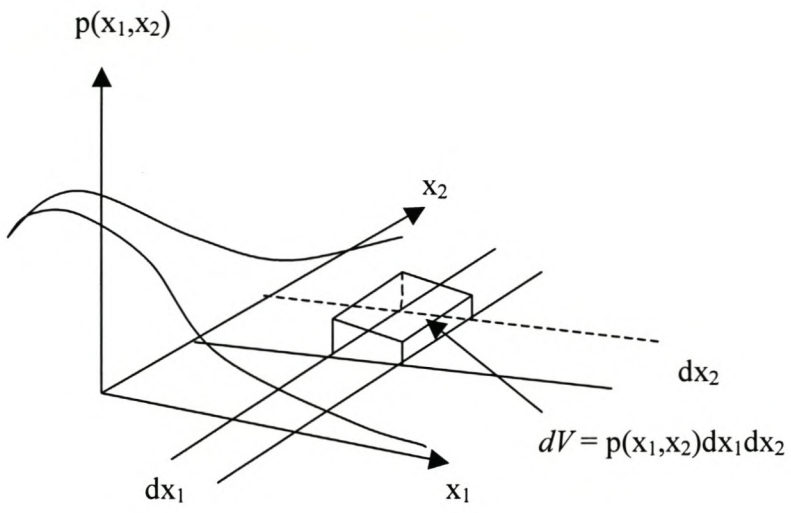

Fig. C-3 Probability density of two random variables X1 and X2

dV – is the elemental volume denoting the probability that the random variable X1 be in the interval dx_1 and X2 in the interval dx_2.

$$P(a < X_1 < b \text{ and } c < X_2 < d) = \int_{x_1=a}^{b} \int_{x_2=c}^{d} p(x_1, x_2) dx_1 dx_2 \quad \text{... C-5}$$

$$P(-\infty < X_1 < \infty \text{ and } -\infty < X_2 < \infty) = \int_{-\infty}^{\infty} \int_{-\infty}^{\infty} p(x_1, x_2) dx_1 dx_2 \quad \text{... C-6}$$

From the definition of the joint probability $p(x_1,x_2)$ the individual probability densities can also be derived. The probability of X_1, irrespective of X_2 is

$$P(x_1 < X_1 < x_1 + dx_1) = p(x_1) dx_1 = \int_{x2=-\infty}^{\infty} p(x_1, x_2) dx_1 dx_2$$

Then the $p(x_1)$ is given by

$$p(x_1) = \int_{-\infty}^{\infty} p(x_1, x_2) dx_2 \quad \text{... C-7}$$

Similarly

$$p(x_2) = \int_{-\infty}^{\infty} p(x_1, x_2) dx_1 \quad \text{... C-8}$$

C-2 Statistical Terminologies

For a continuous random variable X(t) the following statistical concepts are defined by:

a. Average: the average or the expectation value of a random temporal process X(t) is the value where the random variable stays most.

$$E(X) = \lim_{T \to \infty} \frac{1}{T} \int_0^T x(t) dt \quad \text{... C-9}$$

b. Variance: the average of the square of deviation from the mean.

$$\sigma^2 = E[(X - E(X))^2] \quad \text{... C-10}$$

c. Standard Deviation (σ)**:** the square root of the variance. It measures the scatter of the random variable for the mean value.

d. Correlation: the ensemble of the product of two random variables. Correlation measures the change of one random variable in relation to the other.

$$E(X_1, X_2) = \lim_{T \to \infty} \frac{1}{T} \int_0^T x_1(t) x_2(t) dt \quad \text{... C-11}$$

e. Co-variance: is defined as the average across the ensemble of all products of deviation.

$$\text{cov}(X_1, X_2) = E\{[X_1 - E(X_1)][X_2 - E(X_2)]\} \quad \text{... C-12}$$

f. Correlation Coefficient: is the normalised co-variance.

$$\rho = \frac{\text{cov}(X_1, X_2)}{\sigma_1 \sigma_2} \quad \text{... C-13}$$

C-3 Autocorrelation and Spectral Density

Random processes that have different statistical values at different times are non-stationary processes. On the other hand, those having constant statistical values are stationary processes. Specifically, a random process X(t) is strongly stationary if all orders of its probability functions are stationary. But for weakly stationary processes, applicable for most applications of random processes, only some of its statistics are constant [9]. For a stationary random process:

Mean $= \mu = E[X(t_1)] = E[X(t_2)]$ **... C-14**

Variance $= \sigma^2 = E\{[X(t_1) - \mu]^2\} = E\{[X(t_2) - \mu]^2\}$ **... C-15**

Similarly, for two random variables $X(t_1)$ and $X(t_2)$ at time t_1 and t_2 respectively, having a time lag of $\tau = t_2 - t_1$, the co-variance and correlation are functions of the time lag only (weakly stationary).

Co-variance = $\mathbf{E\{[X(t_1) - \mu][X(t_2) - \mu]\}}$

$$= \mathbf{E[X(t_1)X(t_1+\mu)] - \mu^2} \quad \text{... C-16}$$

And the correlation function is

$$\mathbf{R(\tau) = E[X(t_1)X(t_1 + \tau)]} \quad \text{... C-17}$$

a. Autocorrelation

The correlation function equation (C-17) is called an autocorrelation function in random vibration if the two random variables $X(t_1)$ and $X(t_2)$ are for the same process X(t), and are denoted by

$$\mathbf{R(\tau) = E[X(t)X(t + \tau)]} \quad \text{... C-18}$$

When two random processes, X1(t) and X2(t) are involved, the cross-correlation term is used.

The autocorrelation function has small values except at $\tau = 0$, for the stationary random process having zero mean. For functions having their values $X(t) \cong X(t+ \tau)$, $R(\tau)$ has almost a constant value with a maximum of the mean square. Some properties of the autocorrelation function are:

- $R(0) = E(X^2)$ – ensemble mean square
- Is even function of τ
- As $\tau \rightarrow \infty$, X(t) will be independent of $X(t + \tau)$. Thus $R(\tau) \rightarrow [E(X)]^2$.
- If the random process has a periodic function part, the autocorrelation function of the random process will be also a periodic function of the same period with the periodic part of the random process.

b. Spectral Density

In most engineering applications, problems are expressed as functions of frequency instead of time. Because of this, the frequency transform of the autocorrelation function known as Power Spectral Density, PSD, is more often used.

Taking the Fourier transform of $\frac{R(\tau)}{2\pi}$, from equation (B-6)

$$S(\omega) = \frac{1}{2\pi}\int_{-\infty}^{\infty} R(\tau)e^{-i\omega\tau}d\tau \quad \text{... C-19}$$

R(τ) is absolutely integrable as long as the random process has no purely periodic part and its mean value is zero or filtered out. Then, the inverse Fourier transform of S(ω) is

$$R(\tau) = \int_{-\infty}^{\infty} S(\omega)e^{i\omega\tau}d\omega \quad \text{... C-20}$$

Some of the properties of the power spectral density are:

- $R(0) = E(X^2) = \int_{-\infty}^{\infty} S(\omega)d\omega$ **... C-21**

S(ω) is real and an even function of ω because R(τ) is real and even.

- The negative frequency is only the two-sided Fourier elements of the function. It does not mean the existence of negative frequency.
- S(ω) ≥ 0. As it represents the ensemble means square per unit frequency.

Appendix D TRAILER DIMENSIONS AND PARTS

D-1 Major Parts Specification of Semi-Trailer

Parts Dimensions of Semi-Trailer				
Part	Sub-Part	Dimension (mm)	Comment(1)	Comment(2)
Chassis Flange	Flange	12200*100*16		
Chassis Web	Neck	3660*118*8		
	Taper	1810* _*8		
	Rear	6730*453*8		
Deck		12200*2600*3		
Deck Edge Beams		118*59*9	U-Channels	Deck length
Interlink Plate		2300*110*8		approximate
Deck Cross Bars(small)		100*50*5		Deck width
Deck Cross Bars(big)		230*60*5	U-Channels tapered from the chassis outward	Deck width
Chassis Stiffeners , at the suspension		185*125*45*45	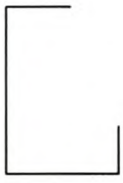	
Ceiling Beams	Central	60*40*4		
	Side beams	100*50*4		
	Front and rear sides	70*70*4		
Corner Ceiling Supporting Beams		2760*150*70*5	L-Beam	

D-2 Chassis Drawing of Semi-Trailer

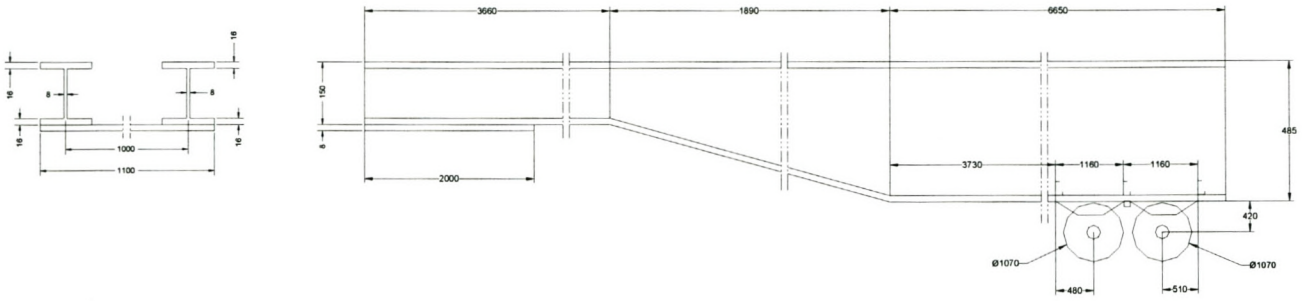

Appendix E EXPERIMENTAL RESULT PLOTS

E-1 Measured Inputs

1. 70km/h Speed Forcing Function Plots

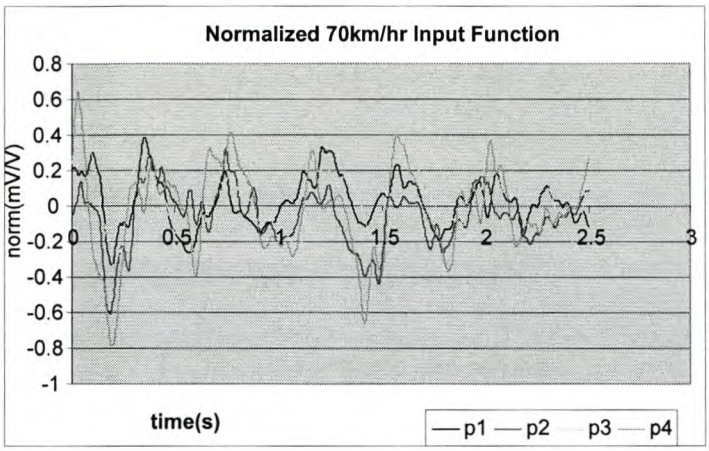

a. Sample input between 0 and 2.5 s

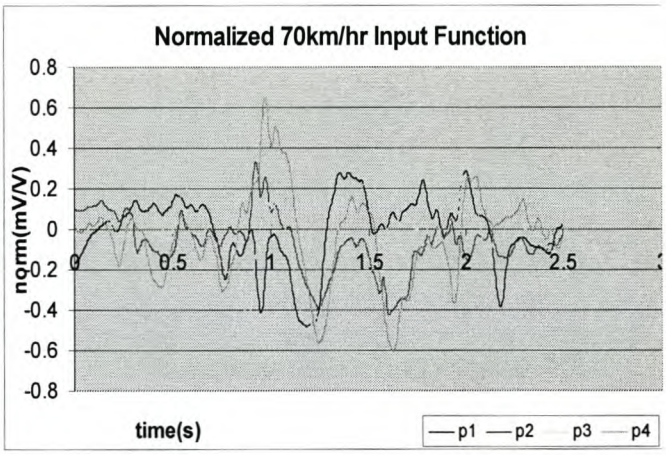

b. Sample input between 10 and 12.5 s

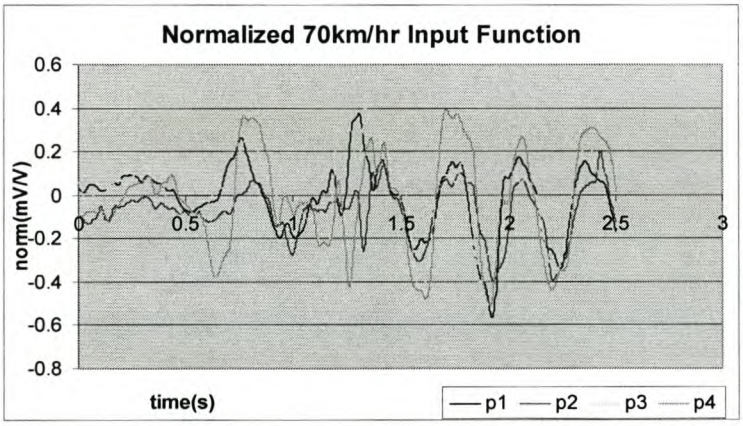

c. Sample input between 17 and 19.5 s

Fig. E-1 70km/h test forcing function plots

2. 50km/h Speed Forcing Function Plots

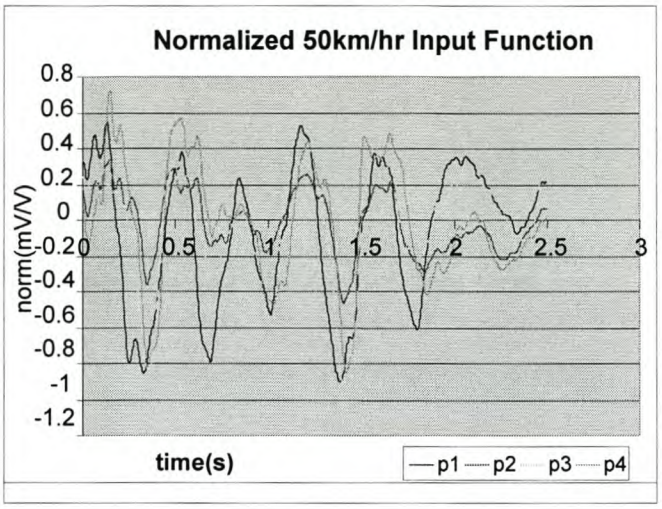

a. Sample data between 2 and 4.5 s

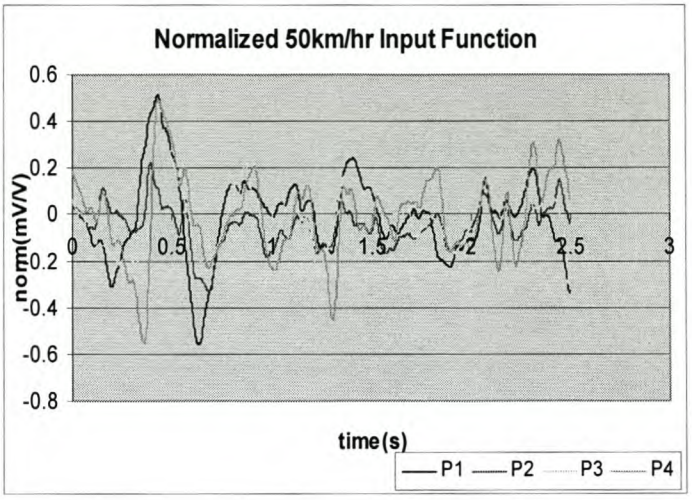

b. Sample data between 11 and 13.5 s

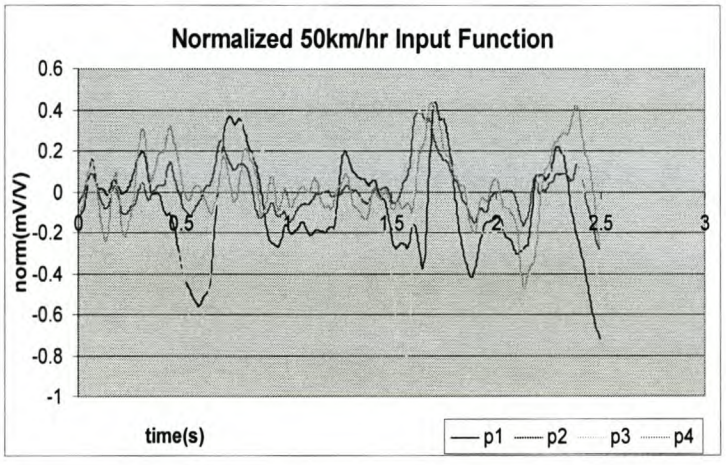

c. Sample data between 13 and 15.5 s

Fig. E-2 50km/h test forcing function plots

3. 40km/h Speed Test Forcing Function Plot

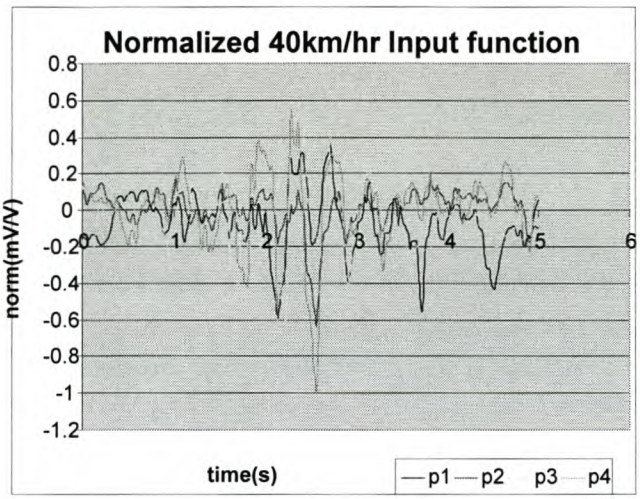

a. Sample Plot between 0 and 5 s

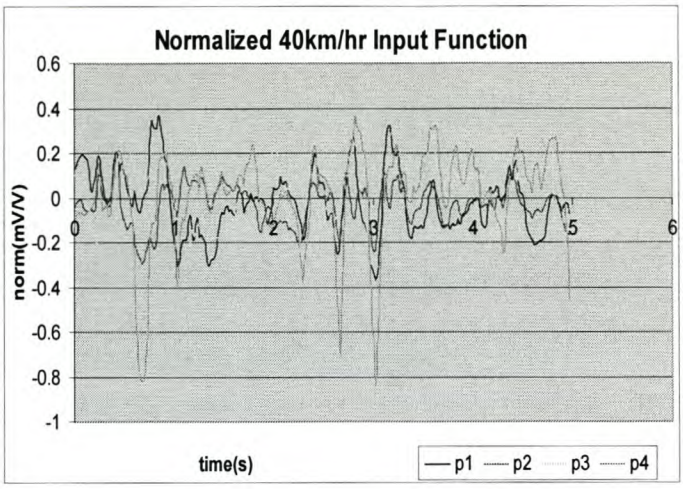

b. Sample Plot between 10 and 15 s

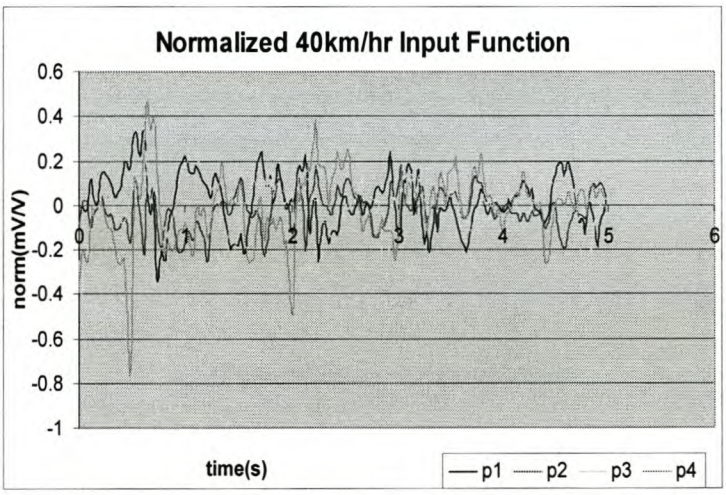

c. Sample Plot between 15 and 20 s

Fig. E-3 40km/h test forcing function plots

E-2 Measured Outputs

1. 70km/h Strain in micro-strain (μm/m) between 0 and 2.5 Seconds

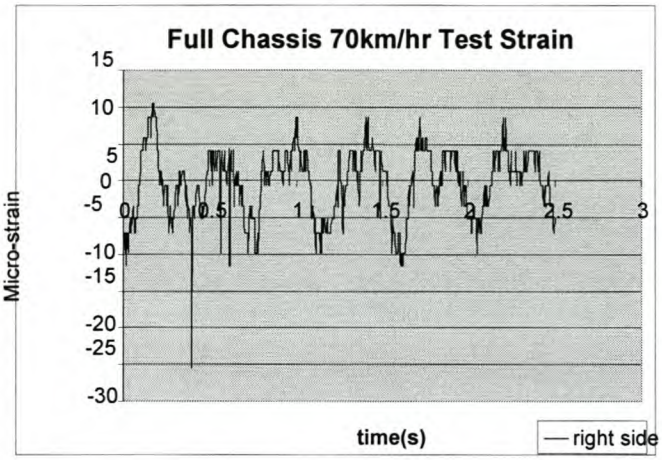

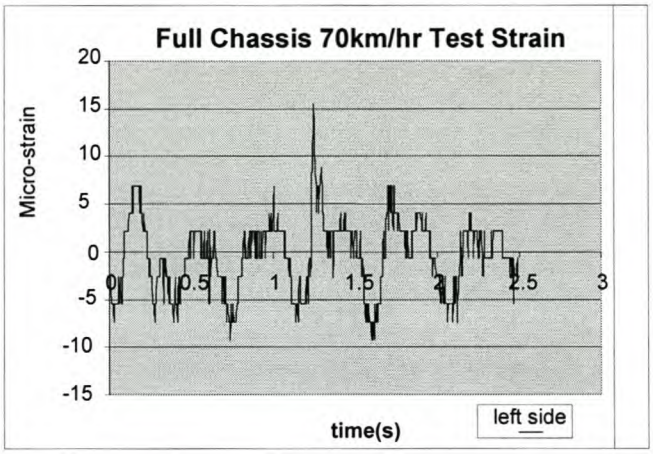

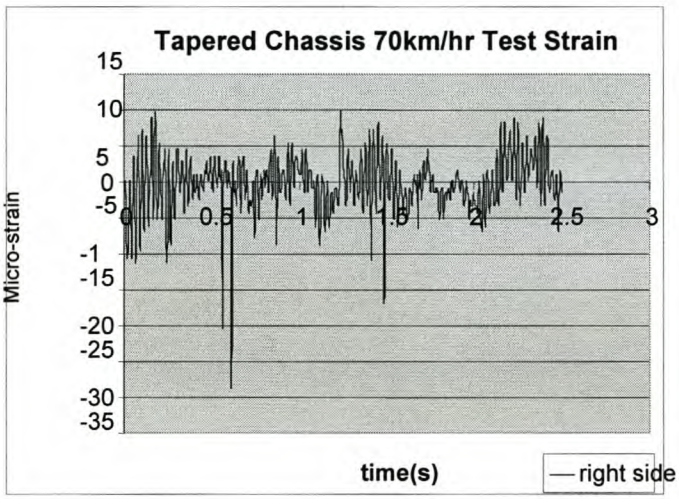

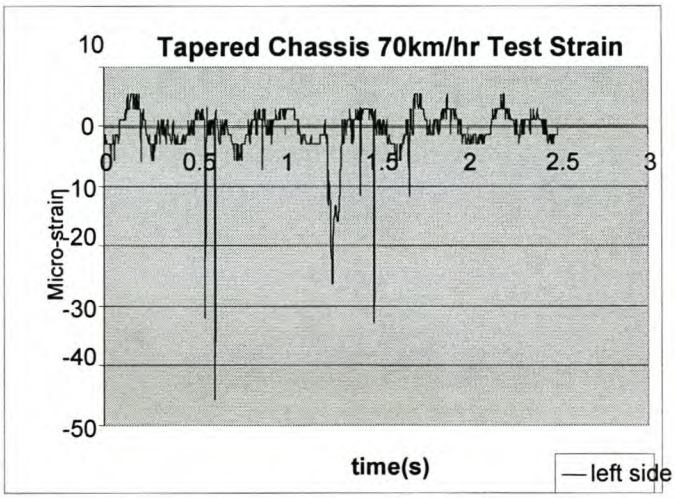

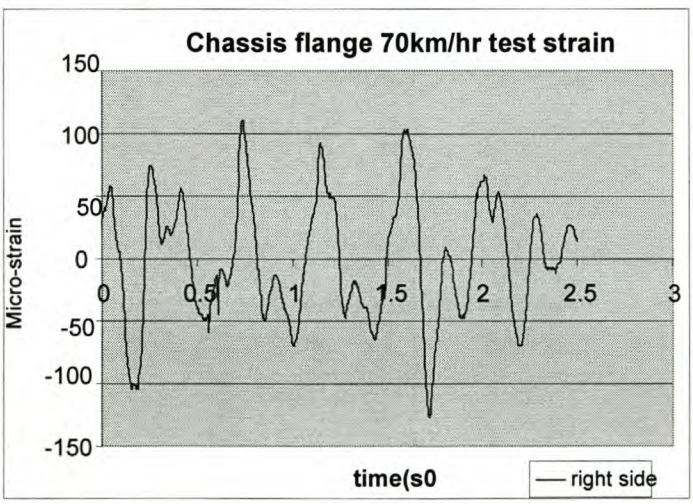

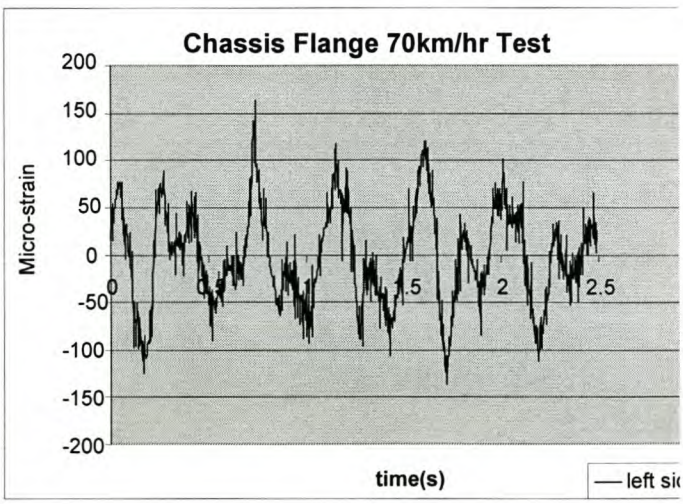

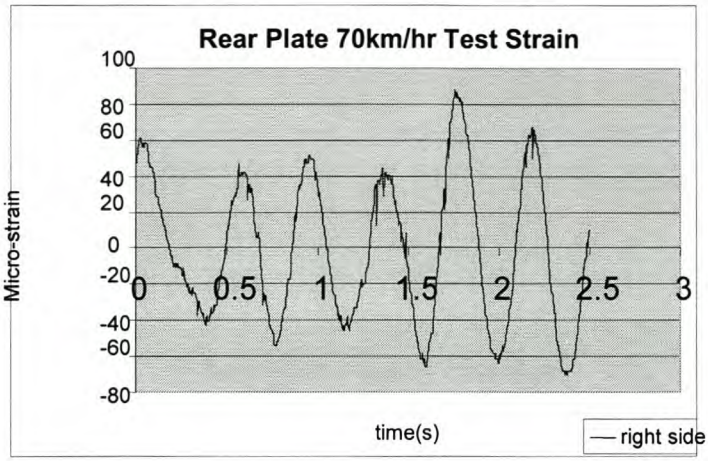

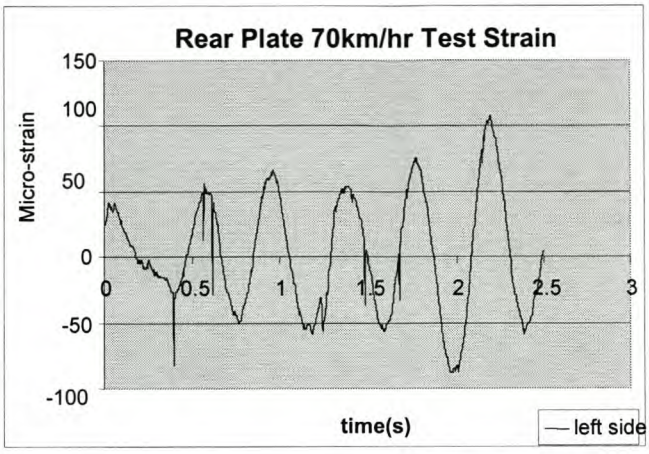

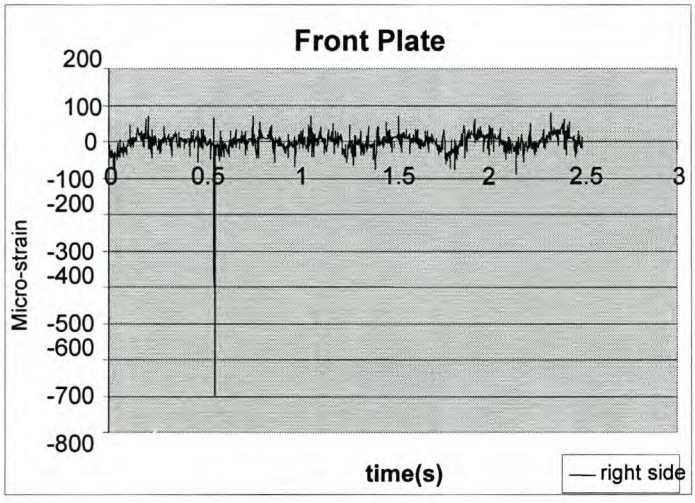

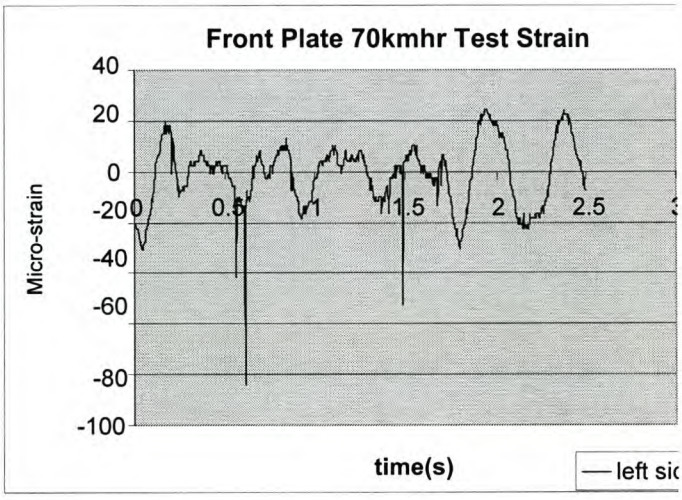

Fig. E-4 70km/h measured strain plots

2. 50km/h Test strain in micro-strain (μm/m) between 0 and 2.5 Seconds

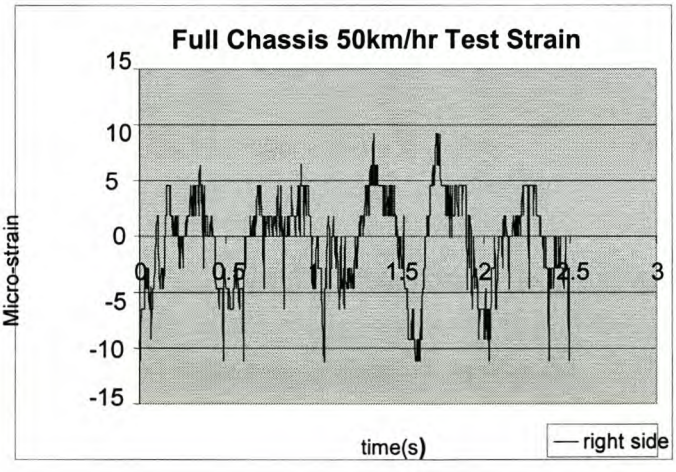

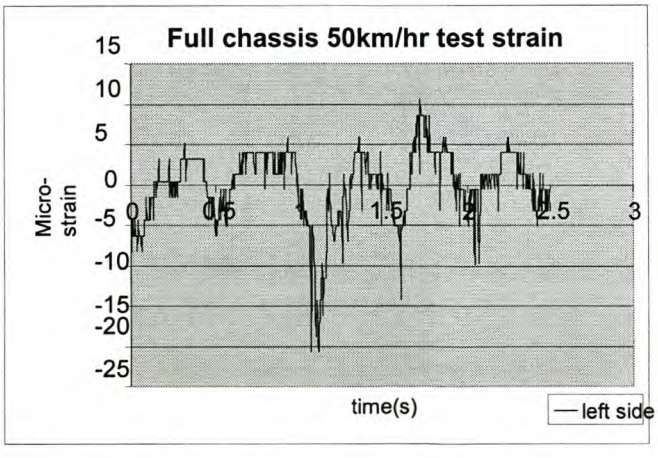

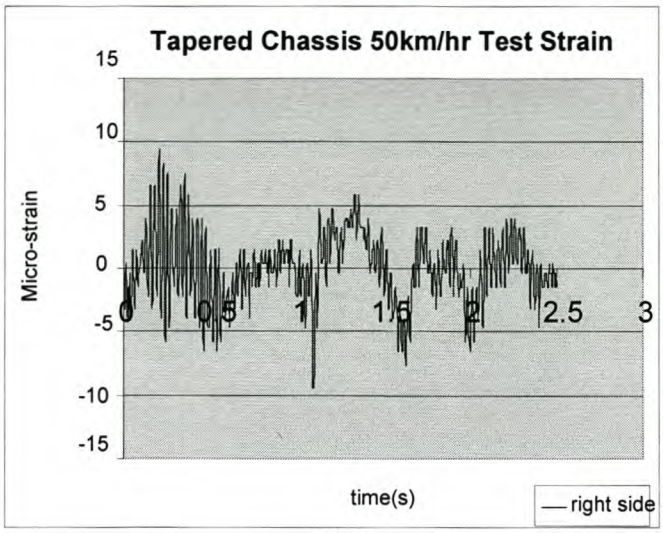

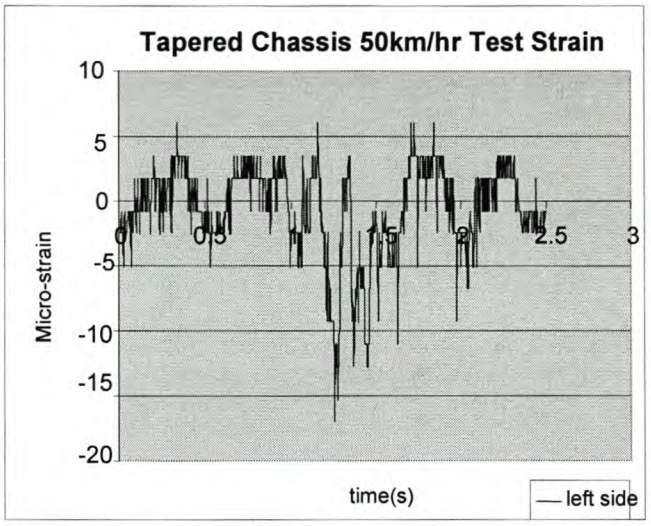

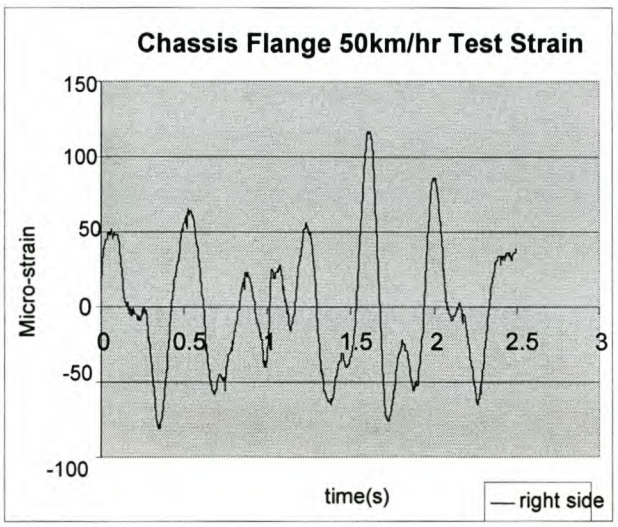

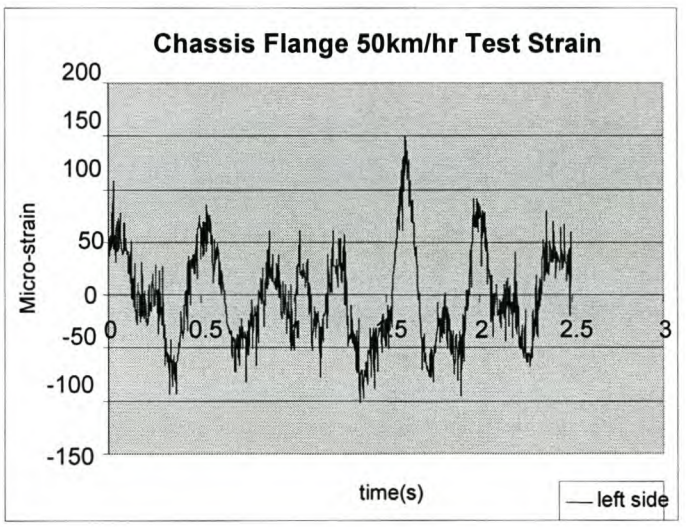

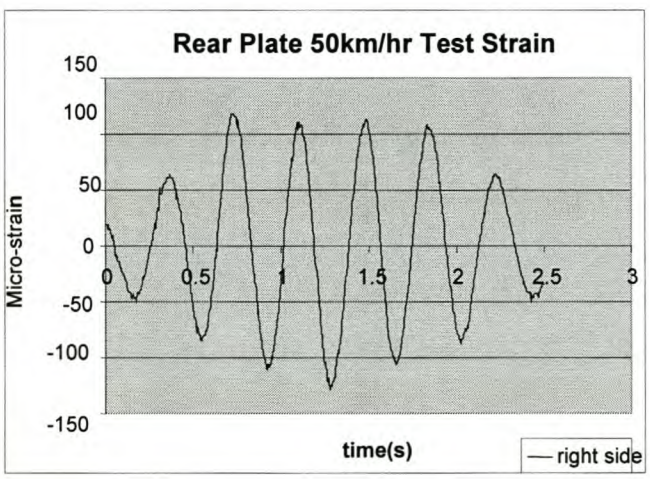

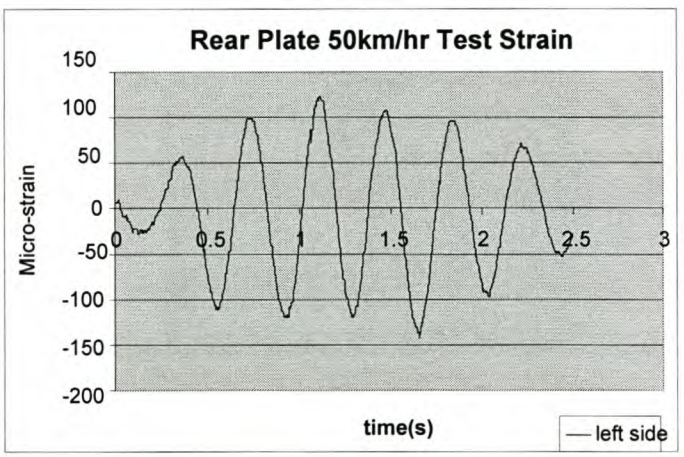

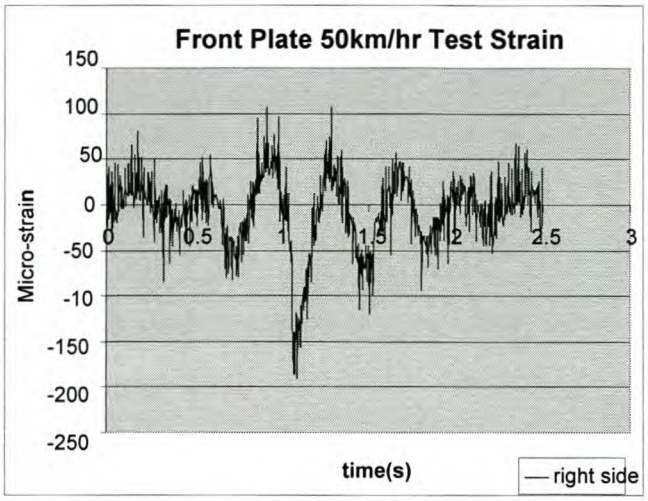

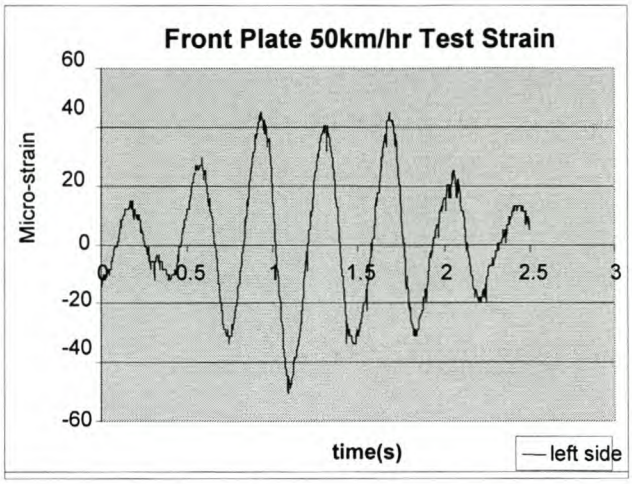

Fig. E-5 50km/h measured strain plots

3. 40km/h Speed test strain in micro-strain (μm/m) between 0 and 5 Seconds

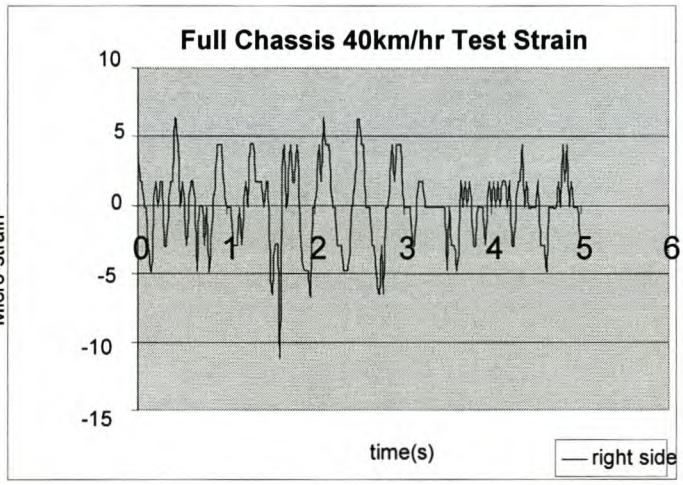

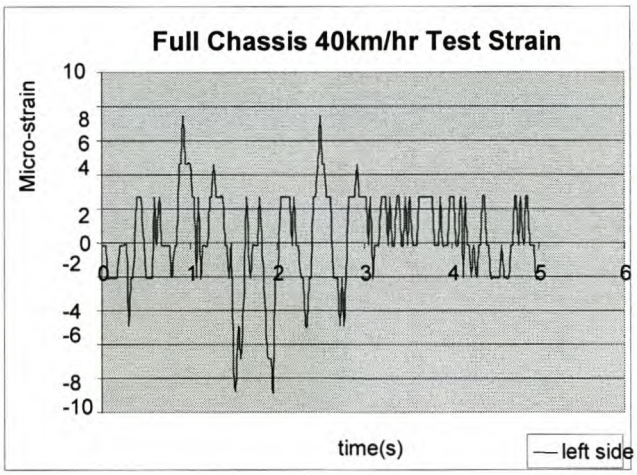

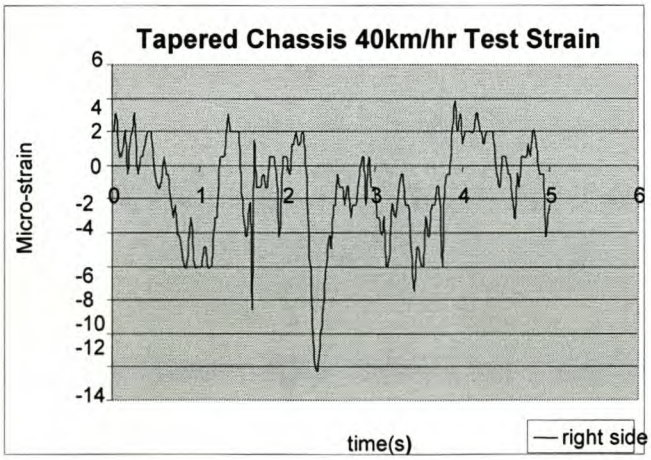

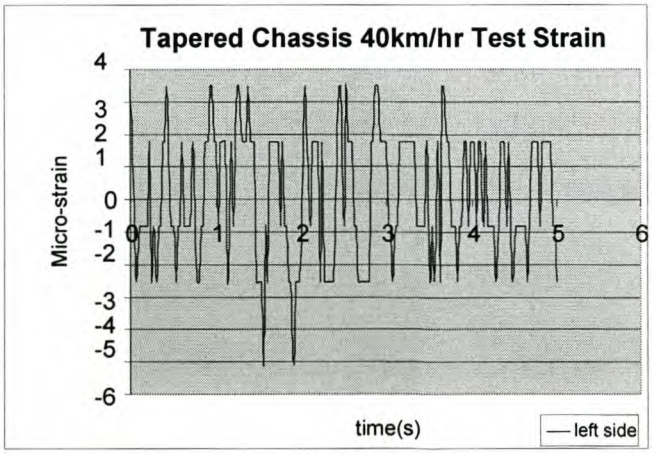

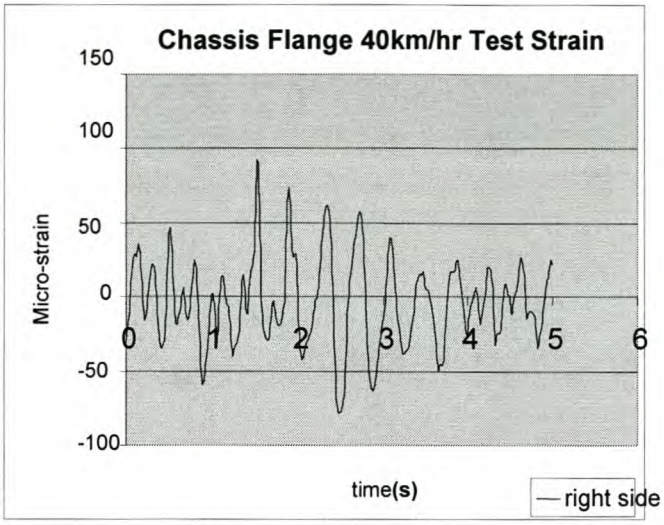

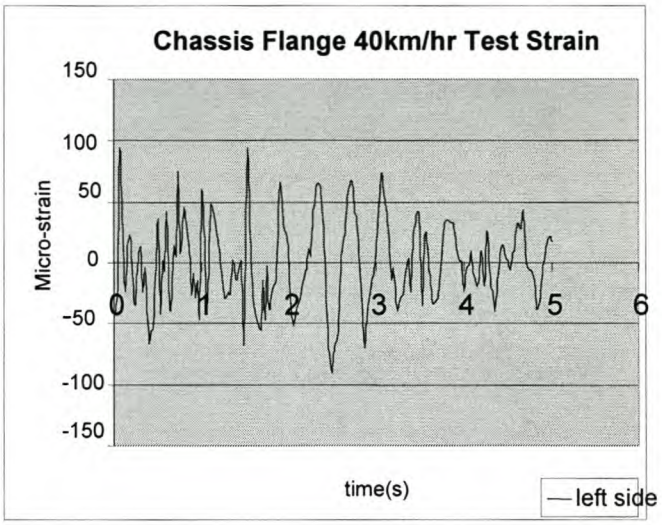

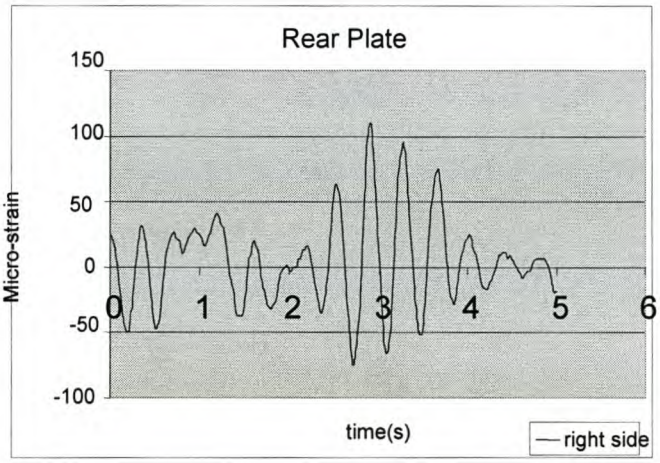

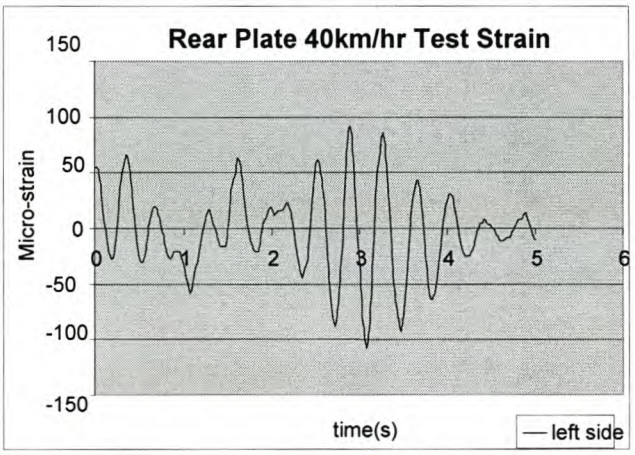

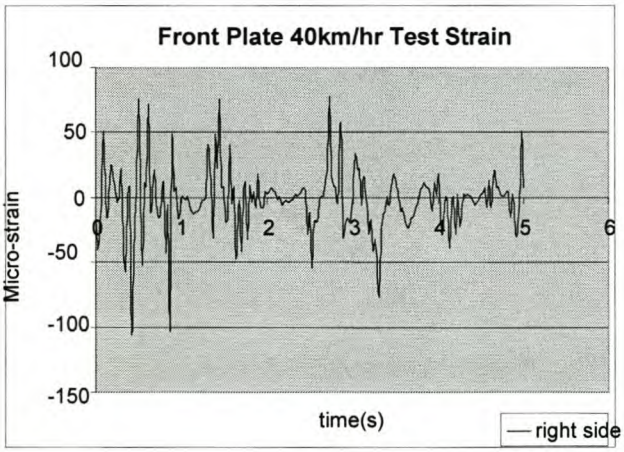

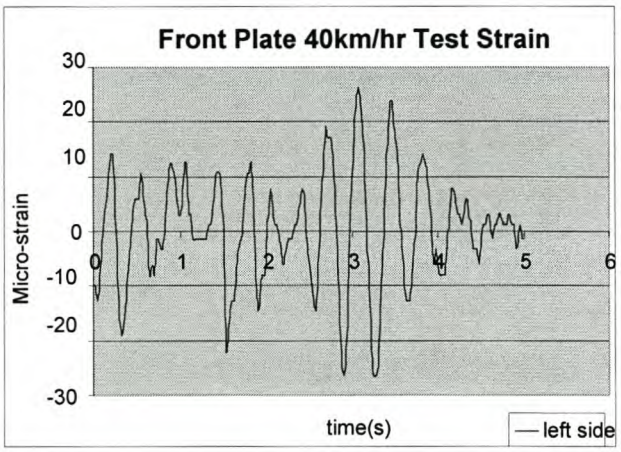

Fig. E-6 40km/h measured strain plots

Appendix F FINITE ELEMENT ANALYSIS RESULTS

F-1 70km/h Test Finite Element Analysis Plots

I. Finite Element Analysis Strain Result for the 70km/h Test Between 0 and 2.5 Seconds

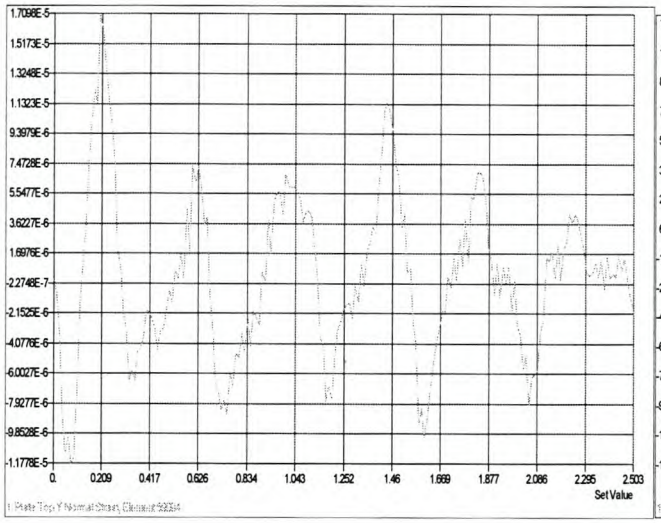

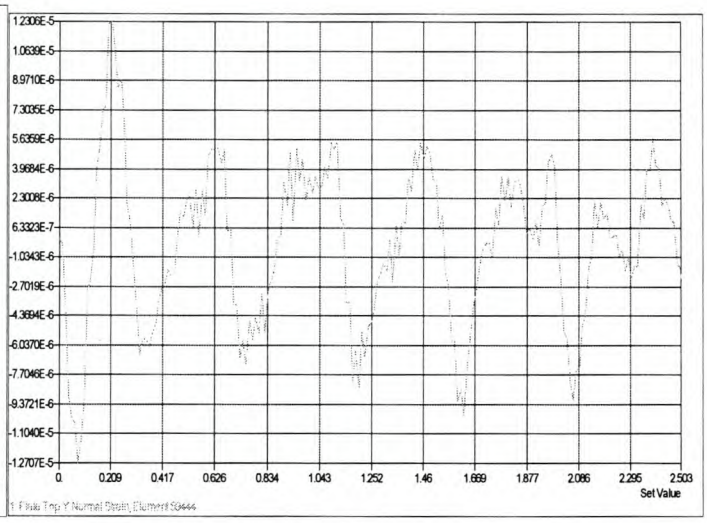

a. Right side b. Left side

1. Full chassis finite element strain result for the 70km/h speed

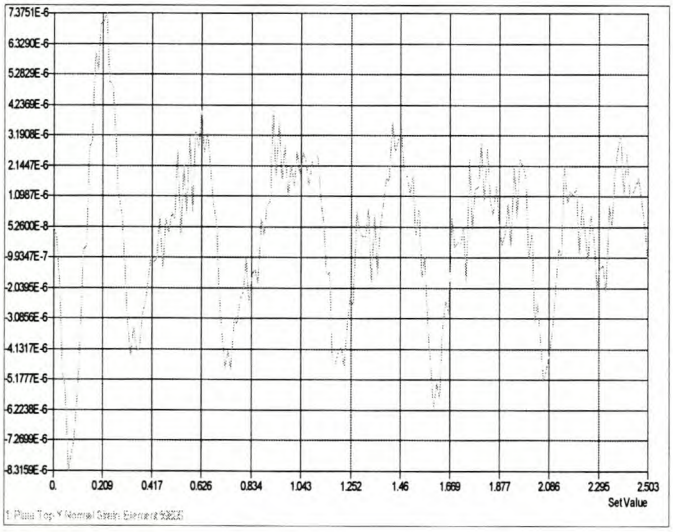

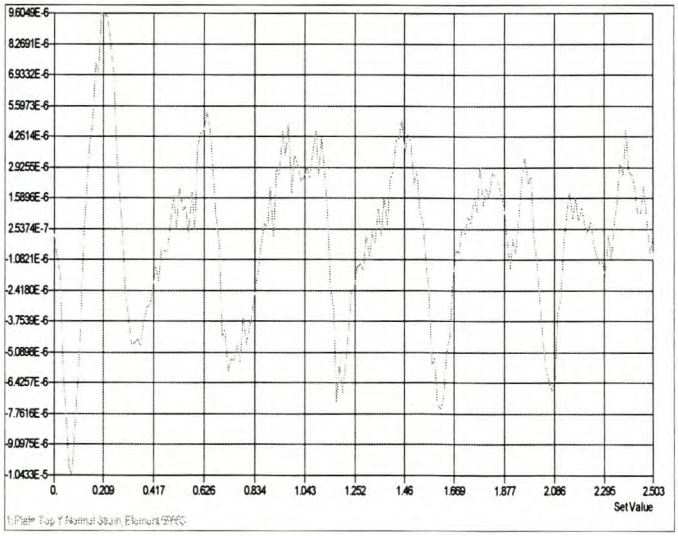

a. Right side b. Left side

2. Tapered chassis finite element strain result for the 70km/h speed

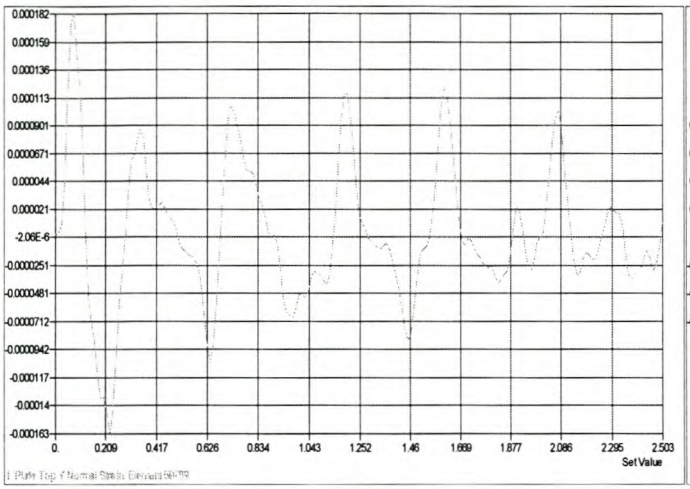

a. Right side

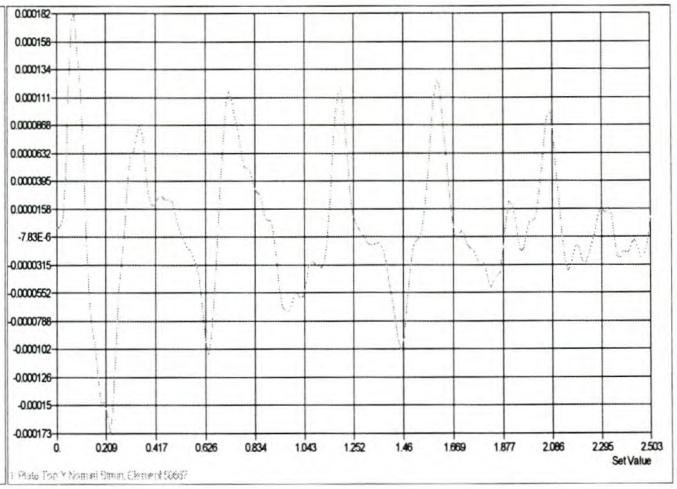

b. Left side

3. Chassis neck finite element strain result for the 70km/h speed

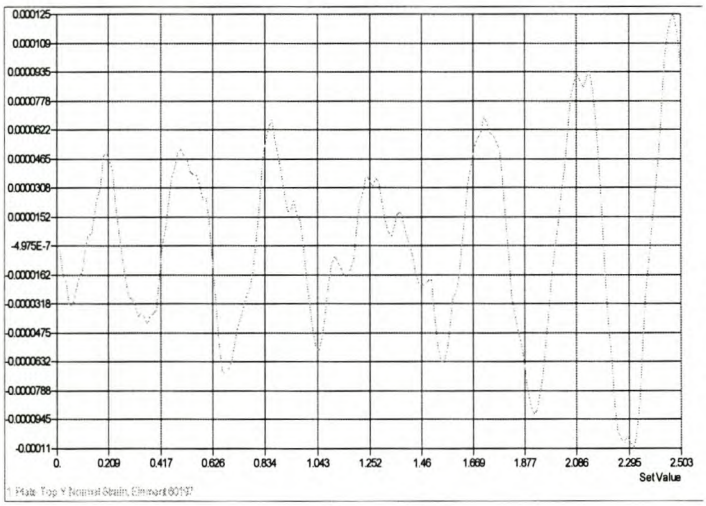

a. Right side

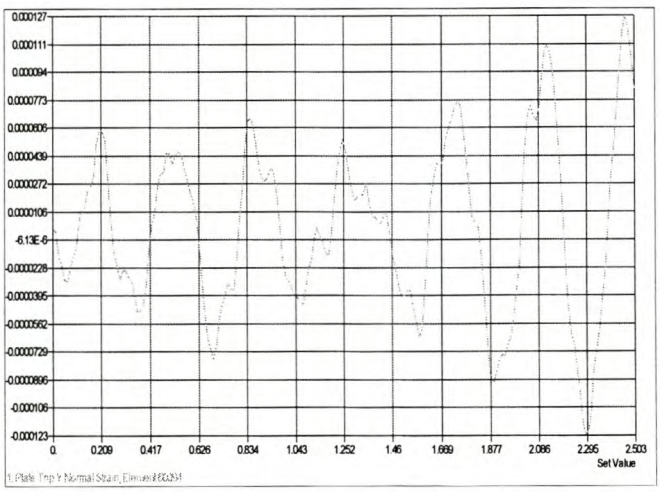

b. Left side

4. Rear plate finite element strain result for the 70km/h speed

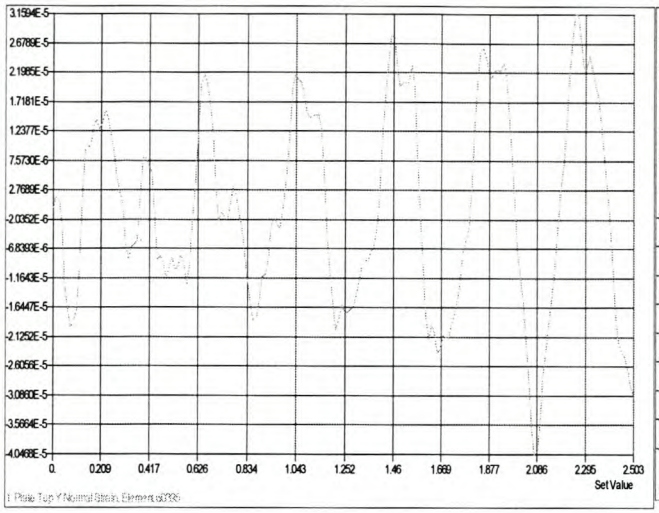

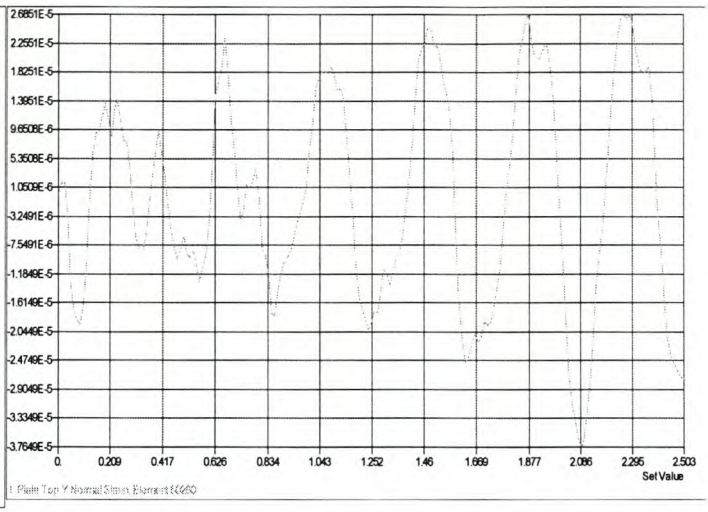

a. Right side b. Left side

5. Front plate finite element strain result for the 70km/h speed

II. Finite Element Analysis Strain Result for the 70km/h Test Between 10 and 12.5 Seconds

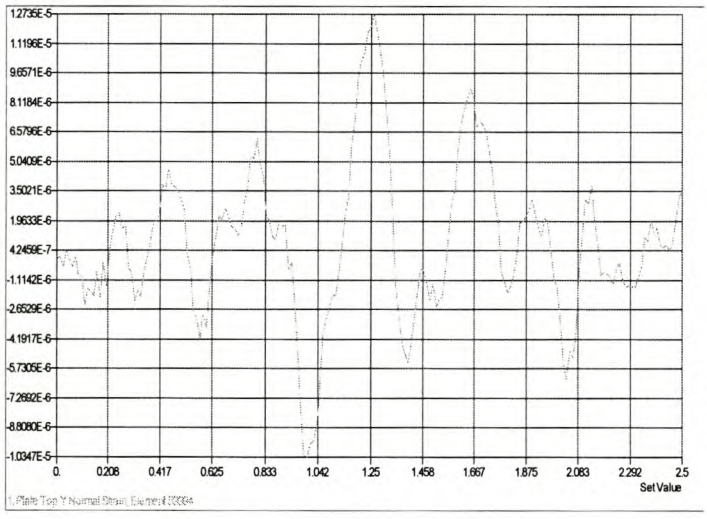

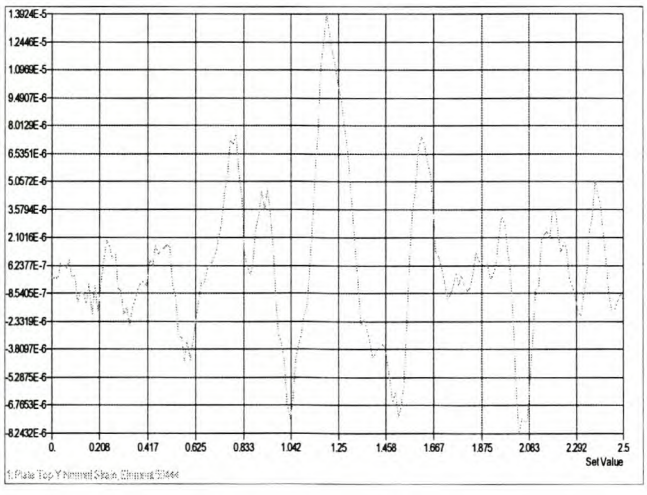

a. Right side b. Left side

6. Full chassis finite element strain result for the 70km/h speed

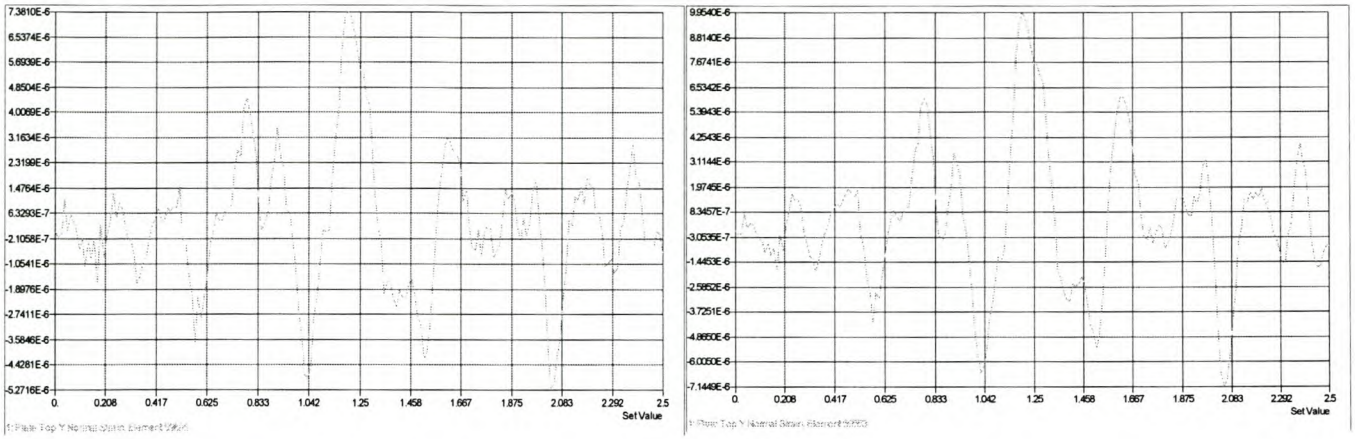

a. Right side b. Left side

7. Tapered Chassis finite element strain result for the 70km/h speed

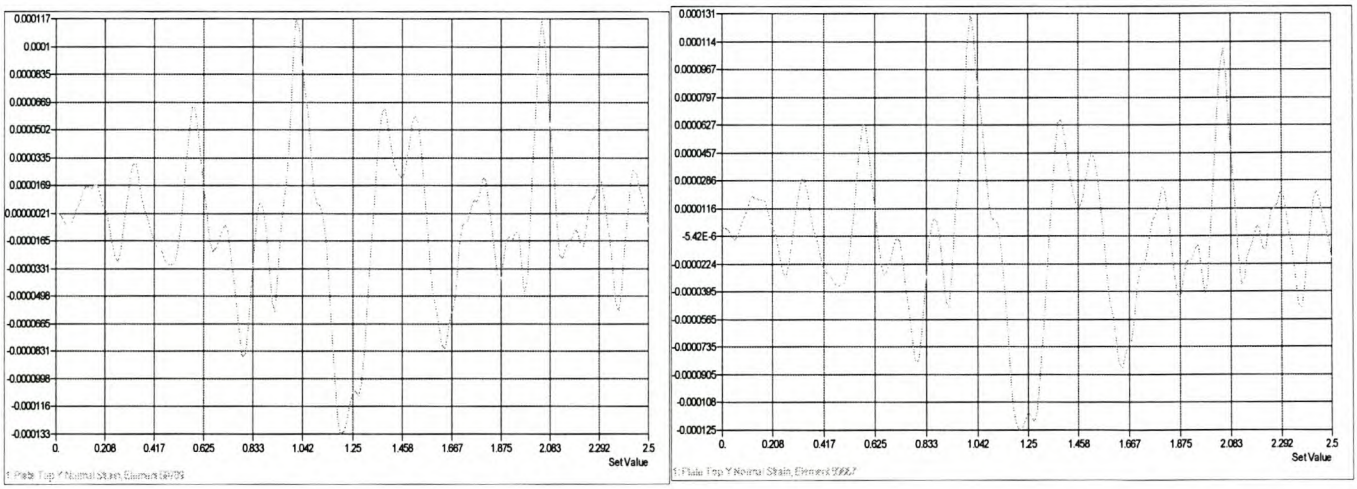

a. Right side b. Left side

8. Chassis neck finite element strain result for the 70km/h speed

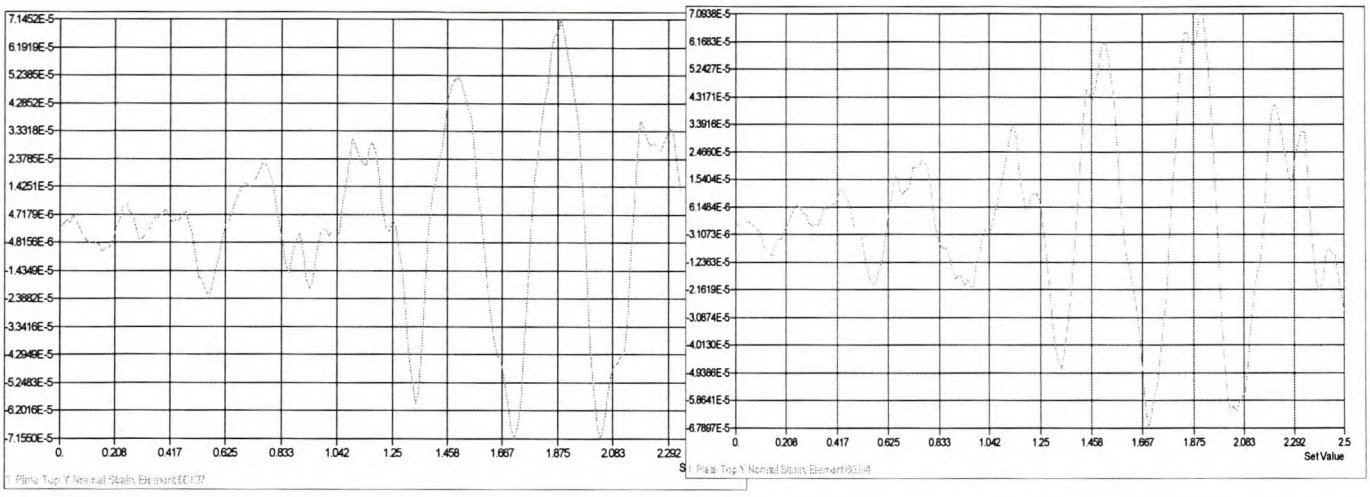

a. Right side b. Left side

9. Rear plate finite element strain result for the 70km/h speed

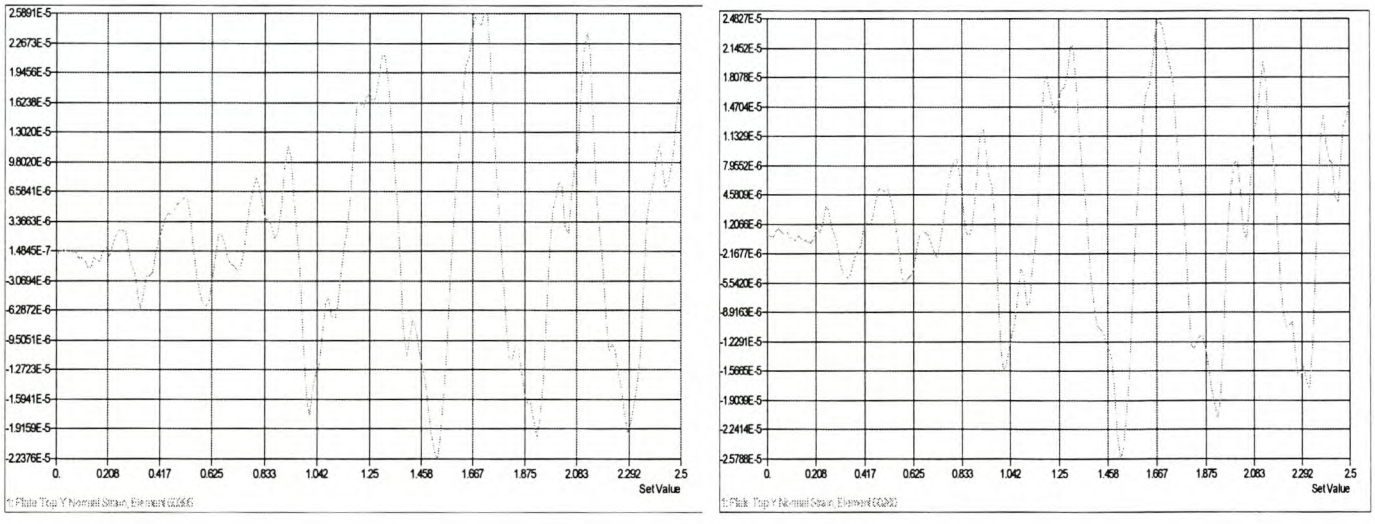

a. Right side b. Left side

10. Front plate finite element strain result for the 70km/h speed

III. Finite Element Analysis Strain Result for the 70km/h Test
Between 17 and 19.5 Seconds

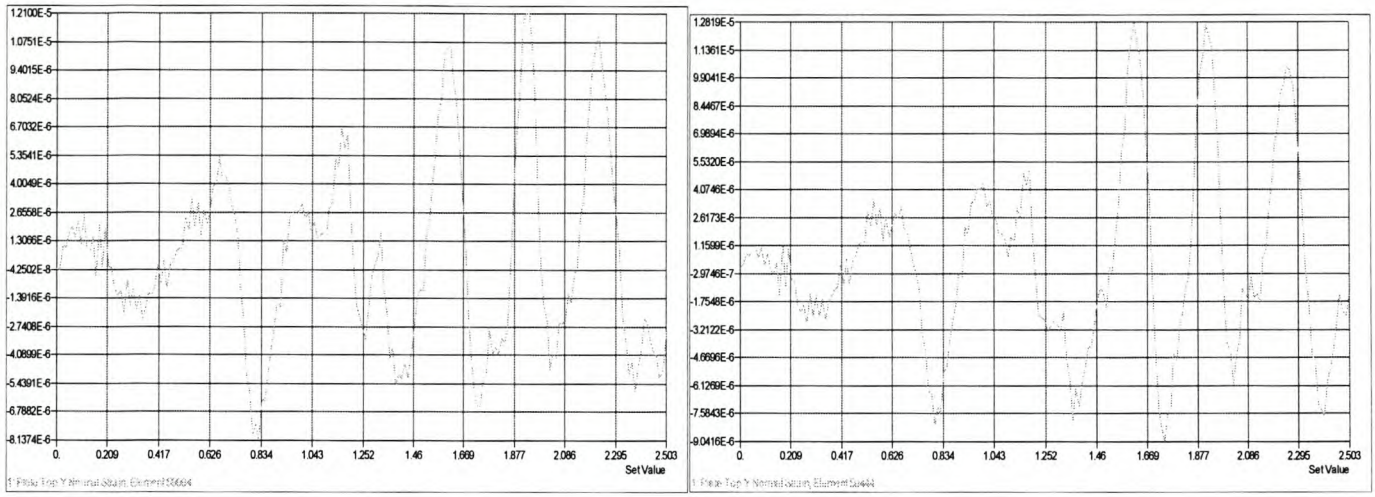

a. Right side b. Left side

11. Full chassis finite element strain result for the 70km/h speed

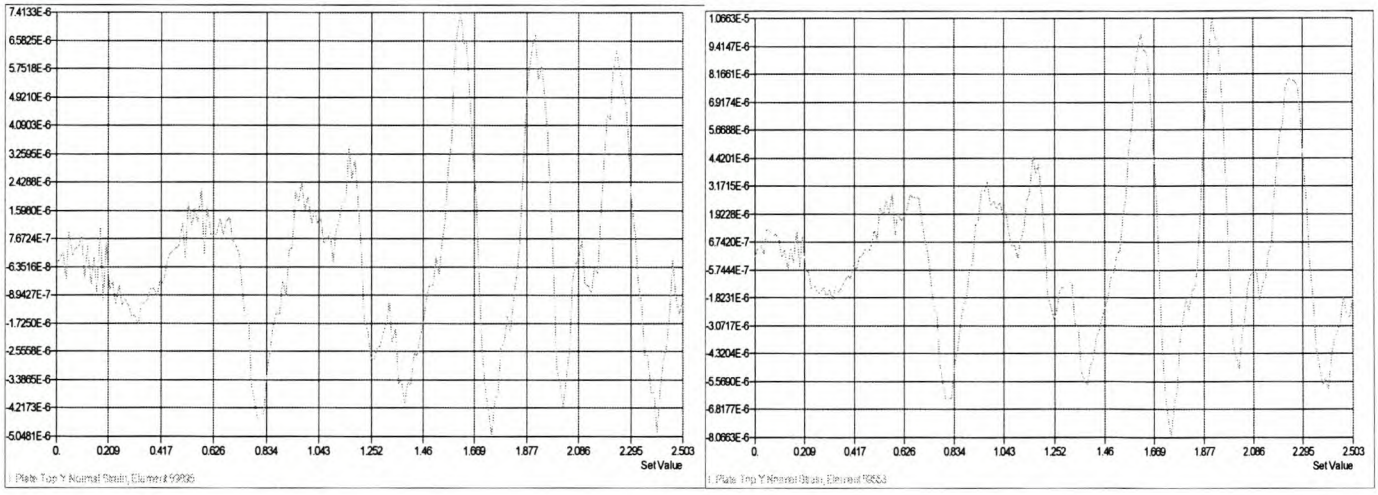

a. Right side b. Left side

12. Tapered chassis finite element strain result for the 70km/h speed

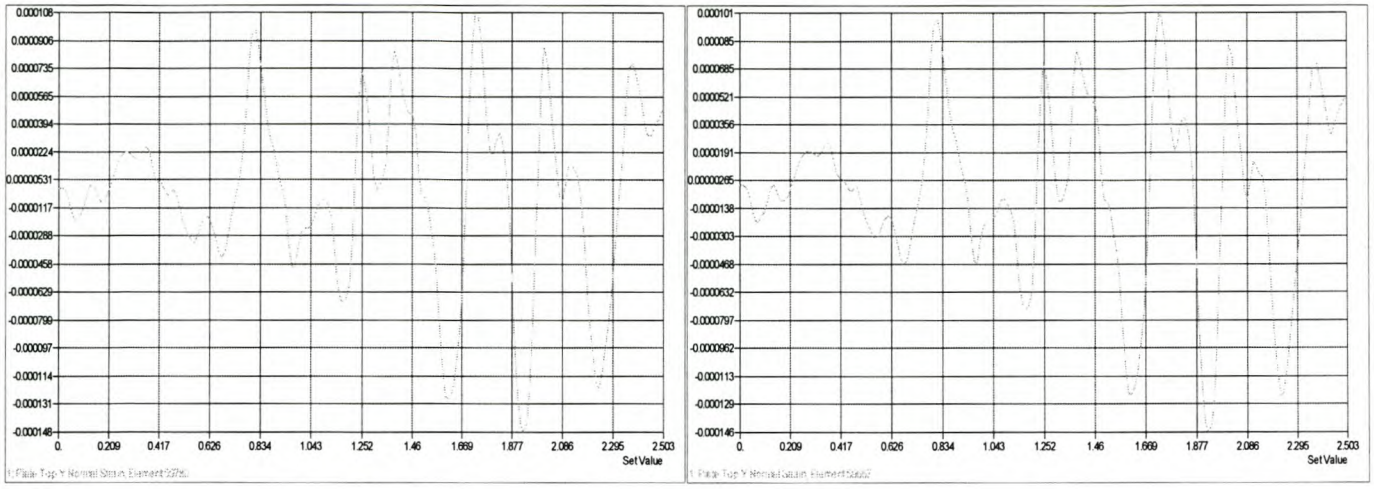

a. Right side b. Left side

13. Chassis neck finite element strain result for the 70km/h speed

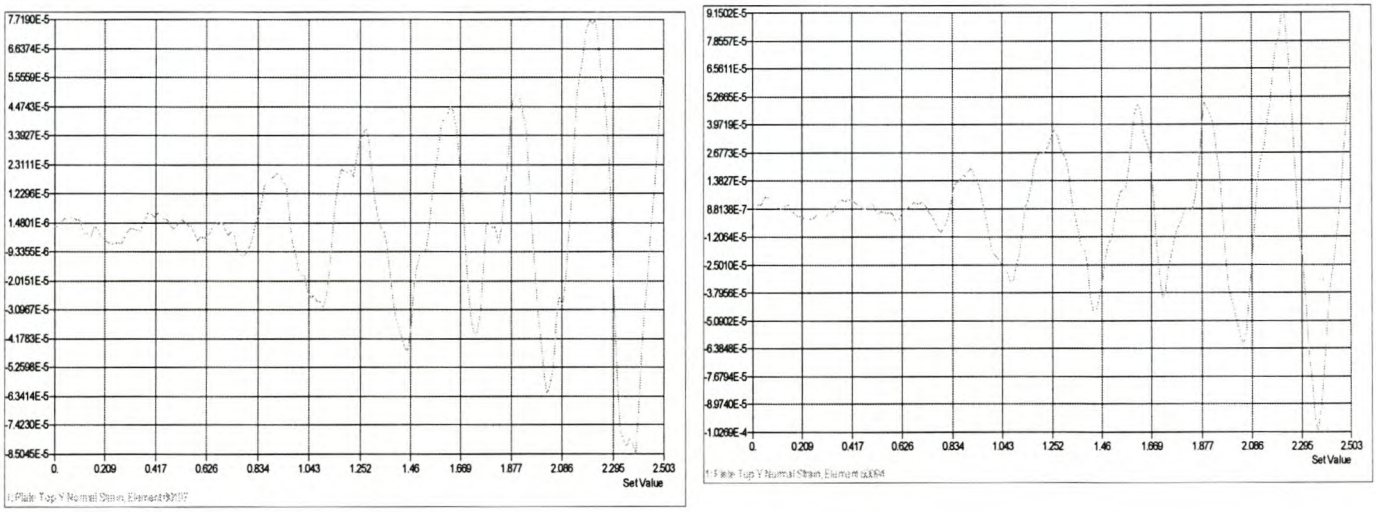

a. Right side b. Left side

14. Rear plate finite element strain result for the 70km/h speed

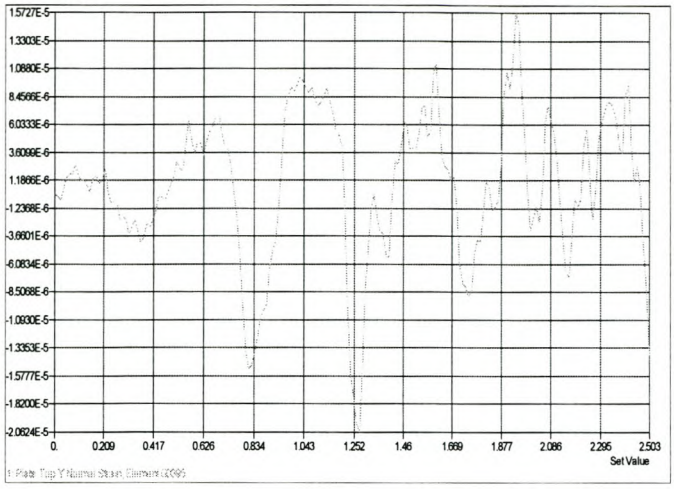

a. Right side

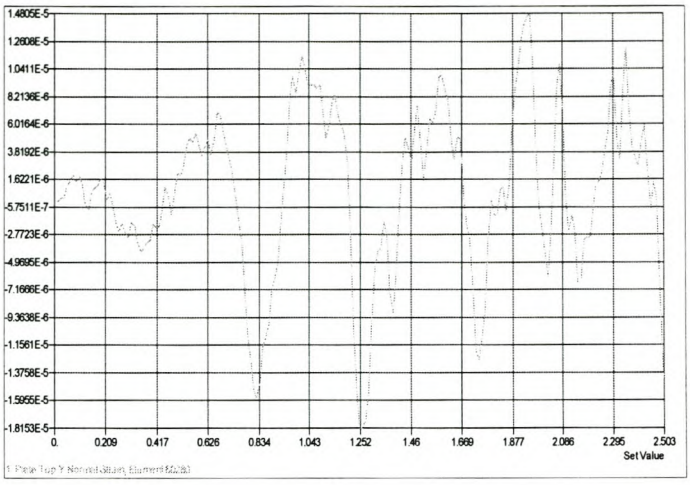

b. Left side

15. Front side finite element strain result for the 70km/h speed

Fig. F-1 70km/h Finite element strain plots

F-2 50km/h Test Finite Element Analysis Plots

IV. Finite Element Analysis Strain Result for the 50km/h Test Between 2 and 4.5 Seconds

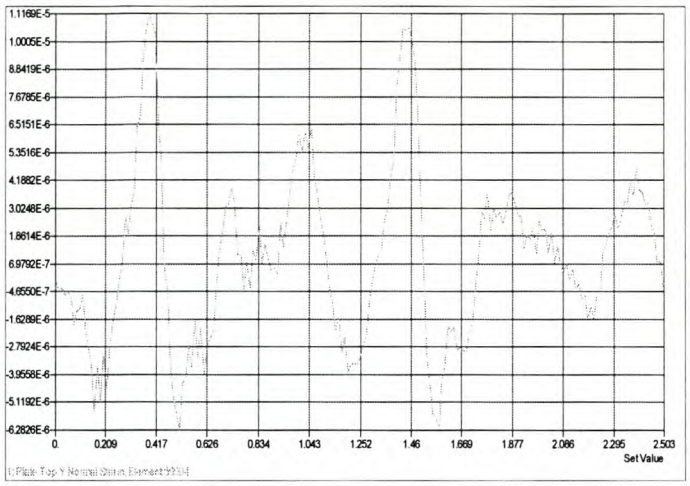

a. Right side

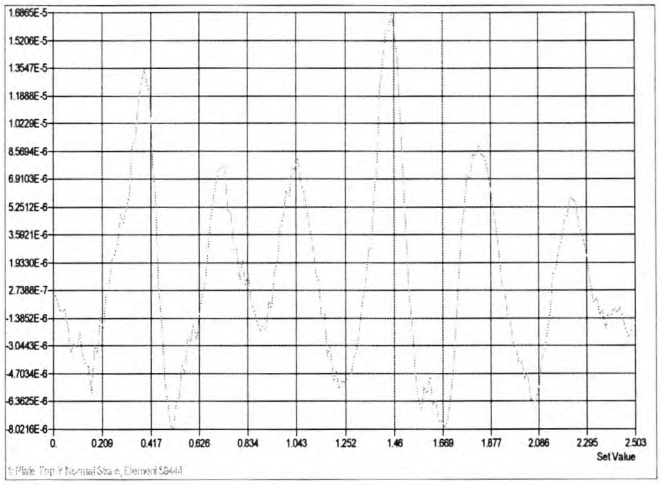

b. Left side

16. Full chassis finite element strain result for the 50km/h speed

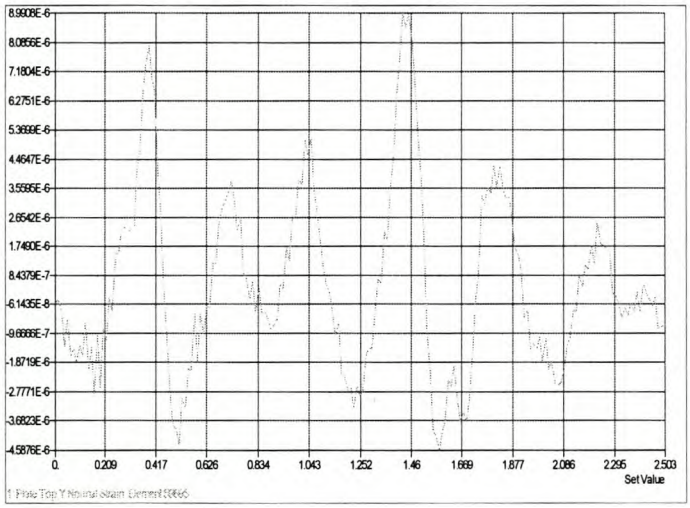

a. Right side

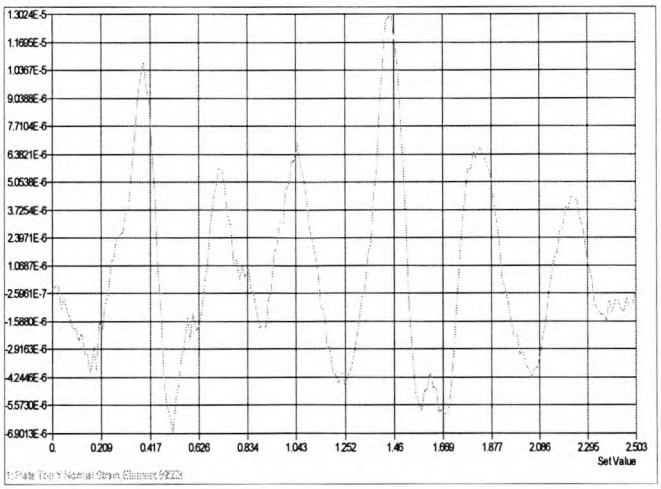

b. Left side

17. Tapered chassis finite element strain result for the 50km/h speed

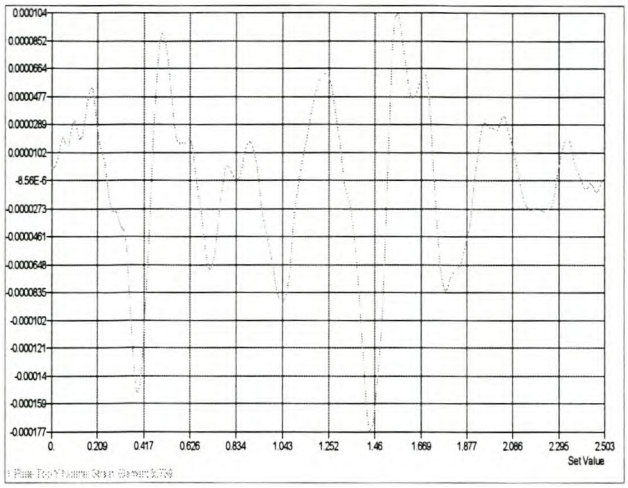

a. Right side

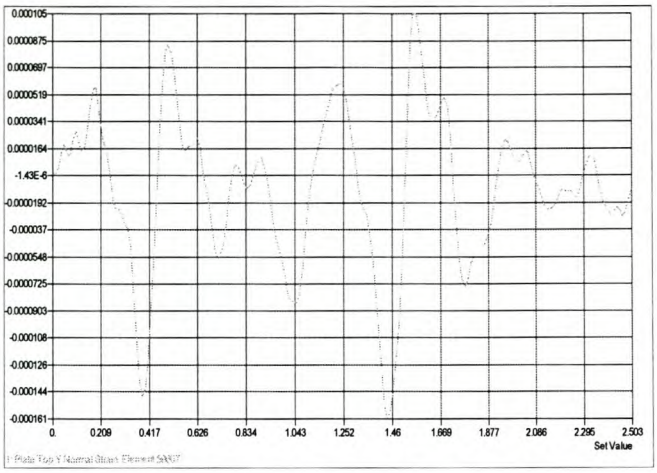

b. Left side

18. Chassis neck finite element strain result for the 50km/h speed

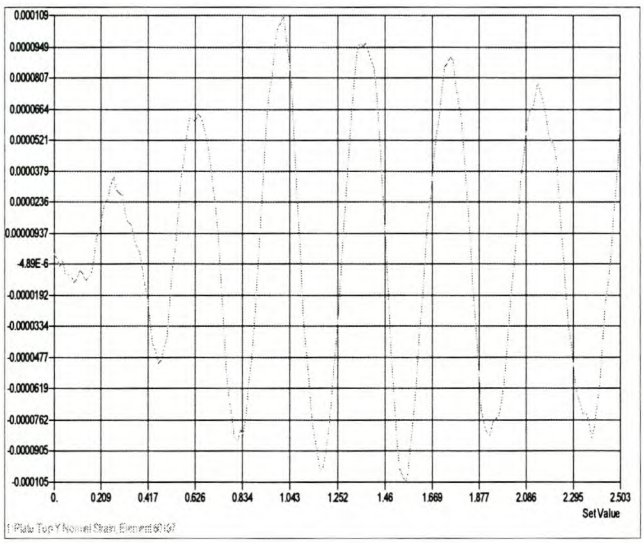

a. Right side

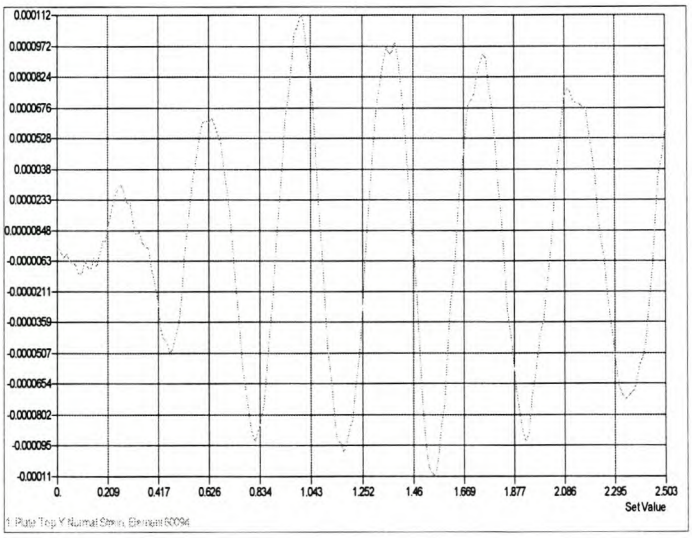

b. Left side

19. Rear plate finite element strain result for the 50km/h speed

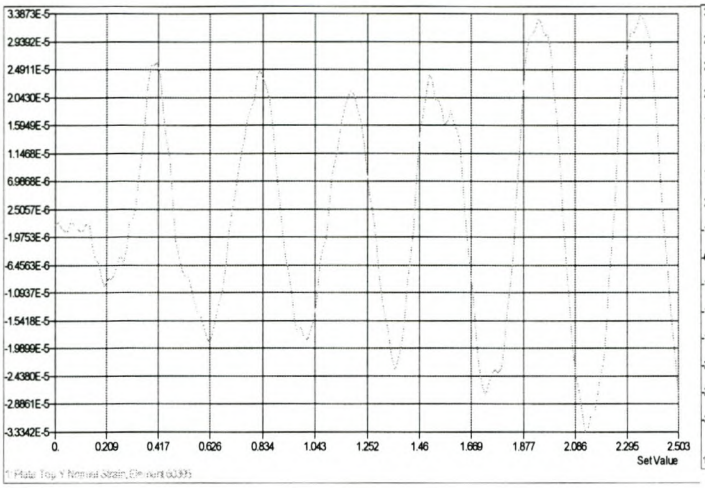

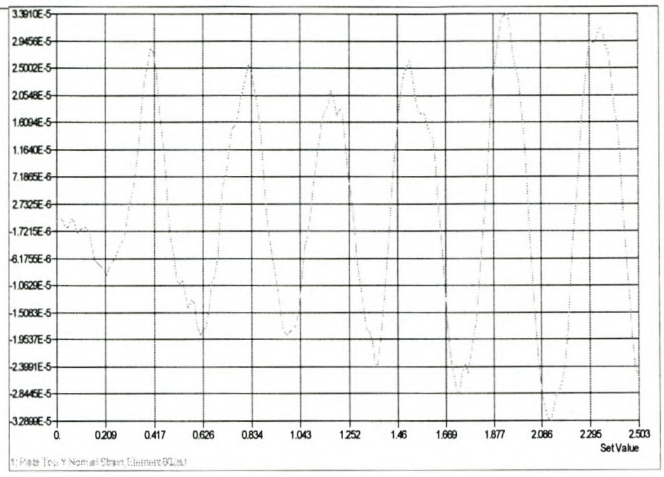

a. Right side

b. Left side

20. Front plate finite element strain result for the 50km/h speed

Fig. F-2 50km/h Finite element strain plots

F-3 40km/h Test Finite Element Analysis Plots

V. Finite Element Analysis Strain Result for the 40km/h Test
Between 0 and 5 Seconds

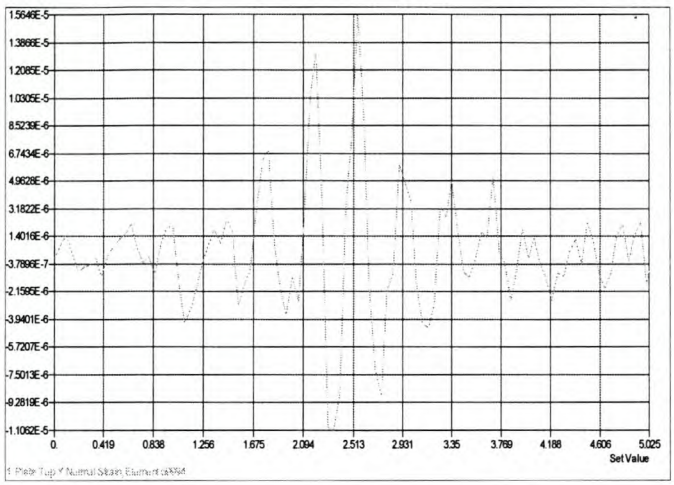

a. Right side

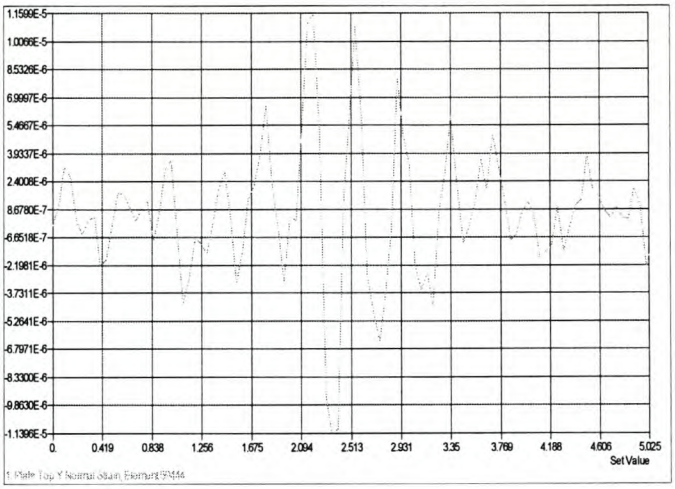

b. Left side

21. Full chassis finite element strain result for the 40km/h speed

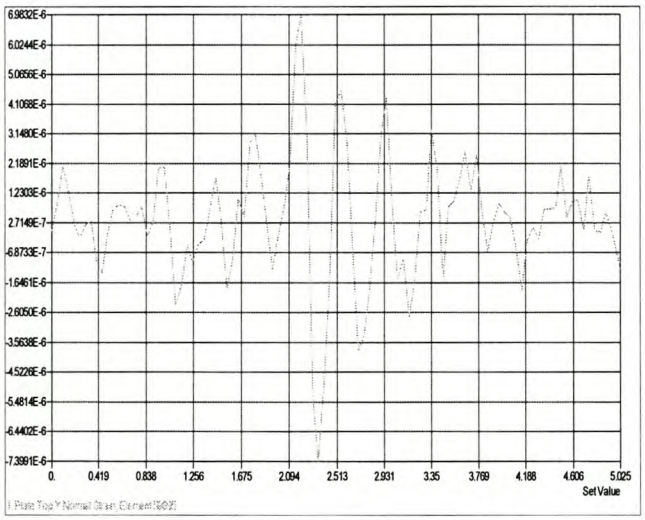

a. Right side

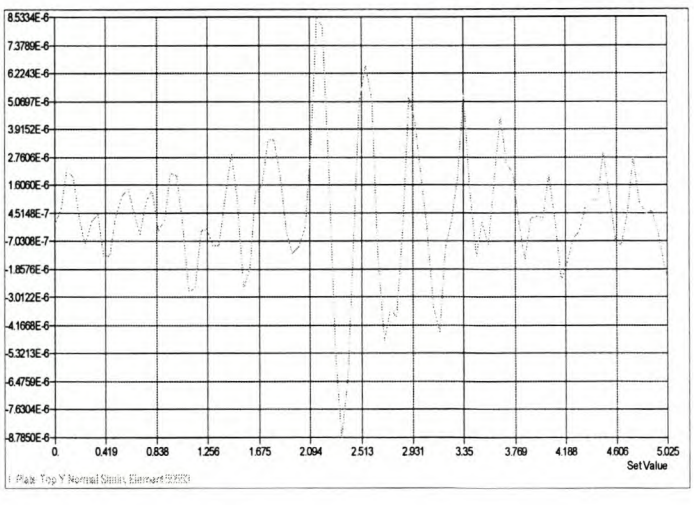

b. Left side

22. Tapered chassis finite element strain result for the 40km/h speed

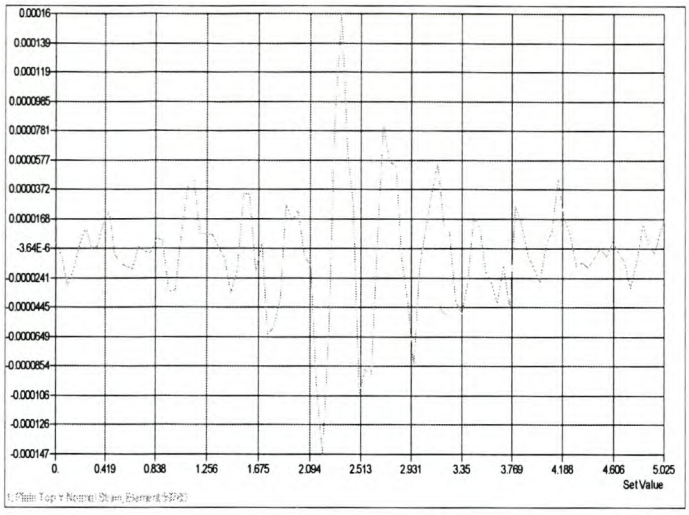

a. Right side

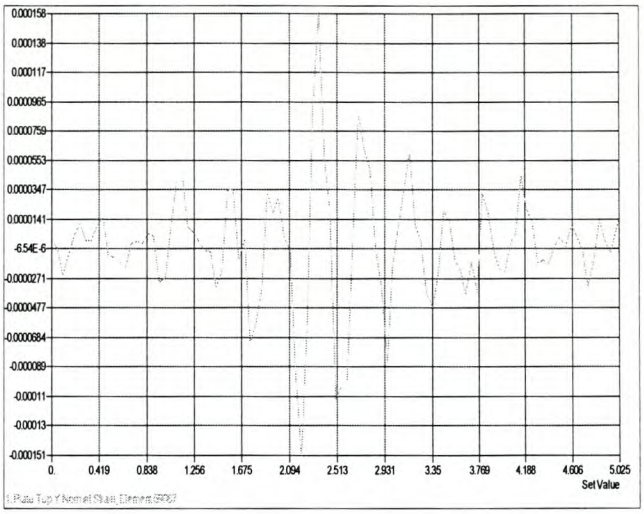

b. Left side

23. Chassis neck finite element strain result for the 40km/h speed

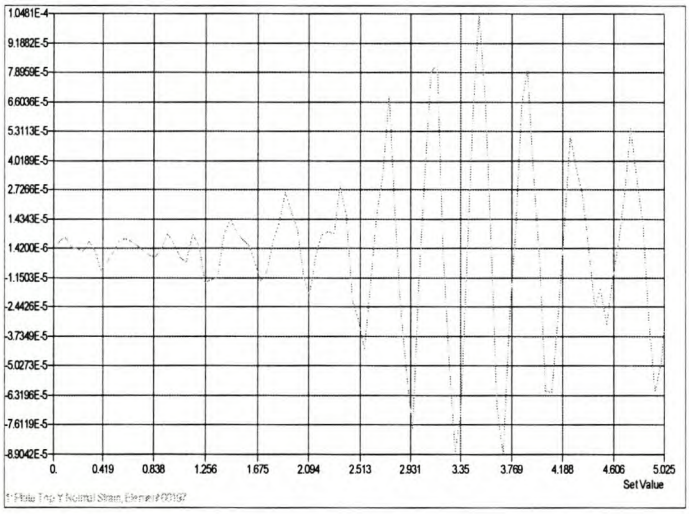

a. Right side

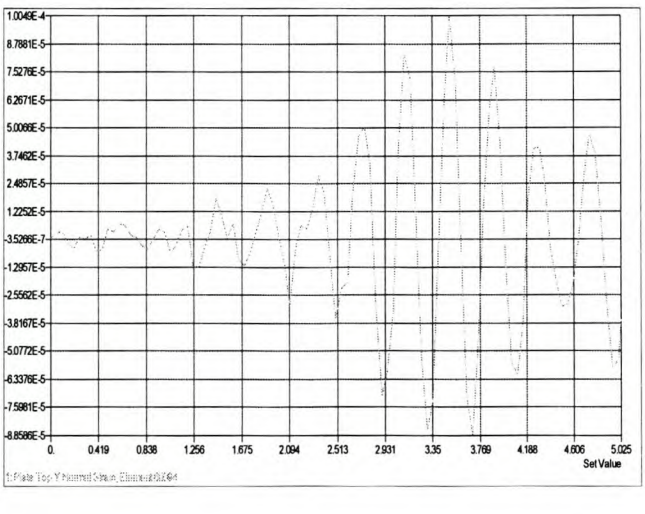

b. Left side

24. Rear plate finite element strain result for the 40km/h speed

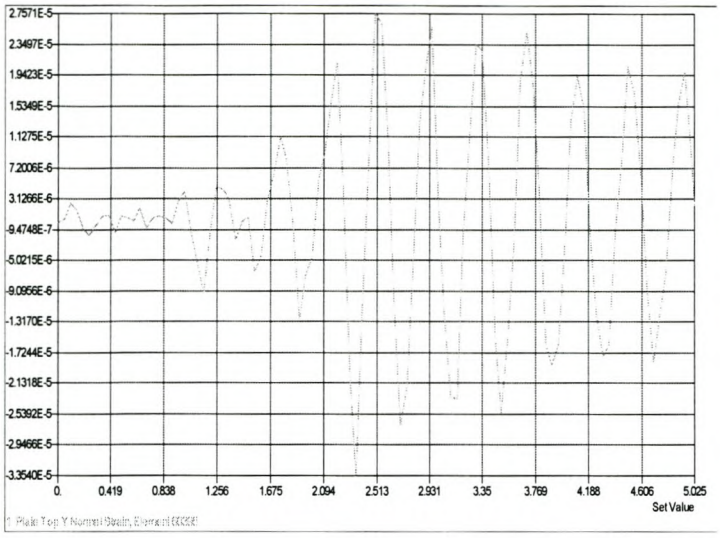

a. Right side

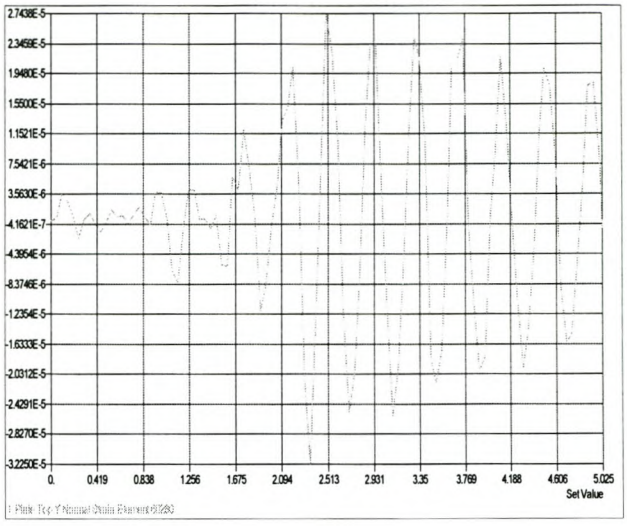

b. Left side

25. Front plate finite element strain result for the 70km/h speed

Fig. F-3 40km/h finite element strain plots

REFERENCES:

1. Dally, J.W. and Rilely, W.F. 1965. *Experimental Stress Analysis.* New York: McGraw-Hill.
2. Timeshenko, S.P. and Goodier, J.N. 1970. *Theory of Elasticity.* 3rd edition. Singapore: McGraw-Hill.
3. Newland, D.E. 1975. *Random Vibrations and Spectral Analysis.* London: Longman Group.
4. Ugural, A.C. and Fenster, S.K. 1977. *Advanced Strength and Applied Elasticity.* 2nd edition. New York: Elsevier Scientific Publishing Company.
5. SABS SV, 1051–1980, *Braking, Standard Specification VI.* Pretoria. South African Bureau of Standards.
6. Stevensen, W.J. 1983. *Static Structural Load Tests on a DE HAVILAND VAMPIRE WING (Master's thesis)*, Stellenbosch: University of Stellenbosch.
7. Ewins, D.J. 1984. *Modal Testing: theory and practice.* Letchworth, Hertfordshire: Research Studies Press.
8. Reddy, J.N. 1984. *An Introduction to the Finite Element Method.* New York: McGraw-Hill.
9. Yang, C.Y. 1986. *Random Vibration of Structures.* USA: Wiley.
10. Beermann, H.J. 1989. *Analysis of Commercial Vehicle Structures.* Koln. Verlag Tuv Rheinland GnΔb H.
11. Cook, R.D. Malkus, D.S. Plesha, M.E. 1989. *Concepts and Applications of Finite Element Analysis.* 3rd edition. New York: Wiley.
12. Window, A.L. 1992. *Strain Gauge Technology.* 2nd edition. England. Elsevier Science Publishers.
13. SABS 1398:1994. *Road Tank Vehicles for Petroleum-Based Flammable Liquids.* Pretoria: South African Bureau of Standards.
14. Inman, D.J. 1996. *Engineering Vibration.* Upper Saddle River, NJ: Prentice-Hall.
15. Hideaki, I., Yukinori, O., Hiroaki, H. and Junzo, T. *Dynamic Stress Analysis of a Fuel Tank Hanger.* ScienceDirect. JSAE Review. October 1996. http://www.sciencedirect/science. Accessed on Aug. 10, 2003.
16. Greenberg, M.D. 1998. *Advanced Engineering Mathematics.* 2ed edition. New Jersey: Prentice-Hall.

17. Sharma, V.M.J., Venkatanarayana, G., Diwakar, V., Arumugham, S. and Lakshmanan, T.S. *Failure of a high strength low alloy steel pressure chamber*. ScienceDirect. Engineering Failure Analysis. March 1998. http://www.sciencedirect/science. Accessed on Aug. 5, 2003.

18. Tamboli, J.A. and Joshi, S.G. *Optimum Design of a Passive Suspension System of a Vehicle Subjected to Actual Random Road Excitations*. ScienceDirect. Journal of Sound and Vibration. 14 January 1999. http://www.sciencedirect/science. Accessed on July 12, 2003.

19. Henshaw, J.M. Wood, V. and Hall, A.C. *Failure of automobile seat belts caused by polymer degradation.* ScienceDirect. Engineering Failure Analysis. February 1, 1999. http://www.sciencedirect/science. Accessed on July 2, 2003.

20. Masaaki, M., Jun, N., Jiro, N. and Yukihiro, O. *Method for measuring force transmitted from road surface to tyres and its applications.* ScienceDirect. *JSAE* Review. October 1999. http://www.sciencedirect/science. Accessed on July 2, 2003.

21. Figueiredo, M.V., Oliveira, F.M.F., Gonçalves, J.P.M., De Castro, P.M.S.T. and Fernandes, A.A. *Fracture analysis of forks of a heavy duty lift truck.* ScienceDirect. Engineering Failure Analysis. November 30,1999. http://www.sciencedirect/science. Accessed on July 2, 2003.

22. Du Toit, J.F. November 2000. *Design Evaluation and Redesign of a Refrigerated Semi-Trailer Structure Using the Finite Element Technique* (Master's thesis). Stellenbosch: University of Stellenbosch.

23. Silva, F.S. *Analysis of a vehicle crankshaft failure*. ScienceDirect. Engineering Failure Analysis. April 4 2003. http://www.sciencedirect/science. Accessed on Aug. 8, 2003.

24. . Terblanche, E. s.a. *Strain Gauge Notes*, Stellenbosch: University of Stellenbosch.

25. Hottinger Baldwin Messtechnik. s.a. *HBM Electrical Measurements for Mechanical Quantities*: *Operating Manuals*. Darmstadt, Hottinger Baldwin Messtechnik. GMBH